Application of Multiple Model Control to Space Structure Systems with Nonlinear Inertia Properties

by

Kazumi Masuda

Submitted to the Department of Aeronautics and Astronautics
in partial fulfillment of the requirements for the degree of

Master of Science in Aeronautics and Astronautics

at the

MASSACHUSETTS INSTITUTE OF TECHNOLOGY

June 1995

Author ....
Department of Aeronautics and Astronautics
May 22, 1995

Certified by ....
Dr. David W. Miller
Principal Research Scientist, Department of Aeronautics and Astronautics
Thesis Supervisor

Accepted by ....
Professor Harold Y. Wachman
Chairman, Department Graduate Committee

Application of Multiple Model Control to Space Structure Systems with Nonlinear Inertia Properties

by

Kazumi Masuda

Submitted to the Department of Aeronautics and Astronautics
on May 22, 1995, in partial fulfillment of the
requirements for the degree of
Master of Science in Aeronautics and Astronautics

Abstract

Future space systems will require high robustness of the control system as well as high performance because of their two major features: lightly damped structural dynamics; and nonlinear inertia properties induced by the large motion of articulating sensor heads and antennas. Effective robust control design techniques are needed to satisfy the performance requirements of future space systems in the presence of model uncertainties and nonlinear changes in their inertia properties.

In this thesis, the Multiple Model (MM) technique is applied to a plant system which has multiple off-nominal factors including nonlinear inertia properties. Three control design problems are presented to examine the effectiveness of the MM technique: sample designs for a simple plant system; single-input, single-output (SISO) designs for the Middeck Active Control Experiment (MACE); and multiple-input, multiple-output (MIMO) designs for the MACE. A plant model of the MACE test article has two off-nominal factors, *i.e.* frequency uncertainty in the Z-axis bending modes and nonlinear inertia changes due to different primary payload average angles. In each design problem, LQG compensators are first designed and used as initial compensators in the subsequent MM designs. Through the comparison between LQG and MM compensators, the effectiveness of the MM technique is examined.

In every design problem, the MM technique enhances robust stability and performance of an original LQG compensator with small loss in nominal performance. In particular, in the MIMO designs for the MACE, the MM technique substantially improves robust performance for nonlinear inertia properties of the MACE test article. This research reveals the effectiveness of the MM technique for multiple off-nominal factors including nonlinear changes of inertia properties.

Thesis Supervisor: Dr. David W. Miller
Title: Principal Research Scientist, Department of Aeronautics and Astronautics

Acknowledgments

I would like to thank my advisor, Dr. David Miller, for his guidance and support through the course of my research.

I would also like to thank the members of the MACE team for their suggestions and encouragement. Simon Grocott gave me technical advice on numerous occasions. Roger Glaese provided me with design data for a plant model. Mark Campbell gave me valuable suggestions. Without their support, this thesis would not have been completed within the limited time.

Special appreciation goes to Professor Wallace E. Vander Velde, who guided me from the start of my study at MIT and introduced me to this exciting MACE program.

Additional thanks goes to Professor Richard H. Battin, who greatly influenced me not only through his lectures of *Astrodynamics* at MIT but also through his outstanding contribution in the Apollo project.

Special appreciation goes to Dr. Paul E. Brown, Director of the Advanced Study Programs at MIT, who introduced me to MIT and gave me valuable encouragement and support.

Finally, I would like to thank Mitsubishi Heavy Industries, Ltd. for the opportunity to study at MIT.

Contents

List of Figures

List of Tables

Chapter 1

Introduction

Future space systems will require high robustness of the control system as well as high performance because of their two major features: lightly damped structural dynamics and nonlinear inertia properties induced by the large motion of articulating sensor heads and antennas. Effective robust control design techniques are needed to satisfy the performance requirements of future space systems in the presence of model uncertainties and nonlinear changes in their inertia properties.

In this introduction, the development of robust control design techniques is reviewed at first. The review covers the comparative study of robust control design techniques made by the research team in the Space Engineering Research Center (SERC) at the Massachusetts Institute of Technology (MIT). Secondly, the Mid-deck Active Control Experiment (MACE) program, conducted by the research team at SERC, is introduced as the most aggressive research to develop a control design methodology for future space systems. Finally, the motivation and objectives of this study are presented in the last section.

1.1 Robust Control Design techniques

In control designs, trade-offs between properties of a compensator are usually unavoidable. A trade-off between controller's nominal performance and sensitivity to uncertainty is a typical example of the trade-offs in control designs. Simple and effective means to evaluate controllers are needed to perform these trade-offs.

The Linear Quadratic Regulator (LQR) technique was developed to allow control designers to conduct designs in a practical way [1]. Through specifying weights on each of the state and control variables, the LQR technique provides the optimal state feedback gains which minimize an LQR cost functional, *i.e.* a weighted sum of quadratic state and control variables. An LQR controller is found by solving an algebraic Riccati equation and it guarantees stability margins, $\pm 60deg$ phase margin and $-6dB$ gain margin, in each channel [2]. However, an LQR controller is not practical, because all state variables cannot be measured in most design cases.

To allow sensor output feedback, Linear Quadratic Gaussian (LQG) control was introduced in the 1960s by combining an LQ regulator and a Kalman filter (KF), and had matured as a practical control design technique by the beginning of the 1970s [3]. Although an LQG solution is easily obtained by solving two decoupled algebraic Riccati equations, the LQG technique does not guarantee robust stability [4]. A laborious iterative design procedure like tuning the weights on the performance outputs and sensor noises has to be performed before obtaining an adequate compensator to satisfy stability requirements for off-nominal factors. This drawback of the LQG technique led control researchers and designers to demand robust control design techniques in the modern linear control theory.

In the following two decades, many robust control design techniques were developed mainly by modifying the LQG technique. The robust control techniques, such as LQG/Loop Transfer Recovery (LQR/LTR) [5, 6], Trajectory Sensitivity Optimization (TSO) [7], Sensitivity Weighted LQG (SWLQG) [8], Parameter Robust LQG [9], Maximum Entropy [10], and Multiple Model (MM) [11], are based on the LQG technique.

On the other hand, new approaches were also conducted to obtain a robust controller. The $\mathcal{H}_\infty$ technique has been studied most vigorously in the last fifteen years [12, 13]. The $\mathcal{H}_\infty$ technique is based on the $\mathcal{H}_\infty$ norm of the closed loop transfer function matrix from disturbance to performance, while the LQG technique is based on the quadratic ($\mathcal{H}_2$) norm. Although the $\mathcal{H}_\infty$ technique starts with a concept different from that of the LQG technique, it was proved that the $\mathcal{H}_\infty$ technique includes the LQG technique as a special case [13].

The most remarkable feature of the $\mathcal{H}_\infty$ formulation is that the compensator provides outstanding guaranteed robustness. However, this robustness is achieved with a large loss of nominal performance, and an $\mathcal{H}_\infty$ compensator is too conservative in many control design cases because its resulting robustness bounds far exceed the targeted bounds. Thus, the current issue in the $\mathcal{H}_\infty$ technique is the reduction of the conservatism of robustness [14].

The answer for the question of which robust control technique should be adopted totally depends on the plant system and the type of off-nominal factors. Grocott performed a comparative study of nine robust control techniques for flexible space structure systems, and demonstrated the effectiveness of SWLQG, ME, MM, and Popov Control Synthesis [15] and the extreme conservatism of $\mathcal{H}_\infty$ synthesis and μ-synthesis [16]. In particular, he emphasized the superiority of the MM technique for a plant system with real parametric uncertainties.

1.2 Middeck Active Control Experiment (MACE)

The recent development of robust control design techniques allows engineers to design high performance controllers. However, control designers can appreciate the benefit of robust control techniques, only if they have precise dynamic models of a plant system including the associated off-nominal models. In some control design cases, measurement data of an actual plant is available. Unfortunately, it is impossible for space system designers to have a precise dynamic model of a space system in a weightless state before the system is launched, because there is no way to perfectly simulate zero-gravity (0-g) conditions on the ground. This is a significant problem in designing a control system particularly for flexible space structure systems, because these systems have complex dynamic modes due to a large number of degrees of free-

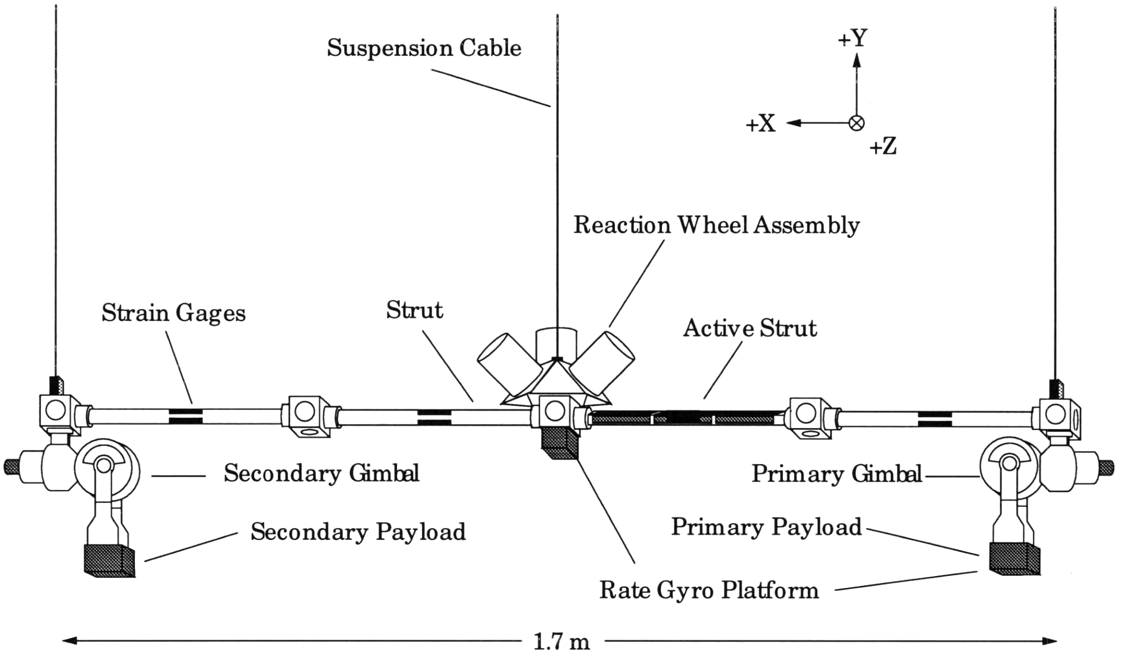

Figure 1-1: Middeck Active Control Experiment (MACE) test article (ground experiment configuration in 1-g)

dom in their dynamics.

The Middeck Active Control Experiment (MACE) program was conducted by the research team in the Space Engineering Research Center (SERC) at the Massachusetts Institute of Technology (MIT) in order to establish a control design methodology for space systems which have interaction between their attitude and pointing control and their structural dynamics [17]. The main technical challenges in the MACE program are to develop a precise analytical 0-g model with a combination of Finite Element Method [18] and 1-g measurement data of a plant system, and to design high performance compensators for 0-g implementation using several robust control design techniques.

The MACE test article, shown in Figure 1-1, was developed as a typical flexible space structure system. It consists of four flexible struts, a three-axis reaction wheel assembly, and two payloads: the primary payload and secondary payload. The reaction wheel assembly is equipped at the center of the structure and controls the bus attitude in the three axis. Each payload is controlled by a two-axis (X and Z axis) gimbal at each end of the connected struts. The actuator system, consisting of the reaction wheel assembly and two gimbals, allows the MACE test article to control each section separately and prevents it from being destabilized by the interaction between its control and structural dynamics. The sensor system includes three rate gyros collocated with the reaction wheel assembly, two (X and Z axis) rate gyros in the primary payload, and two (X and Z axis) encoders in each gimbal. In total, the MACE test article has seven actuator inputs and nine sensor outputs (three inertial angels of the bus body, two inertial angles of the primary payload, and two relative angles at each gimbal system). The secondary payload can simulate an uncollocated disturbance source. Large motion of the payloads causes nonlinear changes of the MACE test article's inertia properties.

The MACE program was in its climax when the 0-g dynamic model measurements and control experiments were operated on the United States Space Shuttle *Endeavor* during the STS-67 mission in May 1995. The flight experiments validated the control design methodology developed by the research team of SERC. Detailed results will be reported by the research team in the near future.

1.3 Motivation, Objectives, and Outline

The control objective in the MACE program was to maintain the inertial pointing of the primary payload while the second payload was undergoing either broad or narrowband excitation. The frequency uncertainty, based on the comparison between a 1-g analytical model and a 1-g measurement model, was used as the off-nominal factor in the MACE control design.

Most space systems have large antennas and sensor heads which are required to have tracking modes as well as pointing modes. Large-angle tracking causes the inertia properties to change in a nonlinear way. These nonlinear inertia property changes can destabilize the closed loop control system when it is designed without their consideration. Therefore, future space systems require a reliable and high performance control system, which can deal with nonlinear inertia properties as well as model uncertainties.

There are two major design approaches to satisfy this requirement: nonlinear control and linear, robust control. Nonlinear control has been vigorously studied by many researchers lately, because all the plant systems in practical control designs have nonlinear properties. Feedback Linearization is a typical nonlinear control technique [19]. Feedback Linearization technique provides excellent performance for a nonlinear plant system, when a precise nonlinear mathematical model of the nonlinear plant system is obtained. However, this technique cannot be applied to all types of nonlinear systems, and it is difficult to develop a precise nonlinear mathematical model in practical designs. Due to poor robustness of a Feedback Linearization controller, an inaccurate nonlinear model causes large performance degradation or destabilization [20]. Furthermore, full states have to be measured in a Feedback Linearization controller. In many plants including the MACE test article, it is impossible to measure full states. Therefore, many researchers are currently making great efforts to develop nonlinear observers. However, they are still immature because they all have drawbacks, such as necessity of an exact nonlinear mathematical model and heavy computational loads [21].

Adaptive Control is another typical nonlinear control technique. The basic concept of Adaptive Control is to estimate plant uncertainties based on on-line measurement data and to adjust gains in the controller. Since there is unknown variation of a plant in many practical designs, Adaptive Control has been expected to be useful in practical application. However, an instability problem of existing Adaptive Control algorithms was pointed out by Rohrs *et al* [22]. Although research on the Robust Adaptive Control Problem has been vigorously pursued since then, no effective modification has been proposed yet [23].

Although linear control techniques are usually applied at each operating point, Gain Scheduled Control is categorized as one of the nonlinear control techniques. In spite of a lack of strong theoretical background, this technique is applied to many practical problems. The main drawback of this technique is no guarantee of the stability and performance of the system at intermediate points [24]. To maintain stability robustness, the system needs to vary sufficiently slowly [23]. Since space systems including the MACE test article are not usually required to make quick motion, Gain Scheduled Control is applicable to them. However, an onboard processor needs to have a sufficiently large capacity because several sets of gains need to be installed in it.

As mentioned above, nonlinear control techniques are still immature and require high computational performance and large capacity of an onboard processor. On the other hand, linear, robust control techniques are reliable because they are based on mature linear control theories. Some robust control techniques, such as Multiple Model, $\mathcal{H}_\infty$ synthesis, μ-synthesis, and Popov Control synthesis, guarantee robust stability for designated off-nominal conditions. Furthermore, requirements for a processor are not excessive. Therefore, it is a reasonable approach to apply linear, robust control techniques to a nonlinear plant at first and to examine the performance limit of linear, robust controllers. The main issue in implementing a robust control design is a trade-off between controller's nominal performance and robustness. The question of which robust control design is the most effective depends on properties of a plant system. Therefore, it is very important to find the most effective robust technique to a plant system that provides a large robustness gain at a sacrifice of a small nominal performance loss.

The objective of this research is to examine the effectiveness of a linear, robust control technique at designing high performance compensators which stabilize a space structure system with nonlinear inertia properties. The Multiple Model (MM) technique is examined as one of the most effective robust control design techniques for a space structure system, while the MACE test article is adopted as a typical space structure system.

This thesis consists of three main chapters. In Chapter 2, the LQG and MM techniques are introduced and applied to a sample structural system, the 4-mode free-free flexible beam, to understand the destabilization mechanisms associated with a lightly damped structural plant. The development of the analytical model of the 4-mode free-free flexible beam using the Finite Element Method [18] is also presented in this chapter. Chapter 3 presents SISO designs for the MACE test article with four Z-axis bending modes to examine the influence of nonlinear inertia properties caused by different primary payload average angles and the effectiveness of the MM technique. Two off-nominal factors are considered: $\pm 10\%$ frequency uncertainty in the second Z-axis bending mode and $\pm 45deg$ primary gimbal average angles. The frequency uncertainty is caused by model errors and is limited in the second Z-axis bending mode in this SISO design case to mainly examine the effect of the other off-nominal factor, *i.e.* the primary gimbal average angle. Large changes of the primary gimbal angle result in nonlinear changes of the MACE test article's inertia properties.

Finally, in Chapter 4, MIMO designs for the MACE test article are performed as a more realistic design case. The secondary payload acts as an uncollocated disturbance source. Two off-nominal factors are also considered in MIMO designs: $\pm 2.5\%$ frequency uncertainty in all Z-axis bending modes and $\pm 45deg$ primary gimbal average angles.

Chapter 2

Control Design Techniques and Sample Designs

A compensator for future space systems must be robust to their two major off-nominal factors, *i.e.* uncertainty in structural dynamics and geometric nonlinearity. The Linear Quadratic Gaussian (LQG) is powerful in control designs for future space systems because of its practicality; a high authority compensator is easily obtained by solving two decoupled algebraic Riccati equations. However, this technique cannot guarantee robust stability. Therefore, robust control techniques need to be applied to future space systems. The Multiple Model (MM) technique can be used in control designs for future space systems as the most effective robust control technique.

The objectives of this chapter are to introduce the LQG and MM technique and to examine basic properties of an LQG and MM compensator for space structural systems through sample designs for a free-free beam.

2.1 Linear Quadratic Gaussian (LQG)

To allow sensor output feedback, Linear Quadratic Gaussian (LQG) control was introduced as a practical control design technique by combining an LQ regulator and a Kalman filter (KF). Although an LQG solution is easily obtained by solving two decoupled algebraic Riccati equations, the LQG technique does not guarantee robust stability. This drawback of the LQG technique led control researchers and designers to demand robust control design techniques. Many robust control techniques including Multiple Model (MM) were developed based on the LQG technique. Therefore, the LQG technique is applied to many engineering problems as a basic linear control technique. In this study, LQG compensators are used as an initial compensator in a MM design and compared with resulting MM compensators. This section presents the formulation of the LQG technique and the design strategy in applying the LQG technique to the design problems presented in this study.

2.1.1 Formulation

Control design always starts at modeling the plant. The Linear Quadratic Gaussian (LQG) method is no exception [3]. A linear time invariant equation has to be formulated. The following general form is often adapted in order to generalize $\mathcal{H}_2$ and $\mathcal{H}_\infty$ design techniques [12, 13].

$$\begin{aligned} \dot{x} &= Ax + B_w w + B_u u \\ z &= C_z x + D_{zw} w + D_{zu} u \\ y &= C_y x + D_{yw} w + D_{yu} u \end{aligned} \tag{2.1}$$

where x, z, and y are a state variable vector, a performance vector, and an output vector, respectively. w and u are a disturbance vector and a control variable vector, respectively.

The open loop transfer functions from the inputs, w and u, to the outputs, z and y, are given by

$$\begin{aligned} G_{zw}(s) &= C_z(sI - A)^{-1}B_w + D_{zw}, \\ G_{zu}(s) &= C_z(sI - A)^{-1}B_u + D_{zu}, \end{aligned} \tag{2.2}$$

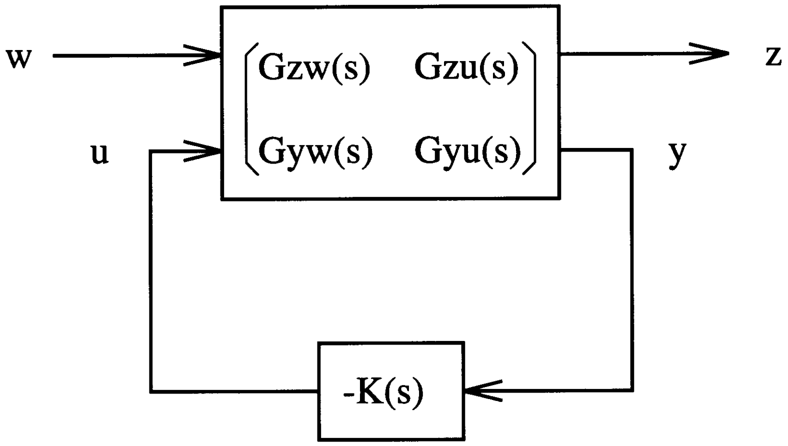

Figure 2-1: General control system

$$\begin{aligned} G_{yw}(s) &= C_y(sI-A)^{-1}B_w + D_{yw}, \\ G_{yu}(s) &= C_y(sI-A)^{-1}B_u + D_{yu}. \end{aligned}$$

Figure 2-1 shows the closed loop system with the compensator, $K(s)$. The closed loop performance transfer function from w to z is given by

$$G_{cl}(s) = G_{zw}(s) - G_{zu}(s)K(s)\left[I + G_{yu}(s)K(s)\right]^{-1} G_{yw}(s). \tag{2.3}$$

The compensator, $K(s)$, is represented as

$$\begin{aligned} \dot{x}_c &= A_c x_c + B_c y, \\ u &= -C_c x_c, \end{aligned} \tag{2.4}$$

where x_c is a state variable vector estimated by the filter.

Then, by using the representation of the closed loop system, the plant system, which is equivalent to Equation (2.1), is written in the augmented state space representation,

$$\begin{aligned} \dot{\tilde{x}} &= \tilde{A}\tilde{x} + \tilde{B}w \\ z &= \tilde{C}\tilde{x} + \tilde{D}w \end{aligned} \tag{2.5}$$

where

$$\begin{aligned}
\tilde{x} &= \begin{bmatrix} x \\ x_c \end{bmatrix}, \\
\tilde{A} &= \begin{bmatrix} A & -B_u C_c \\ B_c C_y & A_c - B_c D_{yu} C_c \end{bmatrix}, \\
\tilde{B} &= \begin{bmatrix} B_w \\ B_c D_{yw} \end{bmatrix}, \\
\tilde{C} &= \begin{bmatrix} C_z & -D_{zu} C_c \end{bmatrix}, \\
\tilde{D} &= D_{zw}.
\end{aligned}$$

By using the representation above, the closed loop transfer function, which is equivalent to Equation (2.3), is given by

$$G_{cl}(s) = \tilde{C}(sI - \tilde{A})^{-1}\tilde{B} + \tilde{D}. \tag{2.6}$$

The smaller the gain of the closed loop transfer function, the better the closed loop system rejects disturbances. Therefore, the objective of control design is to find a compensator which minimizes the closed loop transfer function, $G_{cl}(j\omega)$.

There are many ways to evaluate the magnitude of $G_{cl}(j\omega)$. The $\mathcal{H}_2$ norm is adopted in the LQG technique, while the $\mathcal{H}_\infty$ norm is used in the $\mathcal{H}_\infty$ technique [25].

The $\mathcal{H}_2$ norm is defined as

$$\begin{aligned}
||G_{cl}(s)||^2_{\mathcal{H}_2} &= \frac{1}{2\pi} trace \int_{-\infty}^{+\infty} G_{cl}(j\omega) G^*_{cl}(j\omega)\, d\omega \qquad (2.7) \\
&= trace \int_0^{\infty} G_{cl}(t) G^T_{cl}(t)\, dt.
\end{aligned}$$

In the equation above, the Parseval theory is applied to transfer the integration with respect to frequency to the integration with respect to time [26].

There is no general analytic solution of the integration above, because the solution depends on the input to the closed loop system. In the LQG technique, an impulse input is adopted to have a specific solution. Since the time domain transfer function of the closed loop system, which is given by Equation (2.6), for an impulse input is

$$G_{cl}(t) = \tilde{C}\exp(\tilde{A}t)\tilde{B}, \tag{2.8}$$

then the $\mathcal{H}_2$ norm of the transfer function is given by [27]

$$\begin{aligned} \|G_{cl}(s)\|^2_{\mathcal{H}_2} &= trace \int_0^\infty \tilde{C}\exp(\tilde{A}t)\tilde{B}\tilde{B}^T\exp(\tilde{A}^T t)\tilde{C}^T\,dt \\ &= trace\left[\tilde{C}\tilde{Q}\tilde{C}^T\right], \end{aligned} \tag{2.9}$$

where $\tilde{Q}$ is the solution of the Lyapunov equation,

$$\tilde{A}\tilde{Q} + \tilde{Q}\tilde{A}^T + \tilde{B}\tilde{B}^T = 0. \tag{2.10}$$

In the LQG technique, the $\mathcal{H}_2$ norm defined above is adopted as the LQG cost functional, J, which includes both state and control components.

On the other hand, applying stochastic inputs to the closed loop system also gives the same cost functional for the LQG problem.

$$\begin{aligned} J &= \|G_{cl}\|^2_{\mathcal{H}_2} && (2.11) \\ &= \lim_{T\to\infty}\frac{1}{T}\mathsf{E}\left\{\int_0^T z^T z\,dt\right\} \\ &= \lim_{T\to\infty}\frac{1}{T}\mathsf{E}\left\{\int_0^T \left[x^T R_{xx}x + 2x^T R_{xu}u + u^T R_{uu}u\right]\,dt\right\}, && (2.12) \end{aligned}$$

where $D_{zw} = 0$ to guarantee finite $\mathcal{H}_2$ norm. E is the expectation operator. The weights for the state variables and the control variables are defined as

$$R = \begin{bmatrix} R_{xx} & R_{xu} \\ R^T_{xu} & R_{uu} \end{bmatrix} = \begin{bmatrix} C^T_z \\ D^T_{zu} \end{bmatrix}\begin{bmatrix} C_z & D_{zu} \end{bmatrix} \tag{2.13}$$

Note that R and R_{uu} need to be a semi-positive definite matrix ($R \geq 0$) and a positive definite matrix ($R_{uu} > 0$), respectively.

Now the optimum gains, F and H, which minimize the cost functional in the LQG problem, Equation (2.9) or Equation (2.12), are given by

$$\begin{aligned} F &= R_{uu}^{-1}\left[R_{xu}^{T} + B_u^{T}P\right] && (2.14)\\ H &= \left[QC_y^{T} + V_{xy}\right]V_{yy}^{-1}, && (2.15) \end{aligned}$$

where P and Q are the solutions of the following two decoupled algebraic Riccati equations,

$$\begin{aligned} 0 &= PA + A^{T}P + R_{xx} - \left[PB_u + R_{xu}\right]R_{uu}^{-1}\left[R_{xu}^{T} + B_u^{T}P\right] && (2.16)\\ 0 &= AQ + QA^{T} + V_{xx} - \left[QC_y^{T} + V_{xy}\right]V_{yy}^{-1}\left[V_{xy}^{T} + C_yQ\right], && (2.17) \end{aligned}$$

and the weights for the estimated state variables and the sensor noises are defined as

$$V = \begin{bmatrix} V_{xx} & V_{xy} \\ V_{xy}^{T} & V_{yy} \end{bmatrix} = \begin{bmatrix} B_w \\ D_{yw} \end{bmatrix}\begin{bmatrix} B_w^{T} & D_{yw}^{T} \end{bmatrix}. \qquad (2.18)$$

V and V_{yy} need to be a semi-positive definite matrix ($V \geq 0$) and a positive definite matrix ($V_{yy} > 0$), respectively.

The LQG compensator is composed by applying the LQG optimum gain set, Equation (2.14) and Equation (2.15), to the compensator, $K(s)$ represented by Equation (2.4). Thus, the system matrices of the LQG compensator are given by

$$\begin{aligned} A_c &= A - B_uF - HC_y + B_uD_{yu}C_y && (2.19)\\ B_c &= H \\ C_c &= F. \end{aligned}$$

The most remarkable feature of the LQG compensator is the separation principle [28]. The LQG compensator can be separated into the LQR (Linear Quadratic Regulator) and the KF (Kalman Filter). However, the LQG compensator does not have robustness guarantees [4], while the LQR and KF individually have $\pm 60 deg$

phase margin in each channel, independently and simultaneously, and $\left[\frac{1}{2},\ +\infty\right]$ gain margin [2].

By using the estimation error vector, $e = x - x_c$, and the system matrices of the LQG compensator given by Equation (2.19), the augmented state representation of the closed loop system, Equation (2.5), can be reformulated as

$$\begin{aligned} \frac{d}{dt}\begin{bmatrix} x \\ e \end{bmatrix} &= \begin{bmatrix} A - B_uF & B_uF \\ 0 & A - HC_y \end{bmatrix}\begin{bmatrix} x \\ e \end{bmatrix} + \begin{bmatrix} B_w \\ B_w - HD_{yw} \end{bmatrix} w \qquad (2.20) \\ z &= \begin{bmatrix} C_z - D_{zu}F & D_{zu}F \end{bmatrix}\begin{bmatrix} x \\ e \end{bmatrix}. \end{aligned}$$

Note that $\tilde{D} = D_{zw} = 0$ for the LQG problem.

Therefore, the closed loop poles are given by

$$det\,[\lambda I - (A - B_uF)] = 0 : \text{LQR poles} \qquad (2.21)$$

$$det\,[\lambda I - (A - HC_y)] = 0 : \text{KF poles.} \qquad (2.22)$$

Using the equations above, the LQR poles and KF poles can be specified respectively.

2.1.2 Design Strategy

The most outstanding feature of the LQG design technique is the systematic design procedure made possible through the tuning of the state, control, and filter weights. Tuning the weights determines the properties of the compensator. In the general form of the plant system, C_z, D_{zu}, and D_{yw} matrices correspond to the state weights, the control weights, and the filter weights, respectively. The weights are determined from these matrices by Equation (2.13) and Equation (2.18).

In most of control design cases, however, the number of the weights easily becomes large. In particular, the number of state variables in the flexible space structure problem, which is the main topic of this study, is quite large. This leads control designers to laborious trial-and-error design procedures before getting adequate compensators which satisfy the design requirements. Therefore, effective ways of tuning the weights are required.

In this study, the following procedure is adopted for tuning the weights in the LQG problem.

1. Since only relative ratios among the weights are meaningful, the B_w, C_z, D_{zu}, and D_{yw} matrices are set in the first step such that

$$\begin{aligned} B_w &= \begin{bmatrix} B_{w0\,(n_x \times n_p)} & 0_{(n_x \times n_s)} \end{bmatrix} && (2.23) \\ C_z &= \begin{bmatrix} diag(\sigma_i)\, C_{z0\,(n_{zx} \times n_x)} \\ 0_{(n_u \times n_x)} \end{bmatrix} && (2.24) \\ D_{zu} &= \begin{bmatrix} 0_{(n_{zx} \times n_u)} \\ diag(\rho_j)\, D_{zu0\,(n_u \times n_u)} \end{bmatrix} \times \rho && (2.25) \\ D_{yw} &= \begin{bmatrix} 0_{(n_y \times n_p)} & [diag(\theta_k)\, D_{yw0}]_{(n_y \times n_s)} \end{bmatrix} \times \theta, && (2.26) \end{aligned}$$

where ρ and θ are scalar weights on the control variables and the sensor noises, respectively. σ_i, ρ_j, and θ_k are individual scalar weights on each component of the state and control variables, and the sensor noises, respectively. All the individual scalar weights are set to one, at first. The $diag(\cdot)$ indicates a square matrix which has the specified individual scalar weights as diagonal entries. n_x, n_u, and n_y are the order of the state variable vector, x, the control variable vector, u, and the output variable vector, y, respectively. n_{zx} is the number of the state variables which are chosen as the components of the performance vector. n_p and n_s are the number of the process and sensor noises, respectively.

Since the C_z and D_{zu} matrices mentioned above have a zero submatrix, they give a set of independent weights on the state variables and control variables, and zero weights on the cross product of the state and control variables. The weights on the state-control product play an important role in the robust control design. An adequate set of the weights on the state, control, and state-control product provides good robustness. The sensitivity weighted LQG (SWLQG) is a robust control technique which positively uses the state-control product [8]. In this study, however, the state-control product is set to zero for simplicity.

The B_w and D_{yw} also have a zero submatrix to make the process and sensor noises uncorrelated; $B_w D_{yw}^T = 0$.

2. Set a control scalar weight, ρ, and then find a disturbance scalar weight, θ, so that the following condition is satisfied.
   - Balanced Weight Condition :

$$\frac{J_1}{J_4} = \frac{J_2}{J_3}, \tag{2.27}$$

$$\text{where } \begin{aligned} J_1 &= trace\,[PV_{xx}] \\ J_2 &= trace\,[R_{xx}Q] \\ J_3 &= trace\left[P(QC_y^T + V_{xy})V_{yy}^{-1}(V_{xy}^T + C_yQ)\right] \\ J_4 &= trace\left[(PB_u + R_{xu})R_{uu}^{-1}(R_{xu}^T + B_u^TP)Q\right] \end{aligned}$$

Note that J_1 and J_3 contribute to the LQG cost, Equation (2.9) or Equation (2.12), by the regulator part of the LQG compensator, and that J_2 and J_4 contribute to the LQG cost by the filter part of the LQG compensator. The LQG cost functional can be written by using J_1, J_2, J_3, and J_4.

$$\begin{aligned} J &= J_1 + J_4 \\ &= J_2 + J_3 \end{aligned}$$

Therefore, satisfying the Balanced Weight Condition gives an LQG compensator which has an evenly-balanced regulator and filter cost contribution. Smaller control scalar weights give higher authority compensators. Control authority of the compensator corresponds to the bandwidth of the compensator; high authority compensators have high crossover frequency.

3. Change individual scalar weights, σ_i, ρ_j, and θ_k, in C_z, D_{zu}, and D_{yw} in order to modulate cost contribution by the individual variables or sensor noises. Then, apply the Balanced Weight Condition to find a new disturbance scalar weight, θ. A heavier individual scalar weight on a particular variable or sensor noise makes its LQG cost contribution smaller. The analysis tools, such as the frequency response plot mentioned in Section 2.3.2, are helpful to obtain information on individual variables and sensor noises. Repeat this step until a desirable LQG compensator is obtained.

The tuning of the weights is the most laborious process in a LQG design. The procedure described above is one of the measures to reduce the laboriousness.

2.2 Multiple Model (MM) Method

The Multiple Model (MM) method can be based on the LQR or the LQG [11, 29] problems. In this study, the MM method based on the LQG is adopted, because it is more practical than that based on the LQR.

The most remarkable feature of the MM method is that it provides guaranteed robustness for designers, through direct specification of off-nominal design points, with relatively small loss in nominal performance [16]. Compensators designed with the MM method guarantee stability at a nominal design point and every specified off-nominal design point but do not guarantee stability outside of the design points.

The principle of the MM method is to find a compensator which stabilizes every design point plant system and minimizes a weighted sum of the LQG costs of each design point. While the principle of the MM method is easy, there is no analytical equation like the algebraic Riccati equations in LQG, Equations (2.16) and (2.17), which can be solved analytically. Therefore, numerical nonlinear multivariable optimization methods, such as the Newton method or the Quasi-Newton method [30, 31], need to be introduced to find the solution. This results in a large amount of calculation load and does not guarantee convergence to an optimal solution.

2.2.1 Formulation

Because the Multiple Model (MM) design technique is based on the LQG design technique, the formulation of the MM method starts at the formulation of the LQG method developed in Section 2.1.1.

Since the LQG is a design technique based on a linear, time-invariant plant system, there are two kinds of off-nominal sources: uncertainty and unmodeled dynamics. Nonlinearity is one of the unmodeled dynamics which is removed in the process of linearization. The MM method provides linear time invariant compensators which stabilize off-nominal plant systems by increasing robustness of the compensators.

At first, some off-nominal design points based on off-nominal factors of the plant system have to be selected. The linear time invariant state equations can be set at each design point including the nominal design point as follows:

$$\begin{aligned} \dot{x} &= A_i x + B_{w_i} w + B_{u_i} u \\ z &= C_{z_i} x \qquad\qquad + D_{zu_i} u \\ y &= C_{y_i} x + D_{yw_i} w + D_{yu_i} u, \end{aligned} \tag{2.28}$$

where the subscript "i" refers to the design points. Note that $D_{zw_i} = 0$ for the LQG problem.

With the compensator, $K(s)$,

$$\begin{aligned} \dot{x}_c &= A_c x_c + B_c y \\ u &= -C_c x_c, \end{aligned} \tag{2.29}$$

the augmented state equations at each design point can be written as

$$\begin{aligned} \dot{\tilde{x}} &= \tilde{A}_i \tilde{x} + \tilde{B}_i w \\ z &= \tilde{C}_i \tilde{x}, \end{aligned} \tag{2.30}$$

where

$$\begin{aligned} \tilde{x} &= \begin{bmatrix} x \\ x_c \end{bmatrix} \\ \tilde{A}_i &= \begin{bmatrix} A_i & -B_{u_i} C_c \\ B_c C_{y_i} & A_c - B_c D_{yu_i} C_c \end{bmatrix} \\ \tilde{B}_i &= \begin{bmatrix} B_{w_i} \\ B_c D_{yw_i} \end{bmatrix} \\ \tilde{C}_i &= \begin{bmatrix} C_{z_i} & -D_{zu_i} C_c \end{bmatrix}. \end{aligned}$$

The LQG cost can be determined by the system matrices of the augmented state equations. Thus, the weighted sum of the LQG costs at the design points is given by

$$J_a = \sum_{i=1}^{n_{DP}} \beta_i \, trace \left[\tilde{C}_i \tilde{Q}_i \tilde{C}_i^T \right], \tag{2.31}$$

where β_i is a weight on the LQG cost at each design point and $\sum_{i=1}^{n_{DP}} \beta_i = 1$. And $\tilde{Q}_i$ is the solution of the Lyapunov equation at each design point,

$$\tilde{A}_i \tilde{Q}_i + \tilde{Q}_i \tilde{A}_i^T + \tilde{B}_i \tilde{B}_i^T = 0. \tag{2.32}$$

Now, the MM problem is to find the matrix set, A_c, B_c, and C_c, which minimizes the weighted sum of the LQG costs, J_a, under the condition of the Lyapunov equations, Equation (2.32).

By using the Lagrange multipliers, $\tilde{P}_i$, the weighted sum of the LQG costs can be written as

$$J_a = \sum_{i=1}^{n_{DP}} \beta_i \, trace \left[\tilde{C}_i \tilde{Q}_i \tilde{C}_i^T + \tilde{P}_i \left(\tilde{A}_i \tilde{Q}_i + \tilde{Q}_i \tilde{A}_i^T + \tilde{B}_i \tilde{B}_i^T \right) \right]. \tag{2.33}$$

The partial derivatives of J_a with respect to the variable matrices, A_c, B_c, and C_c, are derived as follows:

$$\begin{aligned}
\frac{\partial J_a}{\partial A_c} &= \sum_{i=1}^{n_{DP}} \beta_i [(QP)_{22}^T + (PQ)_{22}]_i && (2.34) \\
\frac{\partial J_a}{\partial B_c} &= \sum_{i=1}^{n_{DP}} \beta_i [\{(QP)_{12}^T + (PQ)_{21}\} C_y^T - \{(QP)_{22}^T + (PQ)_{22}\} C_c^T D_{yu}^T \\
&\quad + (P_{12}^T + P_{21}) B_w D_{yw}^T + (P_{22}^T + P_{22}) B_c D_{yw} D_{yw}^T]_i && (2.35) \\
\frac{\partial J_a}{\partial C_c} &= \sum_{i=1}^{n_{DP}} \beta_i [D_{zu}^T D_{zu} C_c (Q_{22}^T + Q_{22}) - D_{zu}^T C_z (Q_{21}^T + Q_{12}) \\
&\quad - B_u^T \{(QP)_{21}^T + (PQ)_{12})\} - D_{yu}^T B_c^T \{(QP)_{22}^T + (PQ)_{22}\}]_i, && (2.36)
\end{aligned}$$

where $(\cdot)_{11}, (\cdot)_{12}, (\cdot)_{21}$, and $(\cdot)_{22}$ are $n_x \times n_x$ matrix entries of the indicated matrix. For instance,

$$PQ = \begin{bmatrix} (PQ)_{11} & (PQ)_{12} \\ (PQ)_{21} & (PQ)_{22} \end{bmatrix}.$$

Refer to Appendix A for the derivations of the derivatives.

For the optimum solution of the matrix set, the following partial derivative has to be zero. That is,

$$\frac{\partial J_a}{\partial \tilde{Q}_i} = \tilde{P}_i \tilde{A}_i + \tilde{A}_i^T \tilde{P}_i + \tilde{C}_i^T \tilde{C}_i = 0. \tag{2.37}$$

This is another Lyapunov equation with respect to the Lagrange multipliers, $\tilde{P}_i$. The solution, $\tilde{P}_i$, is used to evaluate the partial derivatives, Equation (2.34), Equation (2.35), and Equation (2.36).

2.2.2 Design Strategy

Since there is no analytical solution of the MM problem, numerical optimization methods, such as the Newton method and the quasi-Newton method, need to be used to get the optimum solution, which minimizes the weighted sum of the LQG costs. In either method, an adequate initial matrix set, A_{c0}, B_{c0}, and C_{c0}, has to be chosen to start the iterative calculation. The LQG solution can be used as the initial matrix set as long as it is stable for each design point. In this study, the following procedure is adopted to obtain the MM solution.

1. An LQG solution is chosen as an initial matrix set. Therefore, the design parameters, such as the state, control, and filter weights, are the same as those used to find the LQG compensator. The LQG solution is obtained by following the procedure described in Section 2.1.2.

2. Set the cost weights, β_i. A heavier cost weight gives a wider stable region around the corresponding design point.

3. All closed loop systems in the MM design procedure, which consist of the plant system at each design point and the compensator in the middle of the iterative calculation, must be stable. Therefore, at the start of the calculation, temporary off-nominal design points, which are inside of the stable region around the nominal design point provided by the initial compensator, need to be set. The optimum solution of this temporary design step expands the stable region around the nominal design point, and then can be used as the initial matrix set for the next design step. In the next design step, the temporary off-nominal design points are moved toward the final off-nominal design points. The solution for the final off-nominal design point is the targeted MM solution.

The design procedure described above is called the progressive method. This method can be one of the measures to avoid obtaining local minima in the numerical optimization process instead of the global minimum. In this study, the effectiveness of this method is also examined.

2.3 Sample Designs

The sample control design is posed in order to investigate basic properties of the plant system and the compensators designed with the LQG technique and the MM technique. The most important thing in the sample design is to understand the mechanism of destabilization of the closed loop system due to the frequency uncertainty of the plant system.

The plant system in the sample design should be as simple as possible without losing its basic properties. A single input and single output (SISO) plant system of a free-free flexible beam is selected as the sample plant system.

2.3.1 Plant System for the Sample Designs

The Middeck Active Control Experiment (MACE) test article was developed as a typical model of a future flexible space structure system, such as space stations and space platforms. The main feature of this type of system is lightly damped structural dynamics. Poles and zeros of the plant system are alternately and successively located near the imaginary axis on the left half of the complex plane. This pole-zero location is deeply related to stability of the closed loop system.

In order to study this basic plant dynamic feature and compensators designed with LQG and MM, a free-free beam is selected in the sample designs. The free-free beam has similar physical properties to those of the MACE test article, such as mass distribution and stiffness of the struts. This beam, however, does not have gimbals like attached to the MACE test article.

The model for the sample design needs to have a few modes at least to examine the lightly damped pole-zero structure. The plant system selected in the sample designs is modeled in the X-Y plane, and has four Z-bending modes. The Finite Element Method (FEM) is used to develop the analytical model of the free-free beam [18].

The sample model consists of four flexible struts, one heavier center node mass, two intermediate node masses, and two end node masses. The masses are modeled

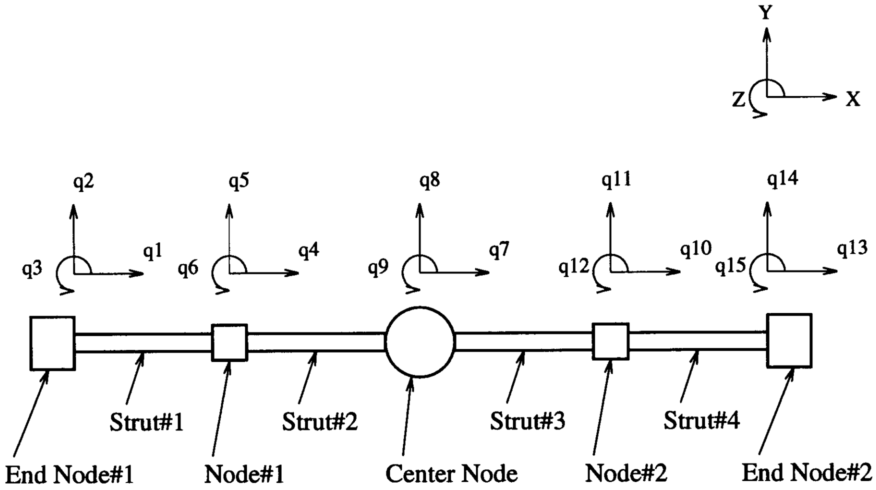

Figure 2-2: Sample model; 4-mode free-free flexible beam

as rigid. Figure 2-2 shows the sample model, and Table 2.1 shows physical values of the sample model. The flexible struts have similar physical properties to those of the MACE test article.

As shown in Figure 2-2, each strut has a reference point at each end, and each reference point has three degrees of freedom resulting in six degrees of freedom for each strut (x_1, y_1, ψ_1, x_2, y_2, and ψ_2). Each rigid mass has three degrees of freedom (x_r, y_r, and ψ_r), which correspond to the degrees of freedom of the struts by connecting it to the ends of the struts. The 4-mode free-free flexible beam is assembled from these elements as illustrated in Figure 2-2 and has 15 degrees of freedom. Eventually, four Z-bending modes are extracted by truncating the 11 other modes.

The equations of motion in the physical reference coordinates are given by

$$\left[\overline{M}\right]\ddot{\overline{q}} + \left[\overline{C}\right]\dot{\overline{q}} + \left[\overline{K}\right]\overline{q} = \overline{F}, \tag{2.38}$$

where $\overline{q}$ is the displacement variable vector, $[A_i]$ is the geometry matrix of i-th element, and

$$\left[\overline{M}\right] = \sum [A_i]^T [\overline{m}_i] [A_i]$$

Table 2.1: Physical values of the 4-mode free-free flexible beam

item	symbol	values
Center Node : Mass	M_C	14.35 kg
Moment of Inertia (Z-axis)	I_{zC}	2.038×10^{-1} $kg\,m^2$
Intermediate Nodes : Mass	M_{Nj} $(j = 1, 2)$	1.300 kg
Moment of Inertia (Z-axis)	I_{zNj} $(j = 1, 2)$	9.521×10^{-3} $kg\,m^2$
End Nodes : Mass	M_{Ej} $(j = 1, 2)$	7.062 kg
Moment of Inertia (Z-axis)	I_{zEj} $(j = 1, 2)$	1.014×10^{-1} $kg\,m^2$
Struts : Density	ρ_j $(j = 1, 2, 3, 4)$	3099 kg/m^3
Length	L_j	0.2643 m
Modulus of Elasticity	E_j	2.578×10^9 N/m^2
Cross-sectional Area Moment of Inertia	I_{zj}	2.140×10^{-8} m^4
Cross-sectional Area	A_j	2.560×10^{-4} m^2

$$\begin{aligned} \left[\overline{C}\right] &= \sum [A_i]^T [\overline{c}_i] [A_i] \\ \left[\overline{K}\right] &= \sum [A_i]^T \left[\overline{k}_i\right] [A_i] \\ \overline{F} &= \sum [A_i]^T \overline{f}_i. \end{aligned} \tag{2.39}$$

The mass $[\overline{m}_i]$ and stiffness $\left[\overline{k}_i\right]$ matrices for the flexible struts in the X-Y plane are given by

$$[\overline{m}_i] = \frac{mL}{420} \begin{bmatrix} 140 & 0 & 0 & 70 & 0 & 0 \\ 0 & 156 & 22L & 0 & 54 & -13L \\ 0 & 22L & 4L^2 & 0 & 13L & -3L^2 \\ 70 & 0 & 0 & 140 & 0 & 0 \\ 0 & 54 & 13L & 0 & 156 & -22L \\ 0 & -13L & -3L^2 & 0 & -22L & 4L^2 \end{bmatrix} \tag{2.40}$$

$$\left[\overline{k}_i\right] = \frac{EI}{L^3}\begin{bmatrix} \left(\frac{L}{r}\right)^2 & 0 & 0 & -\left(\frac{L}{r}\right)^2 & 0 & 0 \\ 0 & 12 & 6L & 0 & -12 & 6L \\ 0 & 6L & 4L^2 & 0 & -6L & 2L^2 \\ -\left(\frac{L}{r}\right)^2 & 0 & 0 & \left(\frac{L}{r}\right)^2 & 0 & 0 \\ 0 & -12 & -6L & 0 & 12 & -6L \\ 0 & 6L & 2L^2 & 0 & -6L & 4L^2 \end{bmatrix}, \tag{2.41}$$

where r is the radius of gyration of the cross-sectional area and is given by $r = \sqrt{\frac{I_m}{A}}$. I_m is the cross-sectional area moment of inertia, and A is the cross-sectional area.

The damping matrices, $[\overline{c}_i]$, for the flexible elements are easily determined by using the modal coordinates introduced later.

The $[\overline{m}_i]$, $[\overline{c}_i]$, and $\left[\overline{k}_i\right]$ matrices for the rigid mass elements in the X-Y plane are given by

$$[\overline{m}_i] = \begin{bmatrix} m_r & 0 & 0 \\ 0 & m_r & 0 \\ 0 & 0 & I_z \end{bmatrix} \tag{2.42}$$

$$[\overline{c}_i] = [0]_{(3\times3)} \tag{2.43}$$

$$\left[\overline{k}_i\right] = [0]_{(3\times3)} \tag{2.44}$$

The physical reference coordinates are intuitive for understanding physical motion of the beam. They, however, are not suitable for control design for the plant with parametric uncertainties in the natural frequencies of its bending modes, because modal information is implicitly contained in the system matrices of the state equations. The modal coordinates are more convenient in designing compensators for the flexible structure system because the system matrices are expressed with modal parameters explicitly.

The transformation with the mode shape matrix, Φ, defined below gives the following equations of motion in modal coordinates.

$$I\ddot{\overline{\eta}} + 2\,[\zeta]\,[\Omega]\,\dot{\overline{\eta}} + [\Omega]^2\,\overline{\eta} = \Phi^T\overline{F}, \tag{2.45}$$

where $\overline{\eta}$ is a modal variable vector and

$$\begin{aligned} [\zeta] &= diag(\zeta_j) \\ [\Omega] &= diag(\omega_{Nj}). \end{aligned}$$

The $diag(\cdot)$ indicates a square matrix which has a specified vector as diagonal entries. ζ_j and ω_{Nj} denote the damping ratios and the natural frequencies of the j-th Z-bending mode of the sample plant, respectively. Since the sample model has four modes, $[\zeta]$ and $[\Omega]$ are 4×4 matrices in the sample designs in this section.

The mode shape matrix, Φ, needs to satisfy the following relations:

$$\begin{aligned} \overline{q} &= \Phi\overline{\eta}; \\ \Phi^T \left[\overline{M}\right] \Phi &= I; \\ \Phi^T \left[\overline{C}\right] \Phi &= 2\,[\zeta]\,[\Omega]\,; \\ \Phi^T \left[\overline{K}\right] \Phi &= [\Omega]^2\,. \end{aligned} \tag{2.46}$$

Now each mode can be explicitly specified.

The linear, time-invariant state equations based on the modal variables can be derived from the equations of motion, Equation (2.45).

$$\begin{aligned} \frac{d}{dt}\begin{bmatrix} \overline{\eta} \\ \dot{\overline{\eta}} \end{bmatrix} &= \begin{bmatrix} 0 & I \\ -\Omega^2 & -2\zeta\Omega \end{bmatrix}\begin{bmatrix} \overline{\eta} \\ \dot{\overline{\eta}} \end{bmatrix} + \begin{bmatrix} 0 \\ \Phi^T b \end{bmatrix} u \\ y &= \begin{bmatrix} C_d\Phi & 0 \\ 0 & C_r\Phi \end{bmatrix}\begin{bmatrix} \overline{\eta} \\ \dot{\overline{\eta}} \end{bmatrix}, \end{aligned} \tag{2.47}$$

where $\overline{F} = bu$, and u is a control variable. C_d and C_r correspond to the displacement and rate sensors, respectively.

In this representation of the state equations, the A matrix for the actual system with uncertainties in natural frequencies is given by

$$A_a = A + \Delta A = \begin{bmatrix} 0 & I \\ -\Omega^2 & -2\zeta\Omega \end{bmatrix} + \begin{bmatrix} 0 & 0 \\ -2\Omega(\delta\Omega) - (\delta\Omega)^2 & -2\zeta(\delta\Omega) \end{bmatrix}, \tag{2.48}$$

where $(\delta\Omega) = diag(\delta\omega_{Nj})$.

Since a typical value of damping ratios, ζ_j, of the space structure is in the order of 0.01, the uncertainty matrix, ΔA, behaves in a manner of a rank 1 matrix. This implies loss of exact information of the uncertainties.

On the other hand, the following representation enables the uncertainty matrix to keep rank 2. Therefore, the exact information of the uncertainties can be kept.

$$A = \begin{bmatrix} -\zeta\Omega & \Omega\sqrt{I-\zeta^2} \\ -\Omega\sqrt{I-\zeta^2} & -\zeta\Omega \end{bmatrix}, \tag{2.49}$$

where $\sqrt{I-\zeta^2} = diag(\sqrt{1-\zeta_j^2})$.

Then, the actual A matrix is given by

$$\begin{aligned} A_a &= A + \Delta A \qquad (2.50) \\ &= \begin{bmatrix} -\zeta\Omega & \Omega\sqrt{I-\zeta^2} \\ -\Omega\sqrt{I-\zeta^2} & -\zeta\Omega \end{bmatrix} + \begin{bmatrix} -\zeta(\delta\Omega) & (\delta\Omega)\sqrt{I-\zeta^2} \\ -(\delta\Omega)\sqrt{I-\zeta^2} & -\zeta(\delta\Omega) \end{bmatrix}. \end{aligned}$$

The introduction of a new state variable vector, $\bar{\xi} = T\bar{\eta}$, gives the following new state equations.

$$\begin{aligned} \frac{d}{dt}\begin{bmatrix} \bar{\xi} \\ \dot{\bar{\xi}} \end{bmatrix} &= \begin{bmatrix} -\zeta\Omega & \Omega\sqrt{I-\zeta^2} \\ -\Omega\sqrt{I-\zeta^2} & -\zeta\Omega \end{bmatrix}\begin{bmatrix} \bar{\xi} \\ \dot{\bar{\xi}} \end{bmatrix} + T^{-1}\begin{bmatrix} 0 \\ \Phi^T b \end{bmatrix} u \qquad (2.51) \\ y &= \begin{bmatrix} C_d\Phi & 0 \\ 0 & C_r\Phi \end{bmatrix} T \begin{bmatrix} \bar{\xi} \\ \dot{\bar{\xi}} \end{bmatrix}, \end{aligned}$$

Table 2.2: Z-bending modes of the 4-mode free-free flexible beam

Description	Nominal Frequency [Hz]	Nominal Damping Ratio
1st mode	2.50	0.01
2nd mode	6.79	0.01
3rd mode	10.97	0.01
4th mode	12.93	0.01

Table 2.3: Z-bending modes of the nominal 0-g model of the MACE test article

Description	Nominal Frequency [Hz]	Nominal Damping Ratio
1st Z bending	1.94	0.022
2nd Z bending	10.51	0.503
3rd Z bending	12.69	0.149
4th Z bending	39.19	0.022

(Note) Reproduction from the reference [32]

where T is a similar transformation matrix and given by

$$T = \begin{bmatrix} I & I \\ -\zeta - \Omega\sqrt{I-\zeta^2} & -\zeta + \Omega\sqrt{I-\zeta^2} \end{bmatrix}.$$

The natural frequencies and damping ratios of the four modes are shown in Table 2.2. The natural frequencies of the first three modes reasonably correspond to those of the first three Z-bending modes of the 0-g FE model of the MACE test article shown in Table 2.3 [32]. All damping ratios of the sample plant system are set at 0.01, which is a typical value of this type of structural system.

Table 2.4 summarizes the configuration of the SISO plant system of the 4-mode free-free flexible beam model. The plant has a collocated disturbance input and performance output.

The Bode plots of the SISO plant system are shown in Figure 2-3. Four tall

Table 2.4: Configuration of the SISO plant system of the 4-mode free-free flexible beam

item	contents
Order of the system	8 (4 Z-bending modes)
Control input	Torque about Z axis at the end node #1
Sensor output	Inertial angle, q_3, about Z axis at the end node #1
Disturbance input	Disturbance torque about Z axis at the end node #1 (collocated at the same position of the control input)
Performance output	Inertial angle, q_3, about Z axis at the end node #1 (collocated at the same position of the sensor output)

peaks and three deep valleys are observed. This is a typical property of a lightly damping structure system. The phase is bounded between $0deg$ and $-180deg$. The Bode plots of the plant system perturbed in the second bending mode frequency by ±20% are also shown in Figure 2-3. The first and second zeros are also affected by the perturbation of the second bending mode, while the third zero is scarcely affected.

Figure 2-4 shows the pole-zero location of the plant system. The poles and zeros are placed near the imaginary axis in the left of the complex plane. The pole-zero pattern is easily identified.

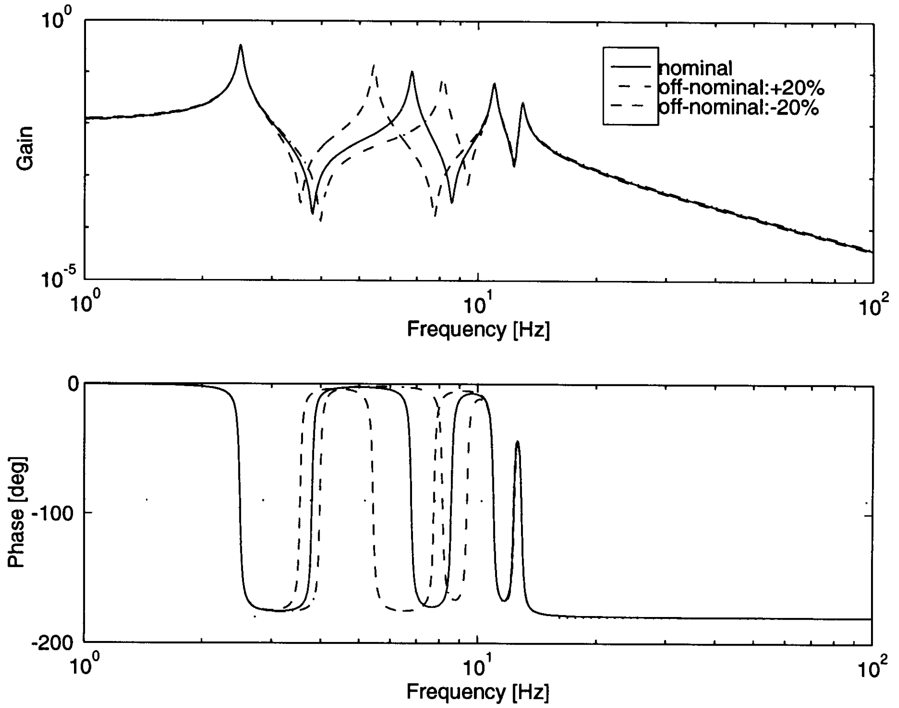

Figure 2-3: Bode plot of the 4-mode free-free flexible beam

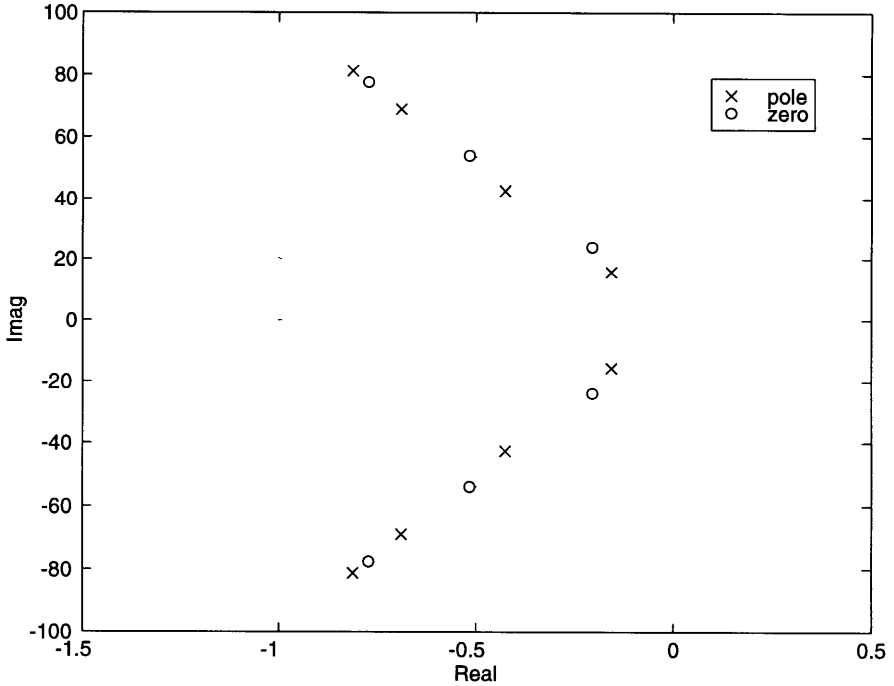

Figure 2-4: Pole-zero location of the 4-mode free-free flexible beam

2.3.2 Analysis Tools

In designing compensators, designers need to have adequate analysis tools to examine properties of the plant system and the compensators. Compensators need to be examined with respect to performance, stability, and sensitivity. In particular, a MIMO design needs effective analysis tools, while a SISO design has mature tools such as the Bode plot. The following introduces the analysis tools used to examine each property.

1. Performance : Frequency Responses and Performance Gain

   Performance consists of two categories: nominal performance and robust performance. The nominal performance of compensators can be indicated by the comparison between frequency responses of the open loop transfer function matrix from the disturbance vector, w, to the performance vector, z, and the closed loop transfer function matrix from w to z: $|G_{zw}(j\omega)|$ and $|G_{cl0}(j\omega)|$. Note that the subscript $(\cdot)_0$ implies that the control contribution to the LQG cost is eliminated to leave only a state cost by setting $D_{zu} = 0$ in Equation (2.5).

   The difference between the closed loop state cost and the open loop state cost indicates the total performance of the compensator. This value is called performance gain. The performance gain P_G is defined as

$$P_G = P_{CL} - P_{OL}. \tag{2.52}$$

   The state costs are given by

$$\begin{aligned} \text{Closed Loop State Cost : } P_{CL} &= \left[\frac{1}{2\pi} trace \int_{-\infty}^{+\infty} G_{c0}(i\omega) G^*_{c0}(i\omega)\, d\omega\right]^{1/2} \\ &= \left[trace\left\{\tilde{C}_0 \tilde{Q} \tilde{C}_0\right\}\right]^{1/2} \end{aligned} \tag{2.53}$$

$$\begin{aligned} \text{Open Loop State Cost : } P_{OL} &= \left[\frac{1}{2\pi} trace \int_{-\infty}^{+\infty} G_{zw}(i\omega) G^*_{zw}(i\omega)\, d\omega\right]^{1/2} \\ &= \left[trace\left\{C_z Q_{zw} C_z\right\}\right]^{1/2}, \end{aligned} \tag{2.54}$$

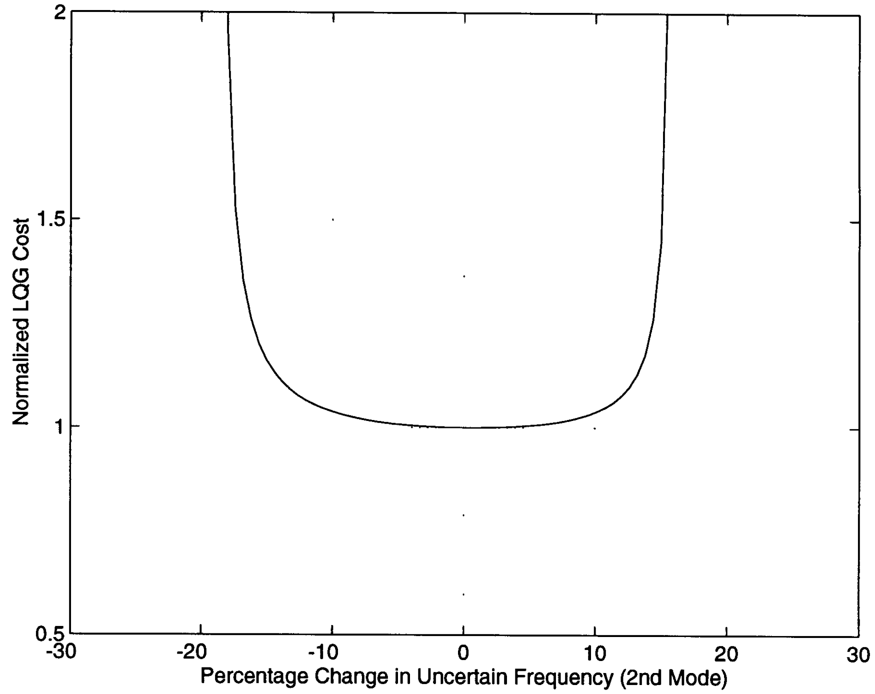

Figure 2-5: Example of the LQG cost plot

where $\tilde{Q}$ is the solution of the Lyapunov equation, Equation (2.10), and Q_{zw} is the solution of the following Lyapunov equation for the open loop system, $G(s)_{zw}$.

$$AQ_{zw} + Q_{zw}A + B_w B_w^T = 0 \tag{2.55}$$

2. Performance : LQG cost *versus* off-nominal parameter plot

   If an off-nominal factor can be represented with one parameter, LQG costs can be plotted as a function of the off-nominal parameter. This LQG cost plot provides information on robust stability and performance of the compensator. Figure 2-5 shows an example of the LQG cost plot. The LQG costs are normalized with the nominal LQG cost. The flat part of the plot around the nominal point means that the compensator can keep its nominal performance in this region of off-nominal parameter. The wider this flat part is, the better robust performance the compensator has. The closed loop system is unstable for the off-nominal parameter outside of the bucket-shaped plot.

However, the LQG cost plot shows robustness of compensators with respect to only one off-nominal parameter. If plant systems have several off-nominal factors, which cause a multiplier effect in degrading the closed loop systems, other analysis methods, such as μ-analysis [33, 34], need to be used.

3. Stability : Nichols Plot

   The Bode plot and Nyquist plot provide information on stability and stability margin of control systems, but can be applied to only single-input and single-output (SISO) plant systems. However, real plant systems usually have more than one input and output. The Nichols plot based on the Multivariable Nyquist Criterion for stability provides information on stability of multiple-input and multiple-output (MIMO) control systems [35, 36].

The Multivariable Nyquist Criterion [35]

The closed loop system is stable if and only if the number of counter-clockwise encirclements of the critical point,(-1, 0), by ,

$$\mathcal{N}(s) = -1 + det[I + G_{yu}(s)K(s)] \qquad s \in D_r \qquad (2.56)$$

is equal to the number of unstable poles of $G_{yu}(s)K(s)$*, where* D_r *is the Nyquist contour.*

$\mathcal{N}(s)$ is called the Multivariable Nyquist function. In the SISO case, this criterion results in the conventional Nyquist Criterion for SISO control systems.

Plotting the Multivariable Nyquist function in terms of logarithmic magnitude versus phase allows designers to distinguish the locus of the function much more easily. This type of plot is called the Multivariable Nichols plot or simply the Nichols plot. Note that the Nichols plot has multiple critical points located at a magnitude of 1 with phase of $-180 \pm 360n deg$, $(n = 0, 1, 2, \ldots)$, while the

Nyquist plot only has one critical point.

The Multivariable Nyquist Criterion needs to be modified for the Nichols plot as follows:

> *The closed loop system is stable if and only if the number of left to right passes over the critical points is equal to the number of unstable poles* $G_{yu}(s)K(s)$.

In the case of a stable plant and compensator, if the locus does not have passes over the critical points, the closed loop system is stable.

4. Sensitivity : Minimum Singular Value Plot of $I + G_{yu}(j\omega)K(j\omega)$
   In robust control designs, it is important to identify potential destabilizing factors in a closed loop system due to perturbations. Since the Multivariable Nyquist function depends on a determinant operator, Nichols plots cannot provide information on closed loop system's sensitivity to perturbations. A singular value plot of the sensitivity transfer function, $[I + G_{yu}(j\omega)K(j\omega)]^{-1}$, is one of the measures to investigate sensitivity of a system. A large maximum singular value means that the system is sensitive to perturbations at the corresponding frequency. A singular value plot of $I + G_{yu}(j\omega)K(j\omega)$ keeps the property of the sensitivity transfer function. A small minimum singular value of $I + G_{yu}(j\omega)K(j\omega)$ indicates high sensitivity of a system. In particular, this plot is useful if the plots based on a nominal system and an off-nominal system are compared directly. Differences between the plots based on a nominal system and an off-nominal system indicate sensitivity of the closed loop system to the off-nominal factor.

2.3.3 LQG Designs

In the sample design, the order of the state equations is eight, since four bending modes exist. The control system has one input and one output. Consequently, there are eight state weights, one control weight, and one disturbance weight. According to the design strategy mentioned in Section 2.1.2, the eight state weights are set to unity. In addition, the number of the free weights can be reduced to one by applying the Balanced Weight Condition. The resulting weights are listed in Table 2.5. Three design cases are examined in this section; low, middle, and high control authority cases. Smaller control weights or smaller sensor noise intensities give higher authority compensators.

The frequency responses of the compensators for these three cases are shown in Figure 2-6. The higher authority compensator has higher gain in most of the frequency region. This implies that higher authority compensators demand larger control force and quicker response of actuators.

The most significant feature of the compensators for the flexible structure is the pole-zero structure. The poles and zeros of the compensators are orderly placed between a pole and zero of the plant. This pole-zero pattern strongly impacts on the robust stability of the closed loop system under off-nominal conditions [37].

Figure 2-7 shows the pole-zero pattern more clearly and also indicates the movement of the compensator's poles and zeros with changes of the weights. The arrows in Figure 2-7 indicate the movement of the poles and zeros as the control authority

Table 2.5: Summary of the LQG designs for the SISO plant system of the 4-mode free-free flexible beam

Design Case	Weights			Crossover Frequency $[rad/sec]$	Performance Gain $[dB]$	Nominal LQG Cost
Control Authority	State C_z	Control D_{zu} ρ	Sensor Noise D_{yw} θ			
Low	1.0	3.50×10^{-3}	3.5534×10^{-3}	91.7	-11.113	4.478×10^{-2}
Middle	1.0	2.00×10^{-3}	1.7085×10^{-3}	117.6	-13.629	3.440×10^{-2}
High	1.0	1.00×10^{-3}	6.4306×10^{-4}	175.6	-17.715	2.252×10^{-2}

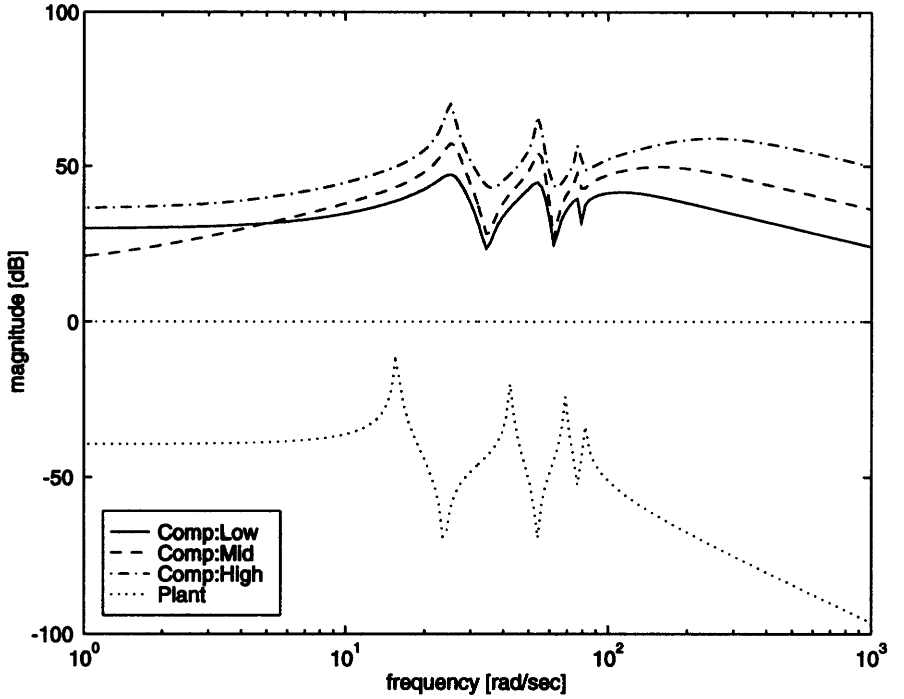

Figure 2-6: Frequency responses of the LQG compensators and the plant system; 4-mode free-free flexible beam

is increased.

Two remarkable distinctions are identified in the movement. The first is that some zeros ('$*$' in Figure 2-7) of the low authority compensator are located in the right half side of the complex plane, making them nonminimum phase, and move into the left half plane with the increase of control authority. The high authority compensator only has minimum phase zeros.

The second distinction is that the compensator's poles move to the plant's minimum phase zeros with the increase in control authority *i.e.* the decrease of the control weight. The third pole at about $79 rad/sec$ of the high authority compensator is placed very close to the third plant zero. This results in pole-zero cancellation. The LQG/LTR (Loop Transfer Recovery) method exploits this characteristic of the LQG compensator to obtain desired closed loop dynamics [5, 6]. The relation between this pole-zero movement and the robustness of the closed loop system is discussed later.

The pole-zero structure of the resulting closed loop system is shown in Figure 2-8. With the separation principle of the LQG compensator, Equation (2.21) and Equa-

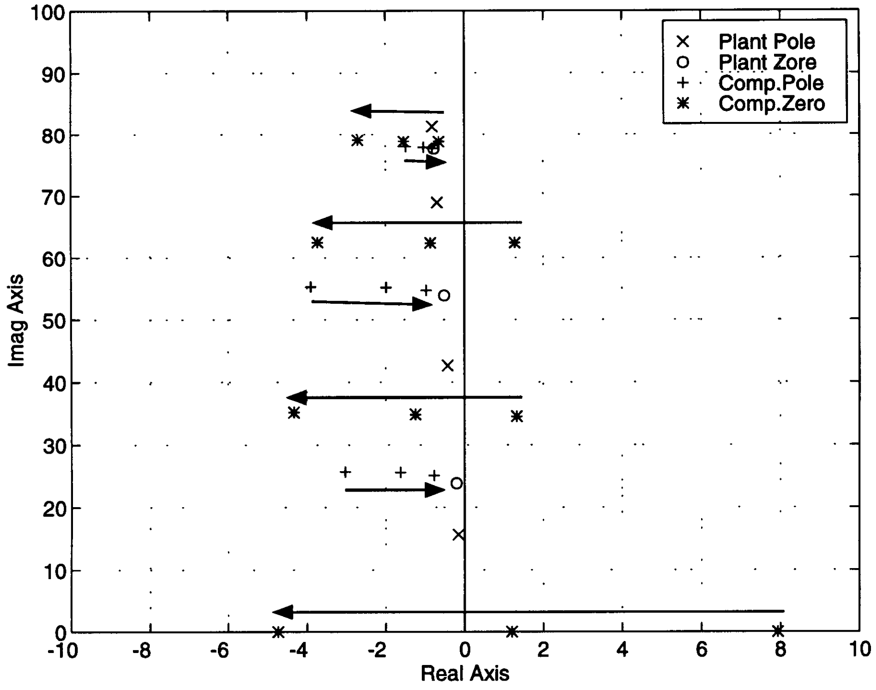

Figure 2-7: Pole-zero location of the plant system and the LQG compensators

tion (2.22), the regulator poles and the filter poles are separately specified in the figure. The regulator poles move in the negative direction parallel to the real axis and exhibit larger damping properties with the increase of the control authority, while the filter poles move in the opposite direction and approach the plant zeros. This movement gives better nominal performance to the high authority compensator. The transmission zeros of the closed loop system are placed at exactly the same positions as the compensators' zeros.

From the frequency responses of the sensitivity transfer function shown in Figure 2-9, the higher authority compensator has better disturbance rejection and command following properties in the frequency region below $100rad/sec$, while it is more sensitive to sensor noises above $100rad/sec$. Table 2.5 shows the crossover frequencies of the three closed loop systems. The crossover frequency is defined here as the frequency at which the magnitude of the complimentary transfer function crosses the $-3dB$ line. As the control authority increases, the crossover frequency gets higher. This means that the higher authority compensator has wider control range in the

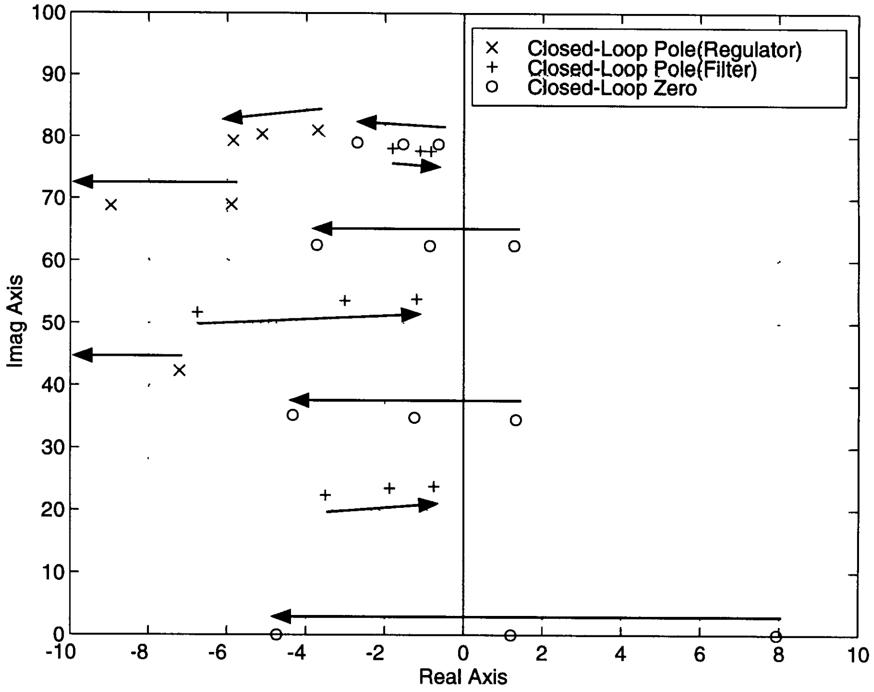

Figure 2-8: Pole-zero location of the closed loop systems with the LQG compensators

frequency region, while it is more sensitive to noise at high frequency.

The frequency response of the open loop transfer functions, $|G_{zw}(j\omega)|$, and the closed loop transfer functions, $|G_{cl0}(j\omega)|$, in Figure 2-10 indicates that the higher authority compensator has better disturbance rejection below $100rad/sec$, while the lower authority compensator has better disturbance rejection above $100rad/sec$. The compensators lower the peaks of the open loop transfer function and make the closed loop system less sensitive to the disturbance at the frequencies corresponding to the peaks. The performance gains listed in Table 2.5 also indicate that the higher authority compensator has better total disturbance rejection performance.

The Bode plots of the loop transfer functions of the three LQG compensators are shown in Figure 2-11. The phase plots of the high and middle authority compensators are bounded between $\pm 180deg$ in the frequency region below $100rad/sec$, while the phase plot of the low authority compensator is not bounded due to the nonminimum phase zeros. This difference between the high and low authority compensators results in different destabilization mechanism for off-nominal factors.

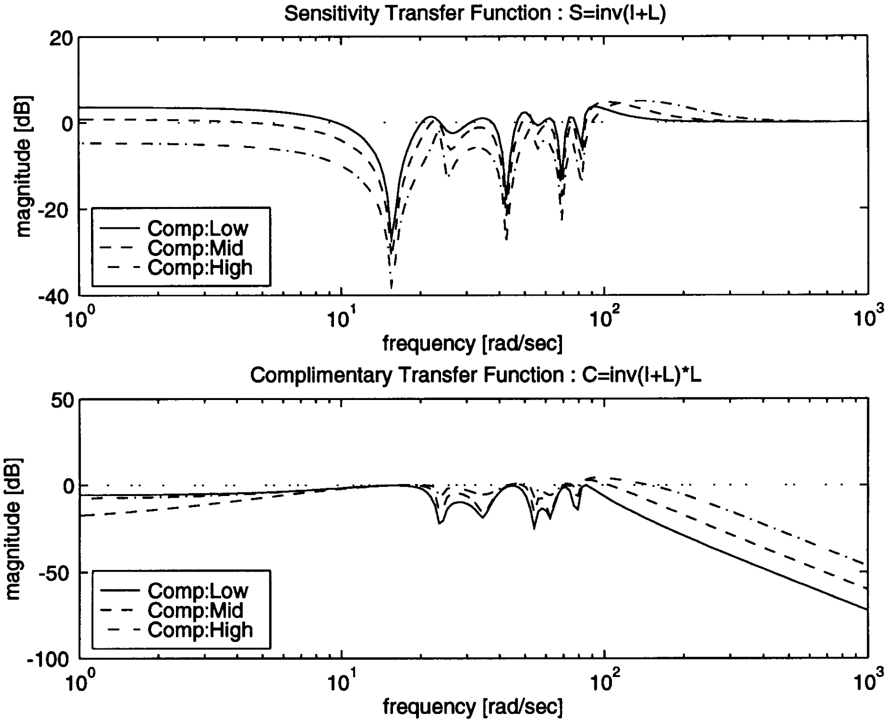

Figure 2-9: Frequency responses of the sensitivity transfer functions and complimentary transfer functions of the LQG compensators

The close-up Bode plot of the low authority compensator is illustrated in Figure 2-12 with plots of off-nominal plants which have ±20% deviations in the second bending mode natural frequency. Closer observation of the nominal plots reveals that there are two frequencies, $35 rad/sec$ and $62 rad/sec$, at which the nominal phase plot crosses $-180deg$ and $-540deg$ critical phases because the nonminimum phase zeros of the compensator are located at $34.6 rad/sec$ and $62.4 rad/sec$. Moreover, these nonminimum phase zeros locally minimize the gain plot and give good gain margins to the closed loop system.

However, if the plant system has -20% frequency uncertainty in the second bending mode, the pole-zero pattern is broken as shown in Figure 2-13. The second plant pole moves below the first compensator zero at $34.6 rad/sec$. The phase plot of the -20% off-nominal case crosses the $-180deg$ critical phase at $34 rad/sec$. The gain at this frequency is greater than $0dB$ due to the deviated second plant pole. Therefore, the closed loop system is destabilized by the frequency uncertainty in the second bending mode.

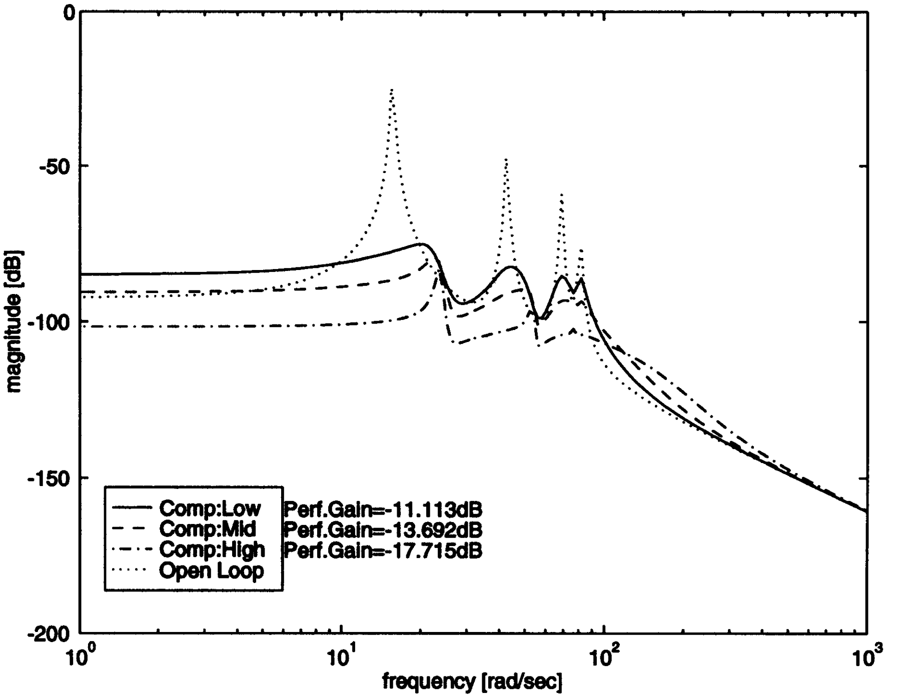

Figure 2-10: Performance of the LQG compensators

On the other hand, if the plant has +20% frequency uncertainty in the second bending mode, the plant second zero lies above the second compensator pole at $55.3rad/sec$. This destruction of the alternating pole-zero pattern does not affect the closed loop system stability significantly, since the second compensator pole is located far enough from the imaginary axis. However, the movement of the second plant pole brings about the phase crossing at $54rad/sec$ before the gain drops below $0dB$ as shown in Figure 2-12. Thus, the closed loop system is destabilized.

Figure 2-17 shows the close-up Bode plot for the high authority compensator case. As observed in the nominal case, the alternating pole-zero pattern makes the phase bounded between $\pm 180deg$, because a pole results in $180deg$ phase loss but then a zero recovers the phase loss promptly. In the high authority compensator case, however, the compensator poles are placed near the plant zeros; all of the compensator poles are located at slightly higher frequencies than the plant zeros as shown in Figure 2-15. Therefore, small positive uncertainties in the plant natural frequencies easily destroy the pole-zero pattern and destabilize the closed loop system. In the +20%

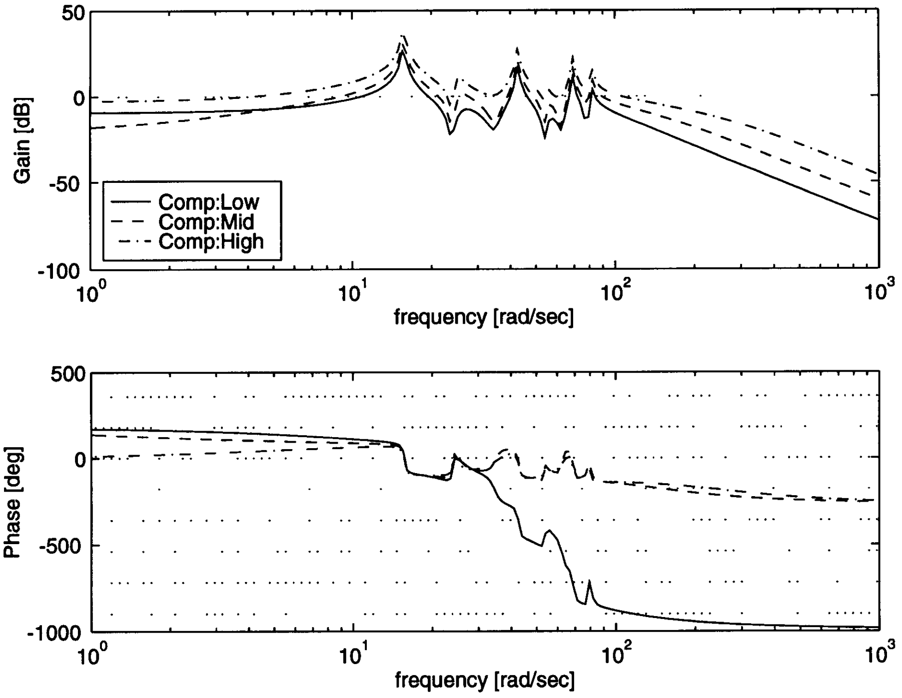

Figure 2-11: Bode plots of the loop transfer functions of the LQG compensators

off-nominal case shown in Figure 2-17, the deviated second plant pole at $51.2 rad/sec$ causes $180 rad/sec$ phase loss, and the second compensator pole successively brings about another $180 rad/sec$ phase loss. And then the phase plot crosses the $-180 deg$ critical phase at $55 rad/sec$ while the gain is greater than $0 dB$.

On the other hand, the closed loop system can stand with relatively larger negative uncertainties, since there is wider room between a plant pole and a lower-frequency compensator zero.

The Nichols plots shown in Figure 2-16 provide the same observation of the destabilization as the Bode plots. However, in multiple-input and multiple-output (MIMO) cases, only the Nichols plot can be used.

The control design trade-off between nominal performance and robustness is discussed in the final part of this section.

There are many trade-offs in control design, such as command following *versus* sensor noise rejection. The trade-off between nominal performance and robustness is a main trade-off in robust control design. In the sample designs, the plot of the

LQG cost with respect to uncertainty in the second bending mode natural frequency shown in Figure 2-17 indicates this trade-off very well. Note that the LQG costs are normalized by the nominal LQG cost of the low authority compensator (4.478×10^{-2}).

From the LQG cost plot, the low authority compensator provides a stable region from -18% to $+16\%$ uncertainty, while the high authority compensator provides from -28% to $+8\%$ uncertainty. The LQG compensator loses the stable region in the positive uncertain frequency as the control authority gets higher. Therefore, the low authority compensator provides better robustness with respect to off-nominal factors. However, the nominal LQG cost of the high authority compensator is half that of the low authority compensator. This means that the high authority compensator provides better nominal performance than the low authority compensator.

Deciding which design factor, robustness or nominal performance, should be given priority depends on model uncertainty and required performance. The problem in the LQG design is that the compensator cannot provide a guarantee of robustness.

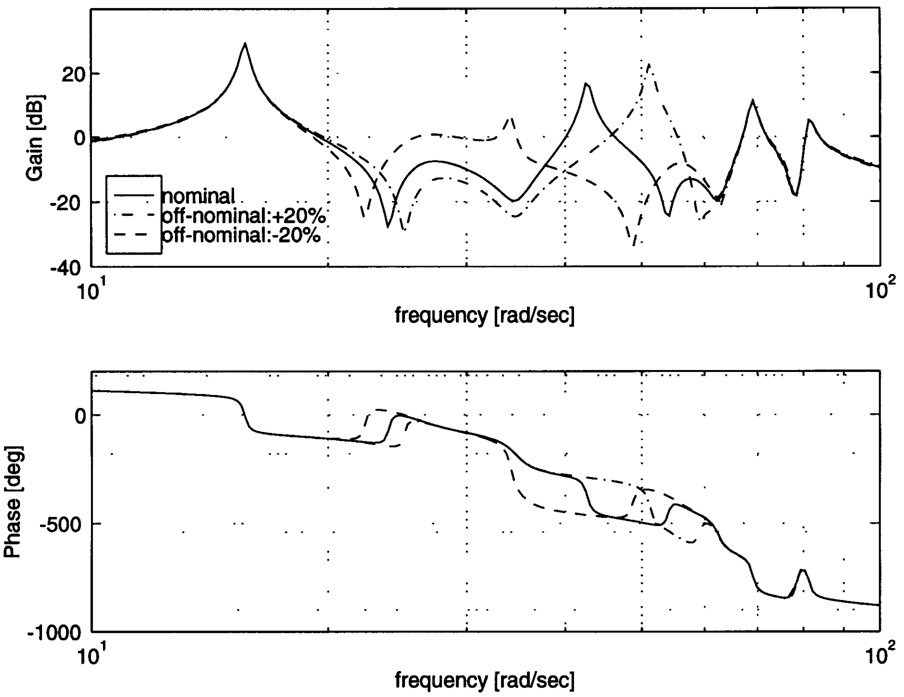

Figure 2-12: Bode plots of the loop transfer functions of the low authority LQG compensator and the plant systems disturbed in the second mode frequency

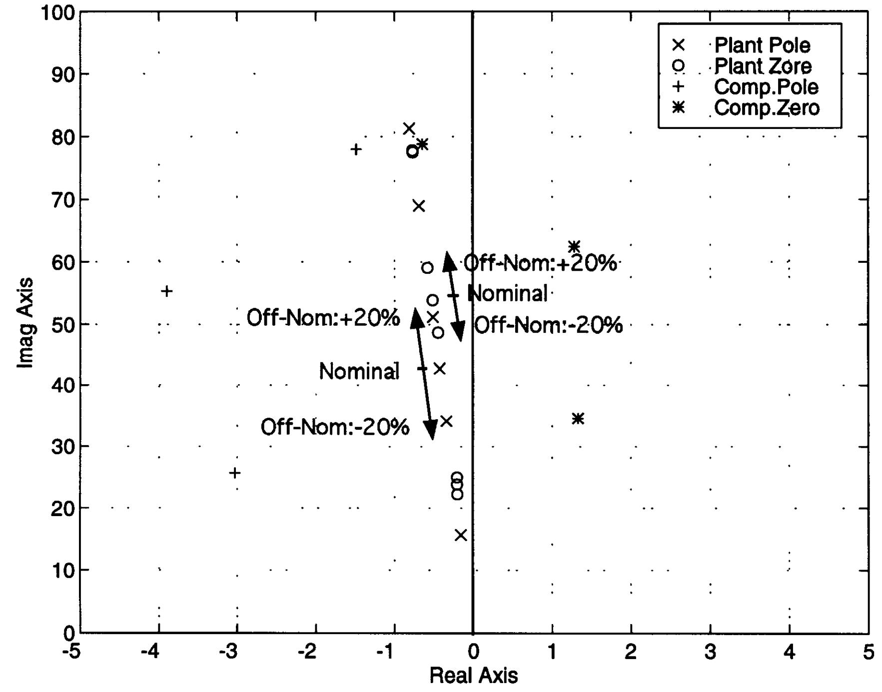

Figure 2-13: Pole-zero location of the low authority LQG compensator and the plant systems disturbed in the second mode frequency

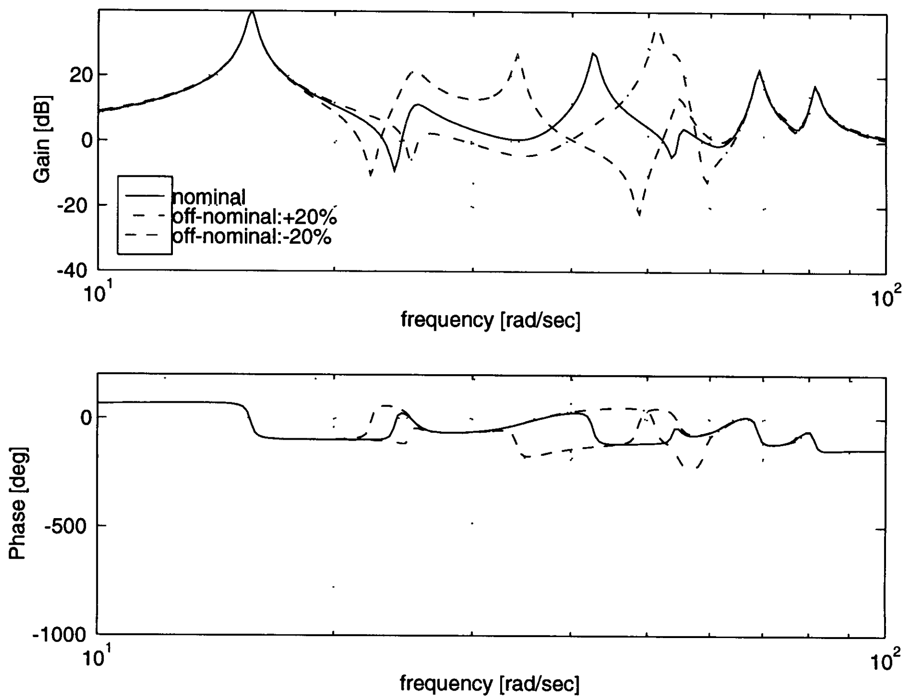

Figure 2-14: Bode plots of the loop transfer functions of the high authority LQG compensator and the plant systems disturbed in the second mode frequency

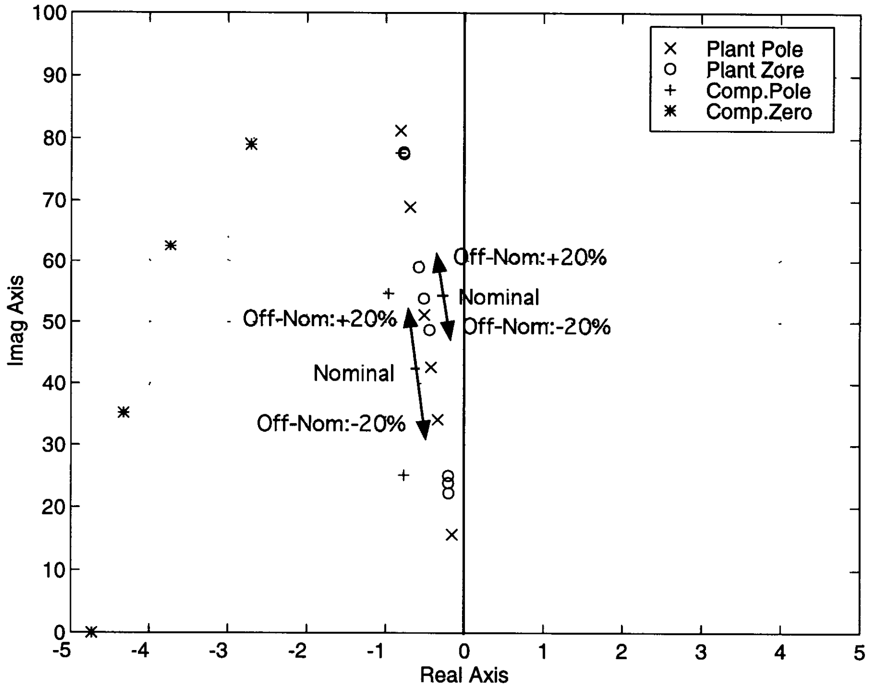

Figure 2-15: Pole-zero location of the high authority LQG compensator and the plant systems disturbed in the second mode frequency

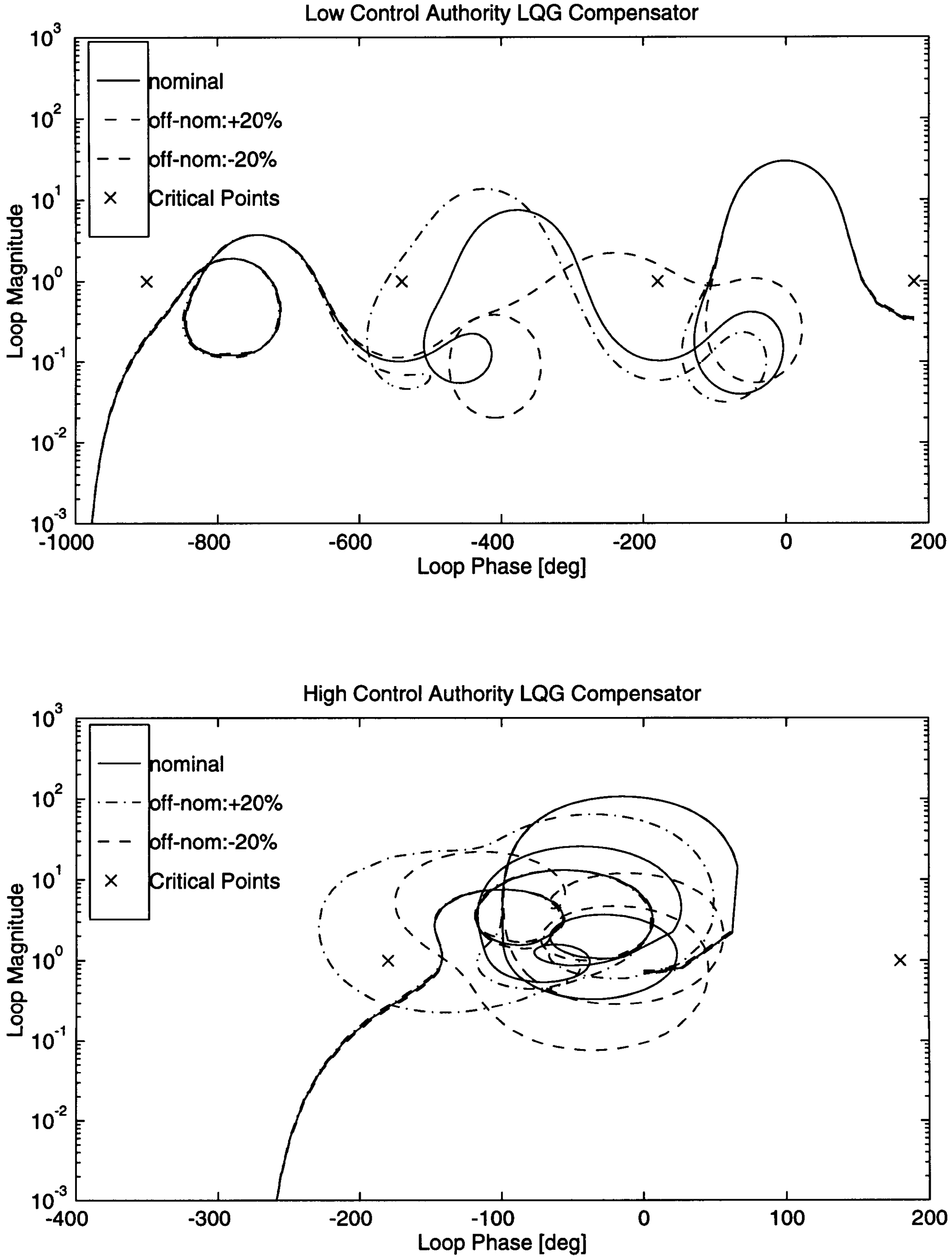

Figure 2-16: Nichols plots of the control system with the low authority LQG compensator and high authority LQG compensator

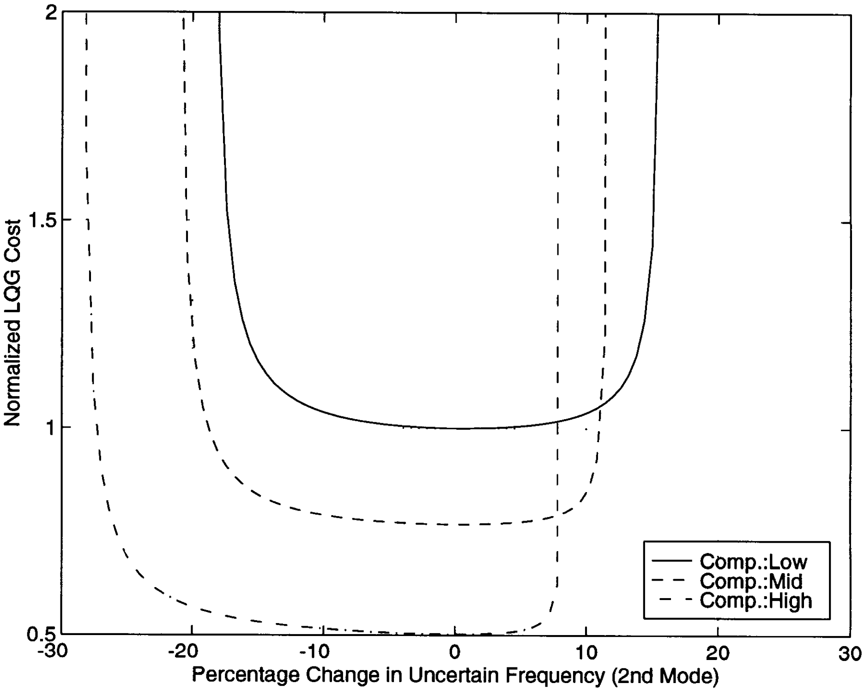

Figure 2-17: LQG costs of the closed loop systems with the LQG compensators

2.3.4 MM Designs

The objective of the Multiple Model (MM) sample designs is to design compensators which provide robust stability for the sample plant system with ±20% frequency uncertainties in the second bending mode.

Two MM compensators are designed and examined. According to the design strategy mentioned in Section 2.2.2, the low and high authority LQG compensator are used as an initial matrix set, A_{c0}, B_{c0}, and C_{c0}. Three design points are set in the MM sample designs: a nominal design point, a negatively deviated off-nominal design point, and a positively deviated off-nominal design point. The maximum frequency deviation from the nominal frequency is ±20%. The cost weights, β_i, are set to 0.9 for the nominal design point and 0.05 for the two off-nominal design points so that the sum of the cost weights is 1.0.

The results of the MM designs are summarized in Table 2.6. The design case of "MM(10%)" means a MM compensator which guarantees stability for the sample plant system with ±10% frequency uncertainties in the second bending mode. The design weights for the MM compensators are the same as those for the LQG compensators used as the initial matrix sets.

Table 2.6: Summary of the MM designs for the SISO plant system of the 4-mode free-free flexible beam

Design Case	Weights			Crossover Frequency	Performance Gain	Nominal LQG Cost
Control Authority	State C_z	Control D_{zu} ρ	Sensor Noise D_{yw} θ	$[rad/sec]$	$[dB]$	
Low : LQG	1.0	3.50×10^{-3}	3.5534×10^{-3}	91.7	−11.113	4.478×10^{-2}
MM(10%)	1.0	3.50×10^{-3}	3.5534×10^{-3}	92.0	−11.121	4.480×10^{-2}
MM(20%)	1.0	3.50×10^{-3}	3.5534×10^{-3}	93.0	−11.086	4.515×10^{-2}
High: LQG	1.0	1.00×10^{-3}	6.4306×10^{-4}	175.6	−17.715	2.252×10^{-2}
MM(10%)	1.0	1.00×10^{-3}	6.4306×10^{-4}	176.5	−17.719	2.257×10^{-2}
MM(20%)	1.0	1.00×10^{-3}	6.4306×10^{-4}	178.7	−17.706	2.273×10^{-2}

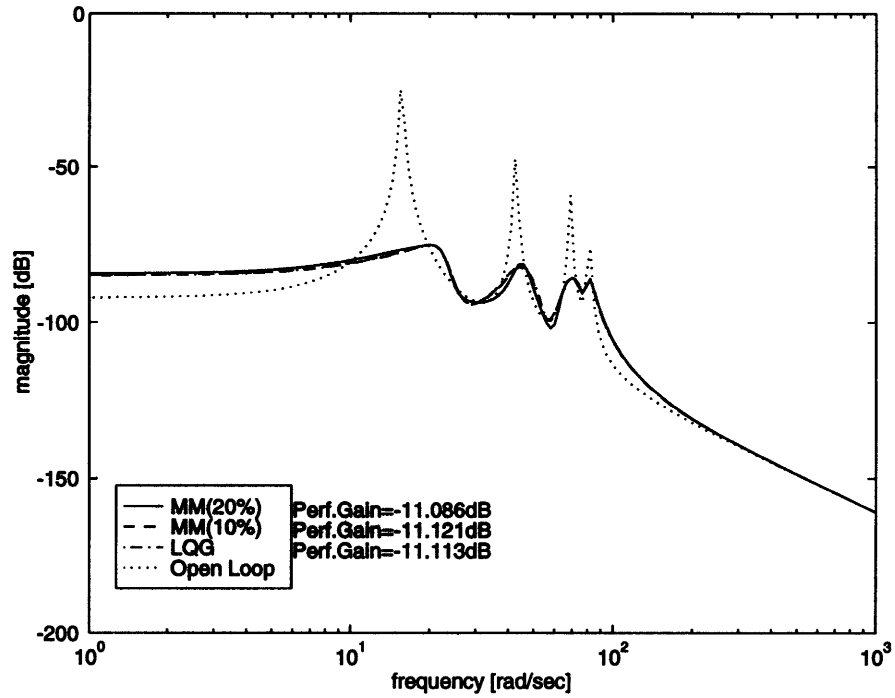

Figure 2-18: Performance of the low authority MM compensator

The crossover frequencies of the MM compensators listed in Table 2.6 get slightly higher as the guaranteed uncertainty bounds are increased. However, the increment is less than 2%. This implies that the MM design maintains the control authority of the original compensator.

The frequency response of the open loop transfer functions, $|G_{zw}(j\omega)|$, and the closed loop transfer functions, $|G_{cl0}(j\omega)|$, is illustrated in Figure 2-18 for the low authority MM compensators and in Figure 2-19 for the high authority MM compensators. The responses in both of the low and high authority designs are almost the same as the response of the original LQG compensators, while there are slight differences around $60 rad/sec$. Moreover, the performance gains are kept constant as shown in Table 2.6. It can be concluded that the MM design also maintains nominal performance of the original compensator.

Figures 2-20 and 2-21 show the movement of the compensator poles and zeros with increases in the frequency uncertainty of the off-nominal design points. In both of the low and high authority designs, the large movements of the second compensator

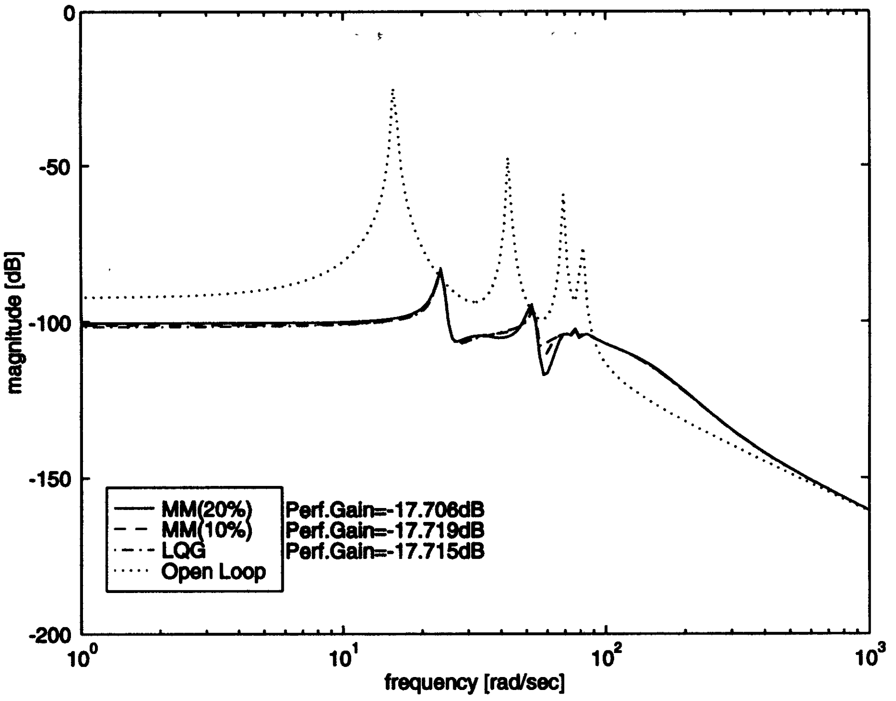

Figure 2-19: Performance of the high authority MM compensator

pole around $55 rad/sec$ and the second and third compensator zeros around $35 rad/sec$ and $62 rad/sec$, respectively, are noticeable. All compensator poles and zeros, except the real zero, move away from the deviated second plant pole in the direction of the imaginary axis.

These pole-zero movements can also be observed in the Bode plots of the nominal loop transfer functions illustrated in Figures 2-22 and 2-23. In the low authority case in Figure 2-22, two deep valleys of the gain plot of the 20% MM compensator at $31.8 rad/sec$ and $63.8 rad/sec$, which the original LQG compensator does not have, correspond to the two nonminimum phase zeros of the 20% MM compensator. These nonminimum phase zeros are located near the imaginary axis and make the phase plot cross the $-180 deg$ and $-540 deg$ critical phases more sharply.

In the high authority case in Figure 2-23, the movement of the second compensator pole, which moves away from the second plant zero, brings about another deep gain valley at $53.9 rad/sec$ and a gain increase around $60 rad/sec$. Larger separation between the second plant zero and the second pole of the 20% MM compensator

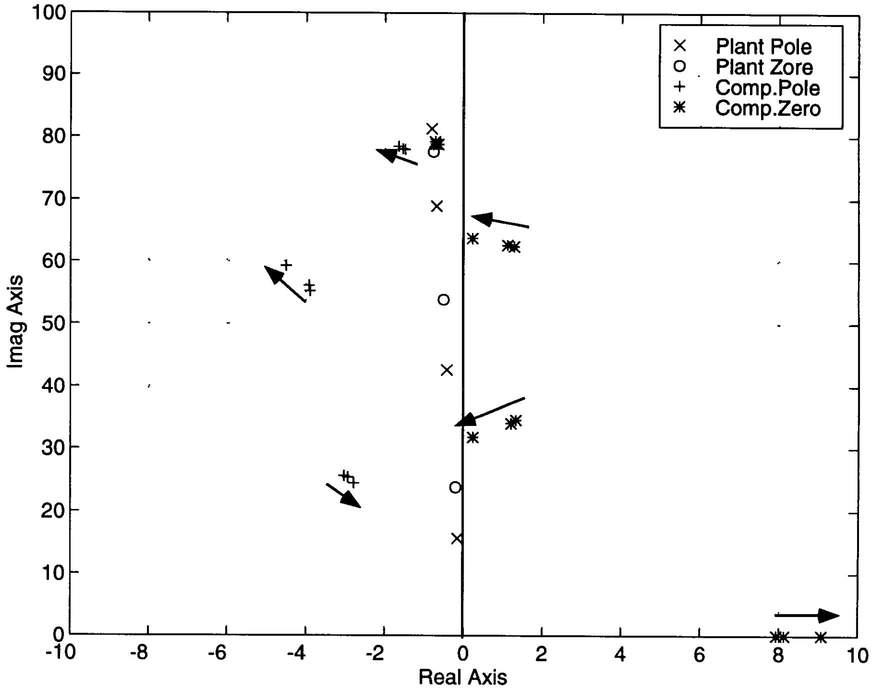

Figure 2-20: Pole-zero location of the plant system and the low authority MM compensators

provides better phase recovery around $55 rad/sec$ than in the case of the LQG compensator.

The robust stability study of the 20% MM compensator in the low authority case is summarized in the Bode plots and the pole-zero locations illustrated in Figure 2-24 and Figure 2-25, respectively. Because the MM design introduces enough separation between a pole and a zero, the pole-zero pattern is not destroyed by the ±20% frequency uncertainties as shown in Figure 2-25. Therefore, the phase plots in the off-nominal cases cross the critical phases with locally minimum and negative gains provided by the compensator nonminimum phase zeros. Furthermore, the phase plot in the +20% off-nominal case does not have the critical phase crossing at $54.0 rad/sec$, which is observed in the low authority LQG compensator case in Figure 2-12. These Bode plots imply that the 20% MM compensator stabilizes the closed loop systems of the off-nominal plants with ±20% frequency uncertainties. Hence, the objective of this sample design has been achieved.

Figure 2-26 and Figure 2-27 show the Bode plots and the pole-zero location in the

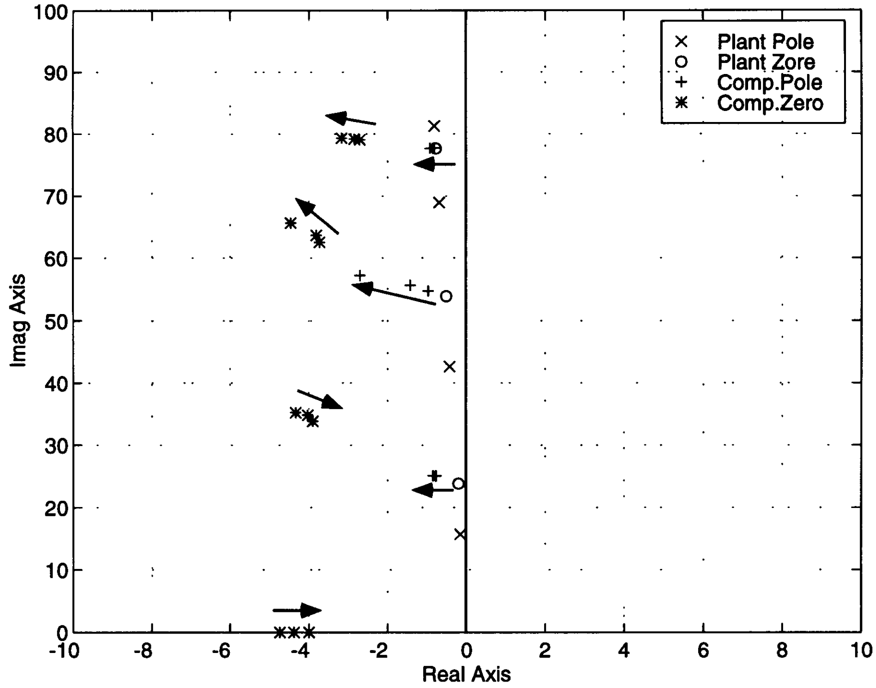

Figure 2-21: Pole-zero location of the plant system and the high authority MM compensators

high authority case. The phase plots in both of the off-nominal cases are bounded between ±180*deg*. This implies that the closed loop systems with the perturbed plant systems are stable. The +20% frequency deviation makes the frequency of the second plant zero higher than that of the second compensator pole as shown in Figure 2-27, and destroys the pole-zero pattern. Recall that the MM design moves the second compensator pole away from the second plant zero. Because of this relatively large separation, the phase plot in the +20% off-nominal case does not have the large phase loss observed in the high authority LQG compensator case in Figure 2-14, and is kept within ±180*deg* boundaries.

The LQG costs of both of the low and high authority cases are shown in Figure 2-28 and Figure 2-29, respectively. The LQG costs are normalized by the nominal LQG costs of the closed loop systems with the original LQG compensators: 4.478×10^{-2} for the low authority case; 2.252×10^{-2} for the high authority case. The 20% MM compensators provide robust stability for the closed loop system with the off-nominal plant which has ±20% frequency uncertainties in the second bending mode. The most remarkable point shown in the LQG cost plots is that the stable region is expanded without large nominal performance loss. The LQG costs of the MM compensators are kept at the same level as the nominal LQG cost of the original LQG compensator within the desired uncertainty region.

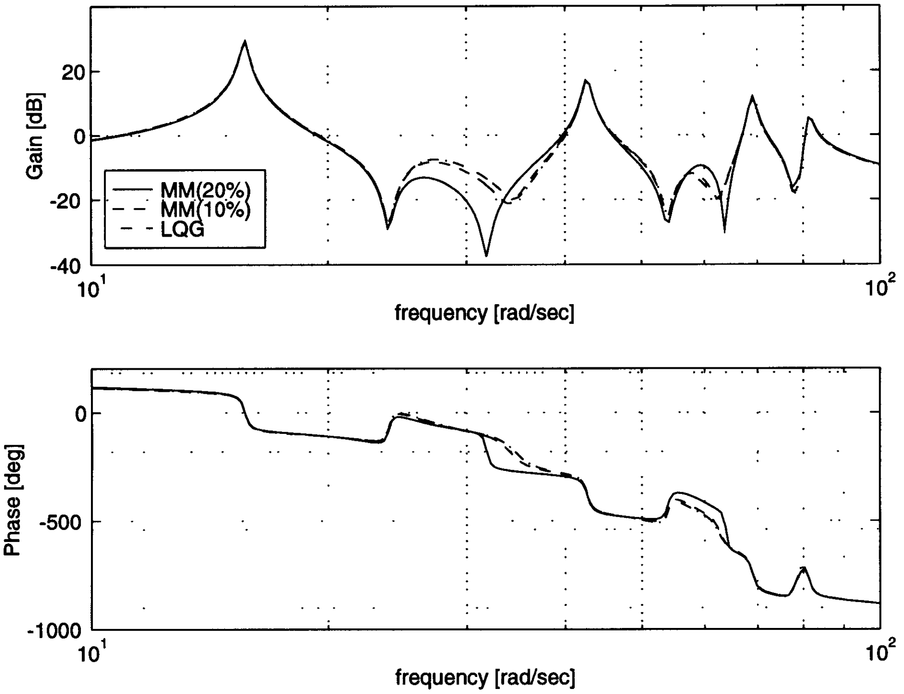

Figure 2-22: Bode plots of the low authority MM compensator

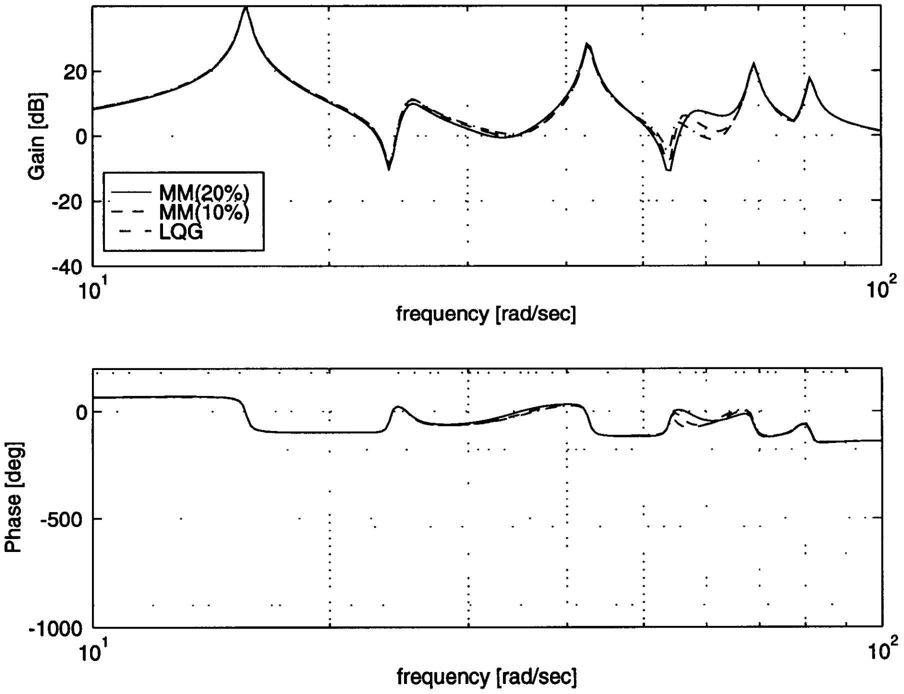

Figure 2-23: Bode plots of the high authority MM compensator

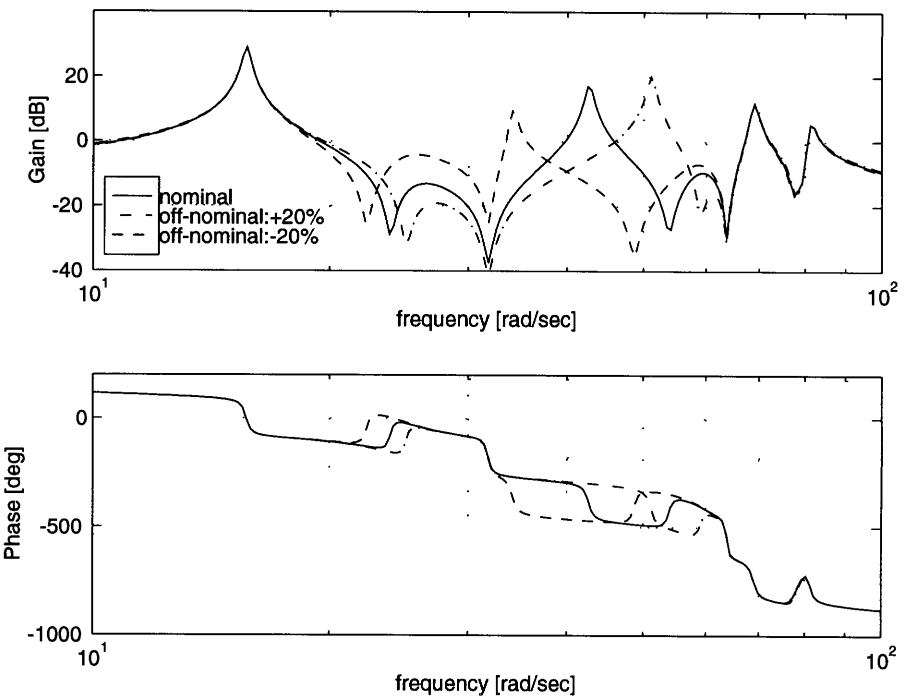

Figure 2-24: Bode plots of the loop transfer functions of the low authority MM compensator and the plant systems disturbed in the second mode frequency

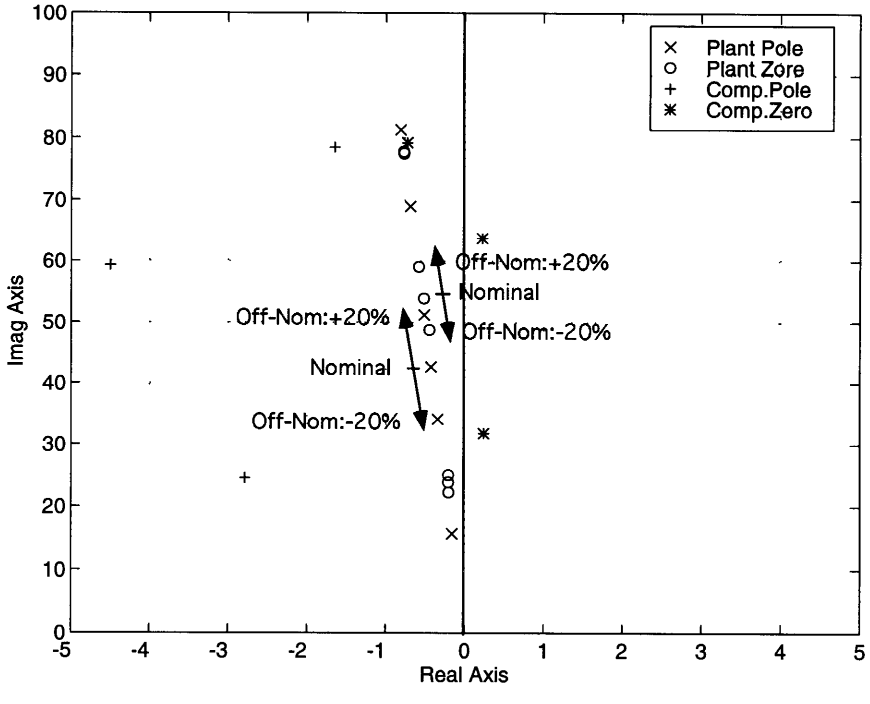

Figure 2-25: Pole-zero location of the low authority MM compensator and the plant systems disturbed in the second mode frequency

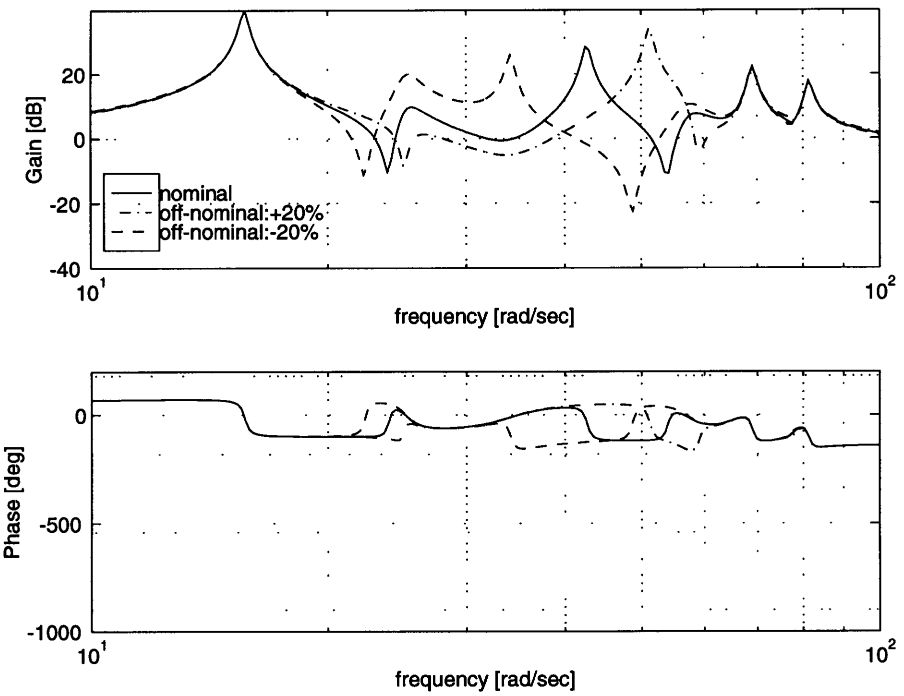

Figure 2-26: Bode plots of the loop transfer functions of the high authority MM compensator and the plant systems disturbed in the second mode frequency

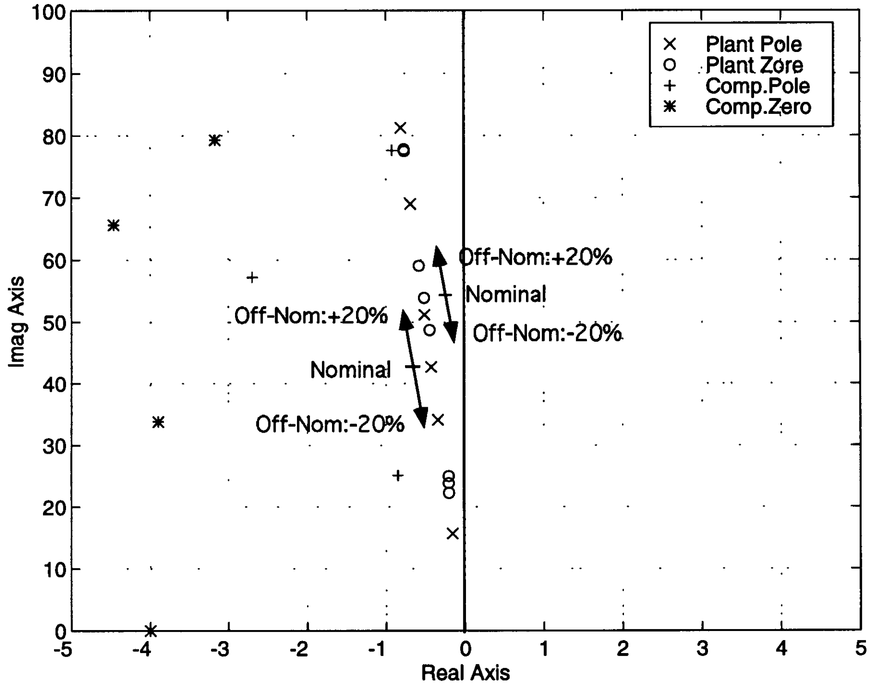

Figure 2-27: Pole-zero location of the high authority MM compensator and the plant systems disturbed in the second mode frequency

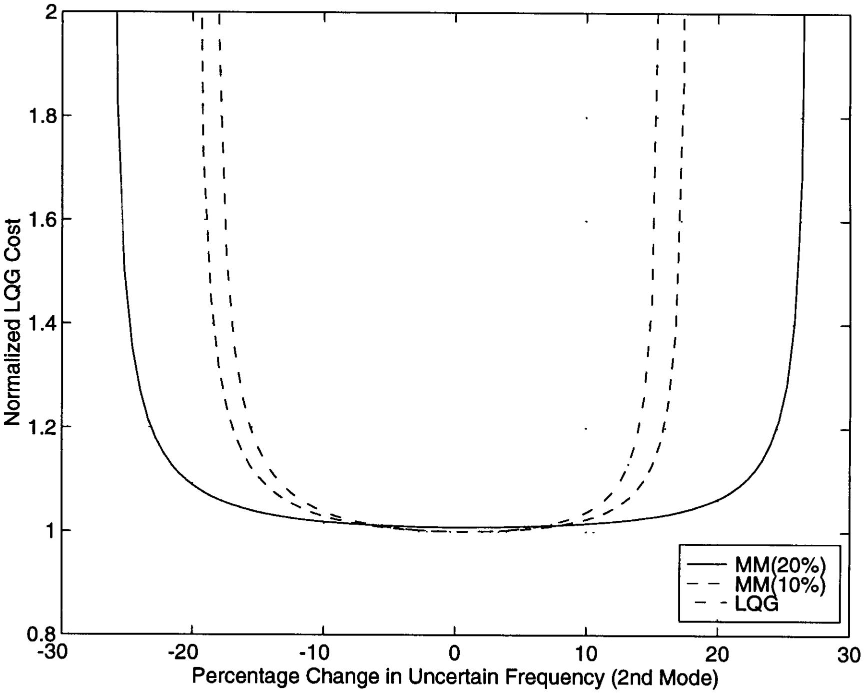

Figure 2-28: LQG costs of the closed loop systems with the low authority MM compensator

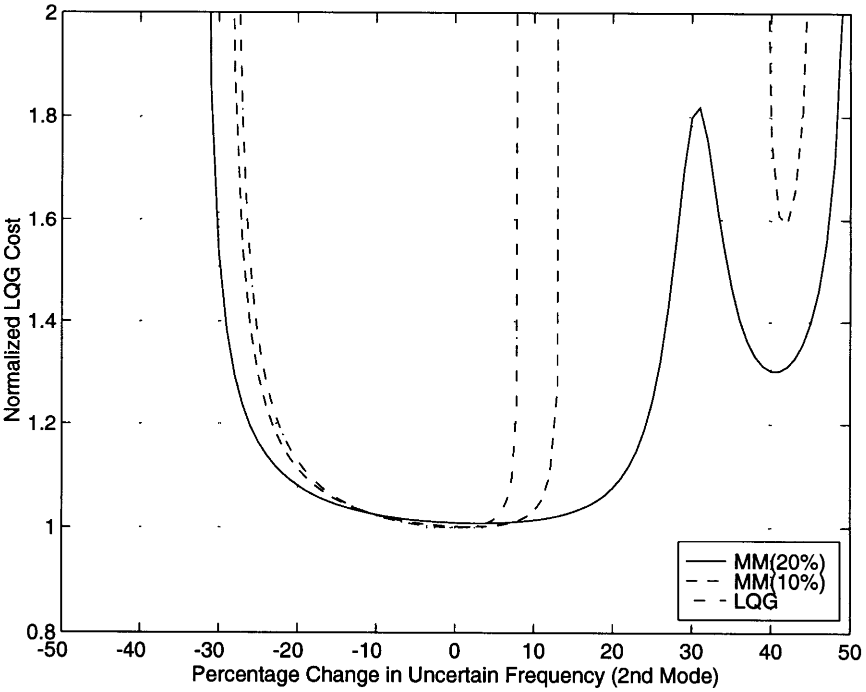

Figure 2-29: LQG costs of the closed loop systems with the high authority MM compensator

2.4 Conclusions

The MM solution, which stabilizes the sample plant system with frequency uncertainty in the second Z-bending mode, is obtained successfully. The results in the LQG designs and MM designs lead to the following conclusions:

- The MM design improves the original LQG compensator by moving compensator poles and zeros located near the plant poles and zeros which have off-nominal factors in order to give a separation between them in the direction of the real and/or imaginary axes;
- The most outstanding property of the MM design is to provide robust stability and performance for compensators without large increases in control authority or loss of nominal performance. In particular, the MM design is an effective robust control design method for a plant with parametric uncertainties.

Therefore, the designs, performed in this section, conclude that the MM method is an effective robust control design technique for space structure systems with frequency uncertainty.

Chapter 3

SISO Control Designs for the 4-Mode Flexible MACE Model

The MACE test article has a gimbal at each end of the connected flexible struts. The gimbals simulate articulating sensor heads or antennas on real orbital space systems. Those gimbal systems provide pointing and tracking. In both modes, motion of the instruments can cause the dynamics of the plant to change in a nonlinear fashion due to such effects as centrifugal force and geometrically nonlinear frequency shifts.

If the sensor heads or antennas swing at slow rates, the effect of centrifugal forces can be neglected and the LQG compensators with linear estimators yield reasonably good results [38]. However, if the equipment moves through large angles from the nominal position, the inertia properties of the plant system can change in nonlinear ways and the natural frequencies of the structural modes can deviate from the nominal case. This nonlinear change of the plant dynamics can destabilize the closed loop systems which consist of linear estimators.

It is important to study the capability of a robust, time-invariant linear compensator to stabilize off-nominal plants. In this chapter, the Multiple Model (MM) method is applied to examine its capability to stabilize an off-nominal system with nonlinear inertia property changes.

The main objective of the control design for the 4-mode flexible MACE model is to design compensators which stabilize the SISO plant system with the following two off-nominal factors:

- ±10% frequency uncertainties in the second Z-axis bending mode;
- $\pm 45 deg$ primary gimbal average angles.

At first, LQG compensators are designed to examine their capability for the nonlinear inertia properties. The MM design follows the LQG design to obtain the compensator which has the targeted robustness for both off-nominal factors. The LQG compensators are used as an initial matrix set for the MM design.

3.1 SISO Plant System

The SISO, 4-mode flexible MACE model needs to be developed before starting control designs. The primary gimbal average angel, which causes nonlinear inertia property changes, is considered in the model. This section presents the modeling procedure of the SISO model and the examination of the nonlinear inertia property effects of the SISO model caused by changes of the primary gimbal average angle.

3.1.1 Modeling

Modeling the 4-mode flexible MACE model starts with replacing the two end nodes of the 4-mode free-free flexible beam model developed in Section 2.3.1 with two gimbals and two smaller end nodes. The two gimbals are called the primary gimbal and the secondary gimbal.

The gimbals are modeled with a simple pendulum, which consists of a rigid beam and a point mass as illustrated in Figure 3-1, and is regarded as a rigid body. The point mass is rigidly joined to one of the ends of the rigid beam. The other end of the rigid beam is connected to the end node of the main structure of the MACE test article. The gimbals can rotate around the connection point in Z axis freely. The control torque acts on the gimbal at the connection point and reacts on the main

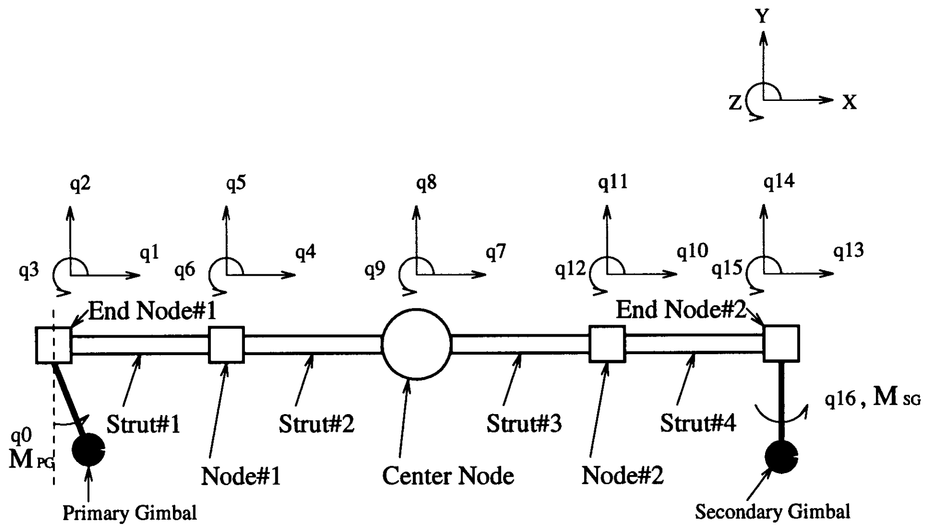

Figure 3-1: 4-mode flexible MACE model

structure. Because of the control torque and friction force at the connection points, the gimbal rotational mode has mode frequency, $0.2Hz$, and damping ratio, 0.4 [32].

The modeling of the primary gimbal dynamics begins with the total kinetic energy of the primary gimbal, T_{PG},

$$2T_{PG} = m_{PG}\left\{\dot{q}_1^2 + \dot{q}_2^2 + 2l_{PG}(\dot{q}_1 \cos q_0 + \dot{q}_2 \sin q_0)\dot{q}_0\right\} + (I_{zPG} + m_{PG}l_{PG}^2)\dot{q}_0^2 \tag{3.1}$$

Since the potential energy of the primary gimbal on orbit can be neglected, the Lagrangian of this dynamic system consists of only the kinetic energy above. Thus, the equations of motion of the primary gimbal are derived by using Lagrange's equations as follows:

$$(I_{zPG} + m_{PG}l_{PG}^2)\ddot{q}_0 + m_{PG}l_{PG}(\ddot{q}_1 \cos q_0 + \ddot{q}_2 \sin q_0) = M_{PG} \tag{3.2}$$

$$m_{PG}\left\{\ddot{q}_1 + l_{PG}(\ddot{q}_0 \cos q_0 - \dot{q}_0^2 \sin q_0)\right\} = 0 \tag{3.3}$$

$$m_{PG}\left\{\ddot{q}_2 + l_{PG}(\ddot{q}_0 \sin q_0 + \dot{q}_0^2 \cos q_0)\right\} = 0 \tag{3.4}$$

The translational equations have centrifugal force term generated by the rotational motion of the gimbal. With assumption that rotation rates of the gimbal are slow,

Table 3.1: Additional physical values of the 4-mode flexible MACE model

item	symbol	values
Gimbals : Mass	$m_{PG/SG}$	$2.320\,kg$
Moment of Inertia (Z-axis)	$I_{zPG/SG}$	$3.73 \times 10^{-2}\,kg\,m^2$
Moment of arm	$l_{PG/SG}$	$9.87 \times 10^{-2}\,m$
End Nodes : Mass	M_{Ej} $(j = 1, 2)$	$4.742\,kg$
Moment of Inertia (Z-axis)	I_{zEj} $(j = 1, 2)$	$6.412 \times 10^{-2} kg\,m^2$

the centrifugal force term can be negligible. Therefore, the equations of motion are linearized as

$$\begin{bmatrix} I_{zPG} + m_{PG}l_{PG}^2 & m_{PG}l_{PG}\cos q_0 & m_{PG}l_{PG}\sin q_0 \\ m_{PG}l_{PG}\cos q_0 & m_{PG} & 0 \\ m_{PG}l_{PG}\sin q_0 & 0 & m_{PG} \end{bmatrix} \begin{bmatrix} \ddot{q}_0 \\ \ddot{q}_1 \\ \ddot{q}_2 \end{bmatrix} = \begin{bmatrix} M_{PG} \\ 0 \\ 0 \end{bmatrix} \tag{3.5}$$

In the same way, the linearized equations of motion of the secondary gimbal are derived as follows:

$$\begin{bmatrix} m_{SG} & 0 & m_{SG}l_{SG}\cos q_{16} \\ 0 & m_{SG} & m_{SG}l_{SG}\sin q_{16} \\ m_{SG}l_{SG}\cos q_{16} & m_{SG}l_{SG}\sin q_{16} & I_{zSG} + m_{SG}l_{SG}^2 \end{bmatrix} \begin{bmatrix} \ddot{q}_{13} \\ \ddot{q}_{14} \\ \ddot{q}_{16} \end{bmatrix} = \begin{bmatrix} 0 \\ 0 \\ M_{SG} \end{bmatrix} \tag{3.6}$$

Hence, the mass matrices of the gimbals for the equations of motion of the flexible structure, Equation (2.38), are given by

$$[\overline{m}_{PG}] = \begin{bmatrix} I_{zPG} + m_{PG}l_{PG}^2 & m_{PG}l_{PG}\cos q_0 & m_{PG}l_{PG}\sin q_0 \\ m_{PG}l_{PG}\cos q_0 & m_{PG} & 0 \\ m_{PG}l_{PG}\sin q_0 & 0 & m_{PG} \end{bmatrix} \tag{3.7}$$

$$[\overline{m}_{SG}] = \begin{bmatrix} m_{SG} & 0 & m_{SG}l_{SG}\cos q_{16} \\ 0 & m_{SG} & m_{SG}l_{SG}\sin q_{16} \\ m_{SG}l_{SG}\cos q_{16} & m_{SG}l_{SG}\sin q_{16} & I_{zSG} + m_{SG}l_{SG}^2 \end{bmatrix} \tag{3.8}$$

Table 3.2: Nominal bending modes of the 4-mode flexible MACE model

Description	Nominal Frequency [Hz]	Nominal Damping Ratio
1st Z-bending mode	2.59	0.01
2nd Z-bending mode	7.42	0.01
3rd Z-bending mode	13.02	0.01
4th Z-bending mode	14.47	0.01

And the stiffness matrices are given by

$$\left[\bar{k}_{PG}\right] = \begin{bmatrix} k_{PG} & 0 & 0 \\ 0 & 0 & 0 \\ 0 & 0 & 0 \end{bmatrix} \tag{3.9}$$

$$\left[\bar{k}_{SG}\right] = \begin{bmatrix} 0 & 0 & 0 \\ 0 & 0 & 0 \\ 0 & 0 & k_{SG} \end{bmatrix} \tag{3.10}$$

The 4-mode flexible MACE model is given by following the same procedure for the 4-mode free-free flexible beam model described in Section 2.3.1 and setting the damping ratios of the Z-bending modes to 0.01. The additional physical values in this modification are listed in Table 3.1. The rest of the values are the same as shown in Table 2.1.

When the gimbals are in their nominal positions, $q_0 = 0$ and $q_{16} = 0$, the natural frequencies of the Z-bending modes are given as shown in Table 3.2. The natural frequencies of the first three modes reasonably correspond to those of the first three Z-bending modes in the 0-g FEM model of the MACE test article shown in Table 2.3 [32].

The configuration of the plant system for the SISO control designs is summarized in Table 3.3. The disturbance input and performance output are collocated at the control input and sensor output, respectively.

Table 3.3: Configuration of the SISO plant system of the 4-mode flexible MACE model

item	contents
Order of the system	10 (4 Z-bending modes & primary gimbal rotational mode)
Control input	Primary gimbal torque about Z axis at the end node #1
Sensor output	Relative angle, $q_0 - q_3$, about Z axis at the end node #1 (Encoder output)
Disturbance input	Disturbance torque about Z axis at the end node #1 (collocated at the same position of the control input)
Performance output	Relative angle, $q_0 - q_3$, about Z axis at the end node #1 (collocated at the same position of the sensor output)

3.1.2 Nonlinear Inertia Property Effects

Sluing the gimbals changes the geometric shape of the structure and causes nonlinear change of the vibrational modes from their nominal values. The plant system is no longer a linear, time-invariant system. The system matrices of the plant are functions of the gimbal angles. They are also functions of time implicitly, because the gimbal angles change with time.

$$\begin{aligned} \dot{\tilde{x}} &= \tilde{A}(q_0, q_{16}, t)\tilde{x} + \tilde{B}(q_0, q_{16}, t)w \\ z &= \tilde{C}(q_0, q_{16}, t)\tilde{x} + \tilde{D}(q_0, q_{16}, t)w \end{aligned} \tag{3.11}$$

Table 3.4 shows the pole-zero frequencies of the plant system with the primary gimbal angles of $\pm 45deg$. The second gimbal angle is set to $0deg$. The table indicates the following notable features:

- The frequency changes of the plant poles are small, because the moment arm of the primary gimbal is short, $9.87 \times 10^{-2}\ m$, while the mass of the primary gimbal is about 7% of the total mass of the MACE test article. The maximum change of the pole frequency is about 1% in the first mode. For high authority compensators, however, this magnitude of the pole frequency changes can be a serious problem.

- The frequency changes of the plant zeros are larger than those of the plant poles. From the sample designs, these zero frequency changes can destabilize the closed loop system with linear, time-invariant compensators. The reason of the destabilization is that the state variables are estimated with a linear estimator in compensators while the actual states change nonlinearly.

The Bode plots and pole-zero location of the SISO plant system with ±10% frequency uncertainty changes in the second Z-bending mode are illustrated in Figures 3-2 and 3-3, respectively. The influence of the second mode frequency uncertainty is limited to the second and third zeros. On the other hand, Figures 3-4 and 3-5 show the Bode plots and pole-zero location of the SISO plant systems with $\pm 45deg$ primary gimbal

Table 3.4: Plant pole-zero frequencies with the primary gimbal angle changes

Description [unit : Hz]	PG Angle = -45deg		PG Angle = 0deg (Nominal)	PG Angle = +45deg	
Pole : 1st	2.611	1.23%	2.592	2.611	0.73%
2nd	7.423	0.06%	7.419	7.422	0.04%
3rd	13.030	0.09%	13.018	13.026	0.06%
Zero : 1st	2.449	−2.51%	2.512	2.590	3.11%
2nd	6.899	0.50%	6.865	6.893	0.41%
3rd	11.560	3.96%	11.120	10.837	−2.54%
4th	14.060	0.38%	14.007	13.980	−0.19%

angle changes. The large movements of the first and third plant zeros are clearly observed, while the other zeros and all poles are hardly affected.

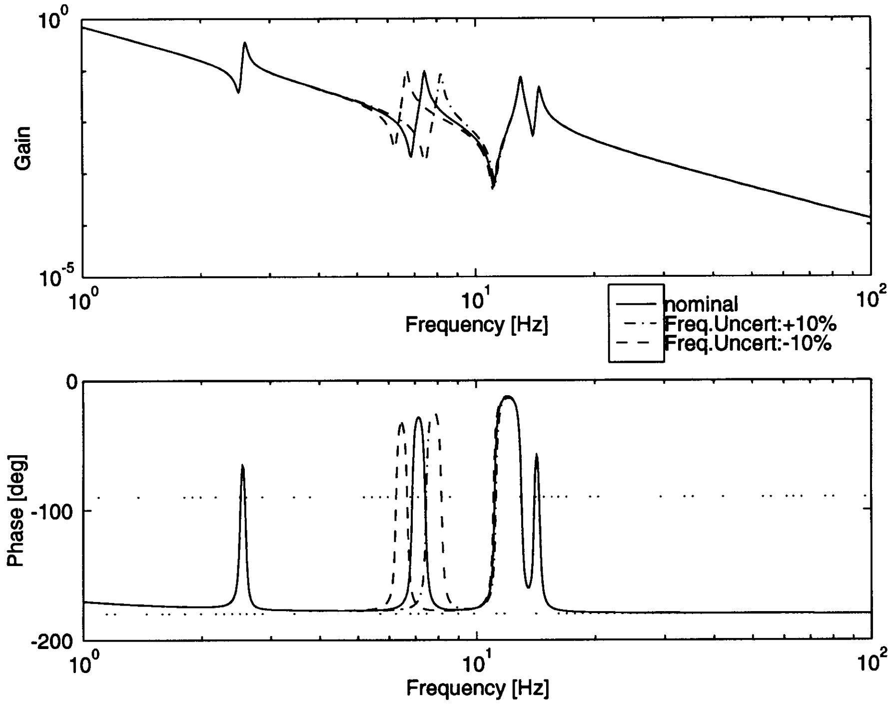

Figure 3-2: Bode plot of the 4-mode flexible MACE model with the frequency uncertainty changes in the second Z-bending mode

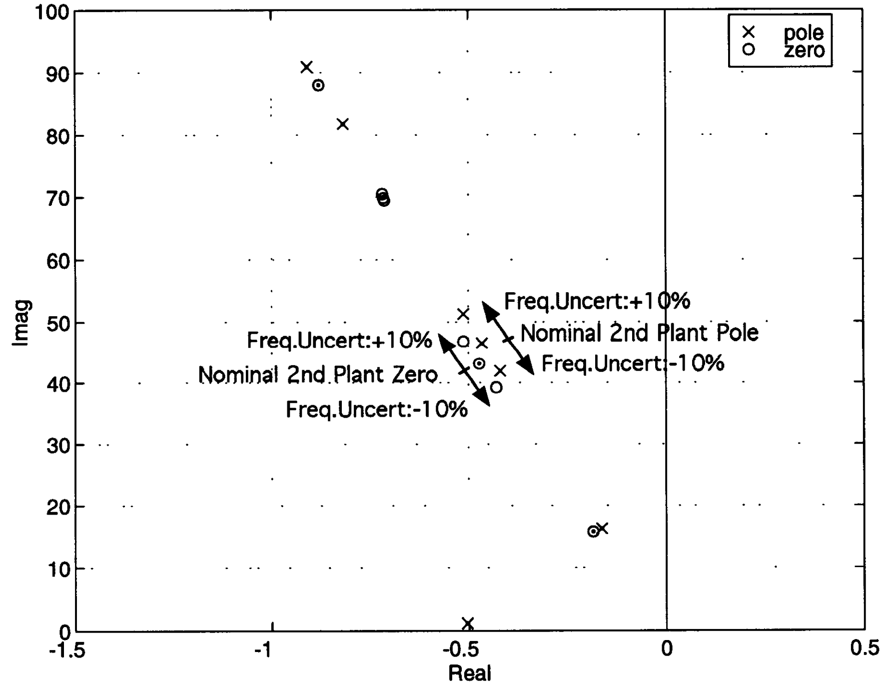

Figure 3-3: Pole-zero location of the 4-mode flexible MACE model with the frequency uncertainty changes in the second Z-bending mode

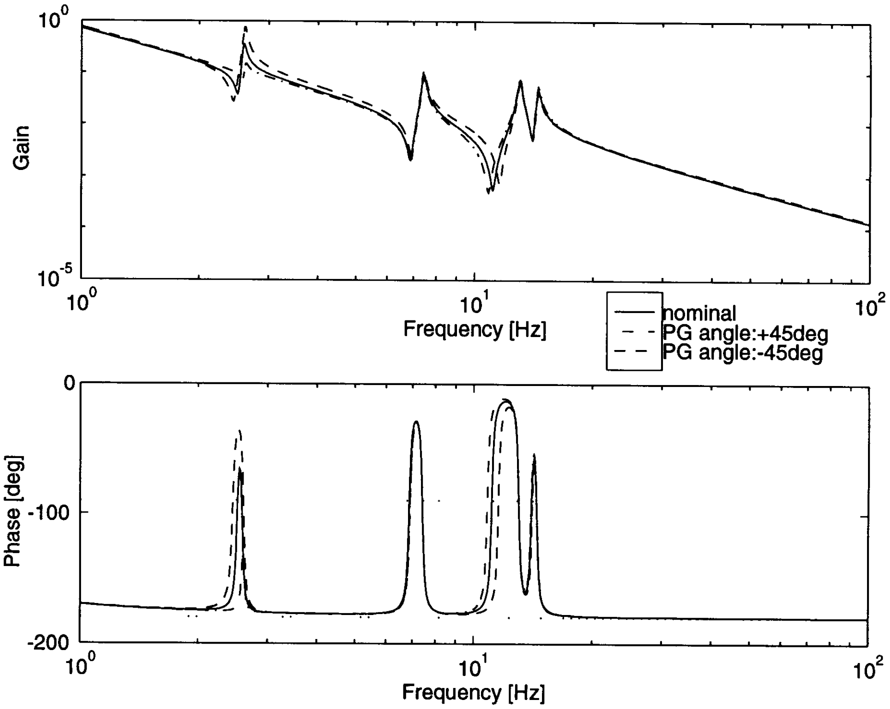

Figure 3-4: Bode plot of the 4-mode flexible MACE model with the primary gimbal angle changes

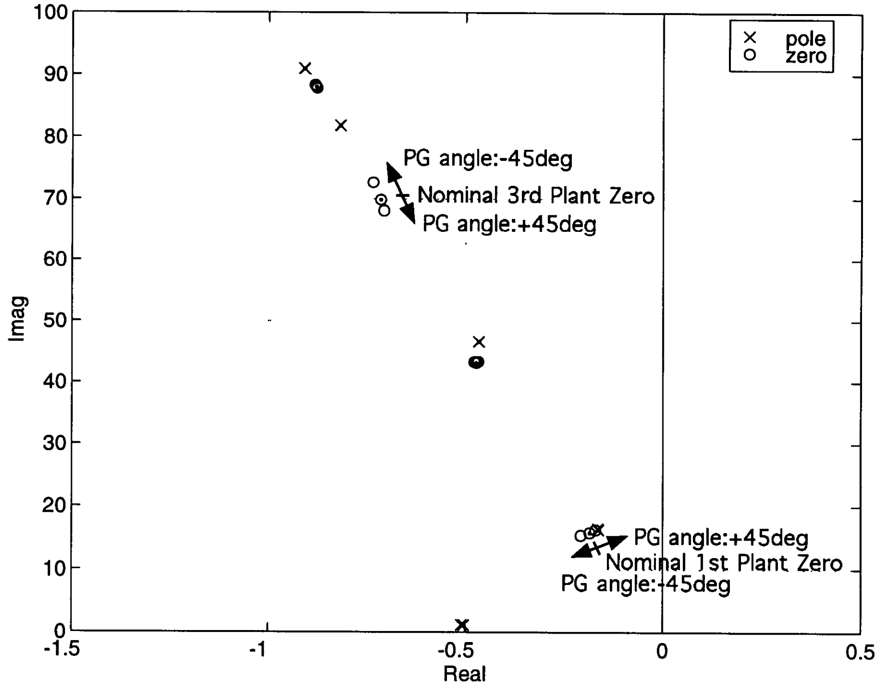

Figure 3-5: Pole-zero location of the 4-mode flexible MACE model with the primary gimbal angle changes

3.2 LQG Designs

Three LQG compensators with low, middle, and high control authority are designed and examined with respect to robustness for the nonlinear mass property. Each of the resulting LQG compensators is used as an initial matrix set for the MM design.

The balanced condition discussed in Section 2.1.2, gives the control and disturbance weights as listed in Table 3.5. The LQG compensators are called low authority, middle authority, and high authority according to their control authority.

Figure 3-6 shows the pole-zero location of the LQG compensators and the nominal plant system. As the control authority gets higher, compensator zeros move in the negative direction of the real axis. The low and middle authorities have two sets of nonminimum phase zeros, while the high authority has one set of nonminimum phase zero. Compensator poles approach the plant zeros as the control authority increases.

The frequency responses of the LQG compensators are plotted with the frequency response of the plant system in Figure 3-7. While the high authority compensator has higher gain throughout the whole frequency region than the low and middle authority compensators, the pole-zero pattern discussed in the sample designs in Section 2.3 is almost identical in all LQG compensators. Sets of a compensator pole and zero are alternately placed with sets of a plant pole and zero. The gain behavior of the high authority above $100 rad/sec$ is different from that of the low and middle authorities. This results in the wider control frequency range of the high authority compensator. The crossover frequency of the high authority compensator is three times as large as

Table 3.5: Summary of the LQG designs for the SISO plant system of the 4-mode flexible MACE model

Design Case	Weights			Crossover	Performance	Nominal
Control Authority	State C_z	Control D_{zu} ρ	Sensor Noise D_{yw} θ	Frequency $[rad/sec]$	Gain $[dB]$	LQG Cost
Low	1.0	1.0×10^{-2}	1.0×10^{-2}	111.3	−38.884	2.110×10^{-1}
Middle	1.0	5.0×10^{-3}	5.0×10^{-3}	149.6	−43.498	1.301×10^{-1}
High	1.0	1.0×10^{-3}	1.0×10^{-3}	334.8	−53.443	4.186×10^{-2}

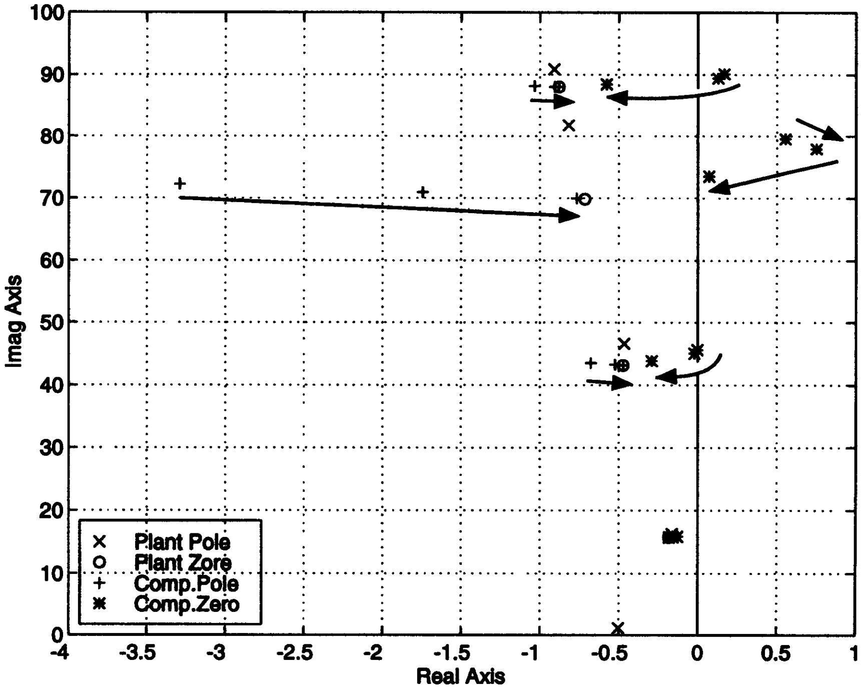

Figure 3-6: Pole-zero location of the LQG compensators and the nominal plant system

that of the low authority compensator as shown in Table 3.5.

The frequency responses of the closed loop systems from w to z plotted in Figure 3-8 imply that the higher control authority a compensator has, the better performance it has. Refer to Section 2.3.2 for the definition of the closed loop system from w to z, $|G_{cl0}(j\omega)|$. The performance gains listed in Table 3.5 also indicate the better performance of the high authority compensator for the nominal plant.

Figure 3-9 shows LQG costs of the three LQG compensators as a function of the frequency uncertainty or the primary gimbal angle. The LQG costs are normalized by the nominal LQG cost of the high authority compensator case, which is listed in Table 3.5. The outside of the "U-" or "L-" shaped plots corresponds to an unstable region. Although the high authority compensator has five times as high nominal performance as the low authority, its stability boundaries are very narrow; only $+1\%$ frequency uncertainty and $-9deg$ primary gimbal angle. On the other hand, the low authority compensator keeps robust stability for more than $\pm 60deg$ primary gimbal angle; its off-nominal LQG cost never goes up 1.2 times as high as the nominal LQG

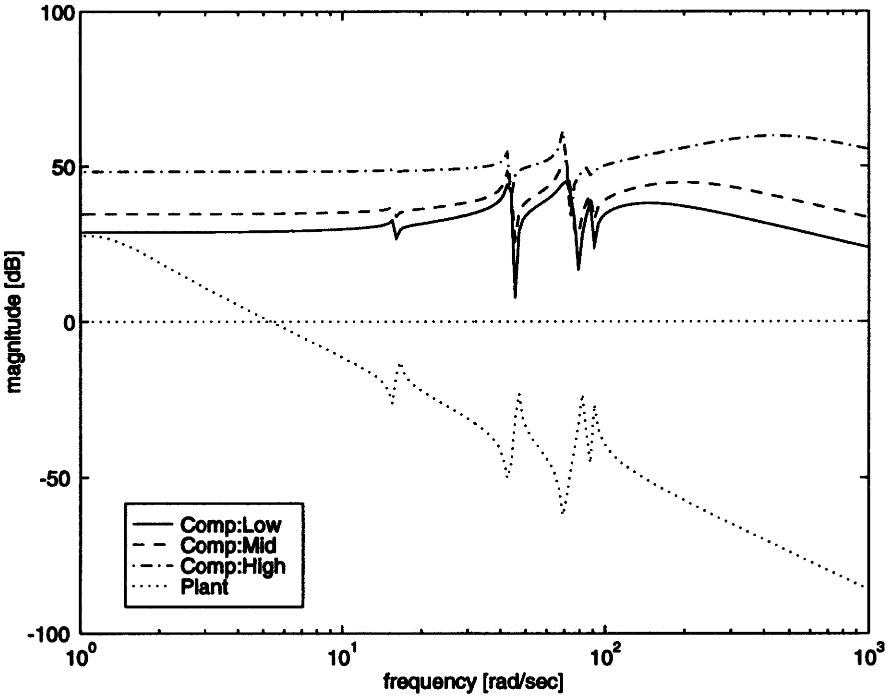

Figure 3-7: Frequency responses of the LQG compensators and the plant system

cost.

The Bode plots of the loop transfer function of the low authority compensator illustrated in Figure 3-10 predict that the closed loop system of the plant with +10% frequency uncertainty is unstable at $42 rad/sec$ and that the closed loop system of the plant with -10% frequency uncertainty is unstable at $43 rad/sec$. The destructions of the pole-zero pattern shown in Figure 3-11 bring about these destabilizations. Because the second compensator zero is located very close to the imaginary axis, every gain plot illustrated in Figure 3-10 has a deep valley at $45 rad/sec$. This results in the destabilization of the closed loop system with frequency uncertainties.

On the other hand, the Bode plots shown in Figure 3-12 indicate that the $\pm 45 deg$ primary gimbal angles do not destabilize the closed loop system. In $-45 deg$ case, the third plant zero becomes above the third compensator pole in frequency shown in Figure 3-13. Because the third compensator pole is located away from the imaginary axis, the gain of the loop transfer function keeps a negative value in dB at $67 rad/sec$ where the phase plot crosses the $-180 deg$ critical phase.

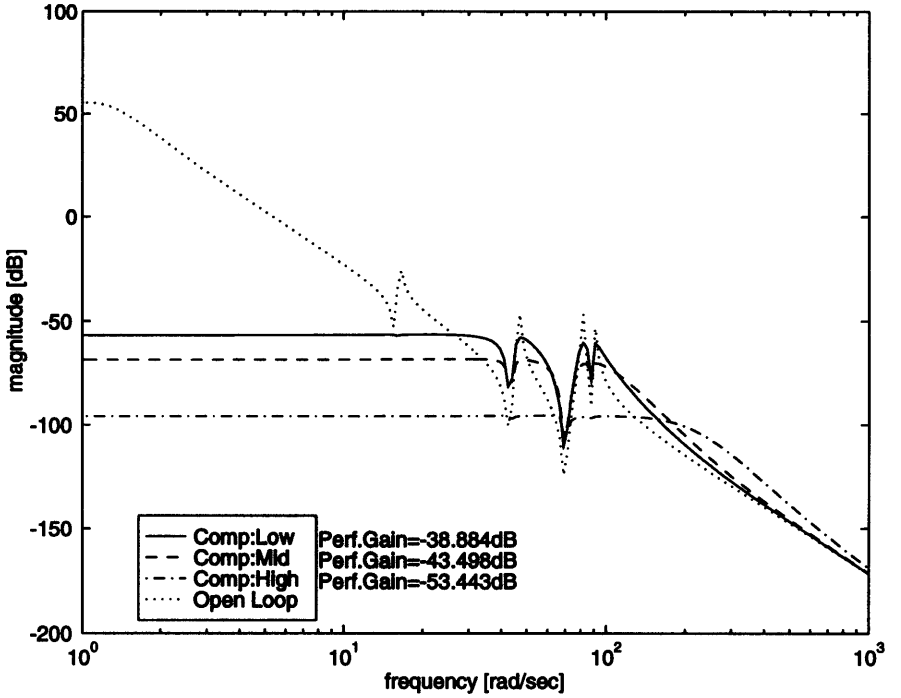

Figure 3-8: Performance of the LQG compensators

In the case of the high authority compensator, ±10% frequency uncertainties in the second Z-bending mode drastically shift the second plant zero and destroy the pole-zero pattern as illustrated in Figure 3-15. Figure 3-14 shows that these destructions of the pole-zero pattern make the phase in both cases beyond the $-180deg$ boundary around $42rad/sec$ with positive gain (in dB). In the -10% frequency uncertainty case, however, the gain keeps positive values in dB until the phase comes above $-180deg$ again. Therefore, the closed loop system with -10% frequency uncertainty is stable, while the closed loop system with $+10\%$ frequency uncertainty is unstable.

The closed loop system with $-45deg$ primary gimbal average angle is unstable from the Bode plots illustrated in Figure 3-16. As the primary gimbal turns in the negative direction, the frequency of the third plant zero increases and becomes above that of the third compensator pole. Because the poles of the high authority compensator are located very close to the plant zero as shown in Figure 3-17, small degree of the pole-zero pattern destruction easily destabilizes the closed loop system.

To examine the stability robustness of the closed loop system with the low and high authority LQG compensators, LQG costs of the closed loop system are plotted in Figure 3-18 and Figure 3-19 as a function of frequency uncertainties in the second Z-bending mode and primary gimbal angles. The LQG costs are normalized by the nominal LQG costs listed in Table 3.5. In both figures, the outside of the contours, which corresponds to the flat surfaces in the 3-dimensional view, indicates unstable region of the closed loop system.

The LQG cost plot in the case of the low authority compensator has wider flat region around the nominal point. This implies that the low authority compensator has better robustness especially for the changes of the primary gimbal angle. The closed loop system is stable from -2.5% to $+5\%$ frequency uncertainty region at nominal primary gimbal angle, $0deg$.

In the case of the high authority LQG compensator, however, the unstable region is eccentric and close to the nominal point. The closed loop system withstands only $+1\%$ frequency uncertainty and $-9deg$ primary gimbal angle. The closed system is stable and fairly robust for negative frequency uncertainty and positive primary gimbal angel, but this feature is not practical.

Both LQG compensators do not satisfy the design requirements, stability guarantee for $\pm 10\%$ frequency uncertainty and $\pm 45deg$ primary gimbal average angle. To meet the requirements, the compensators need to be modified by using robust control design techniques.

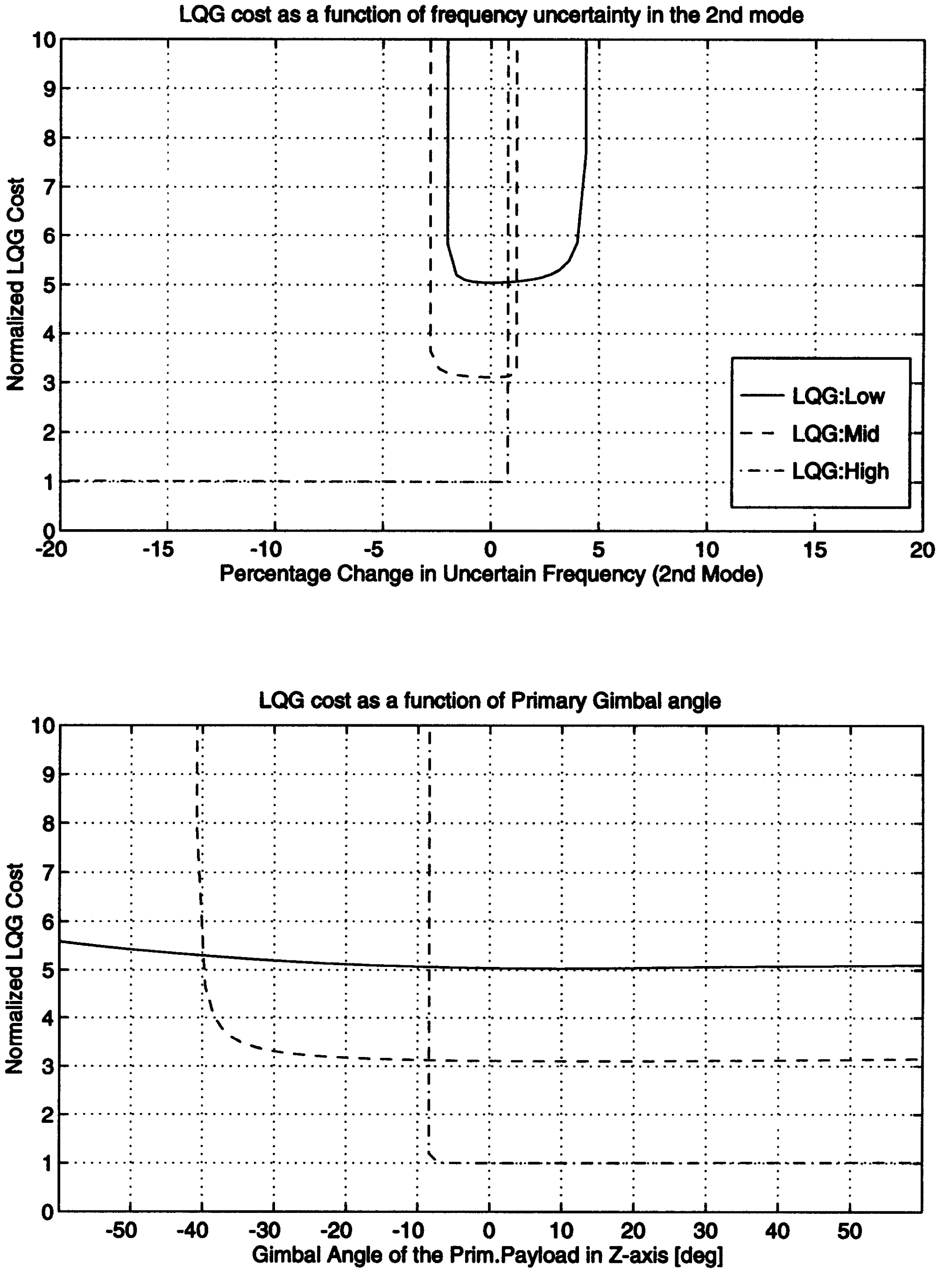

Figure 3-9: Comparison of LQG costs of the LQG compensators

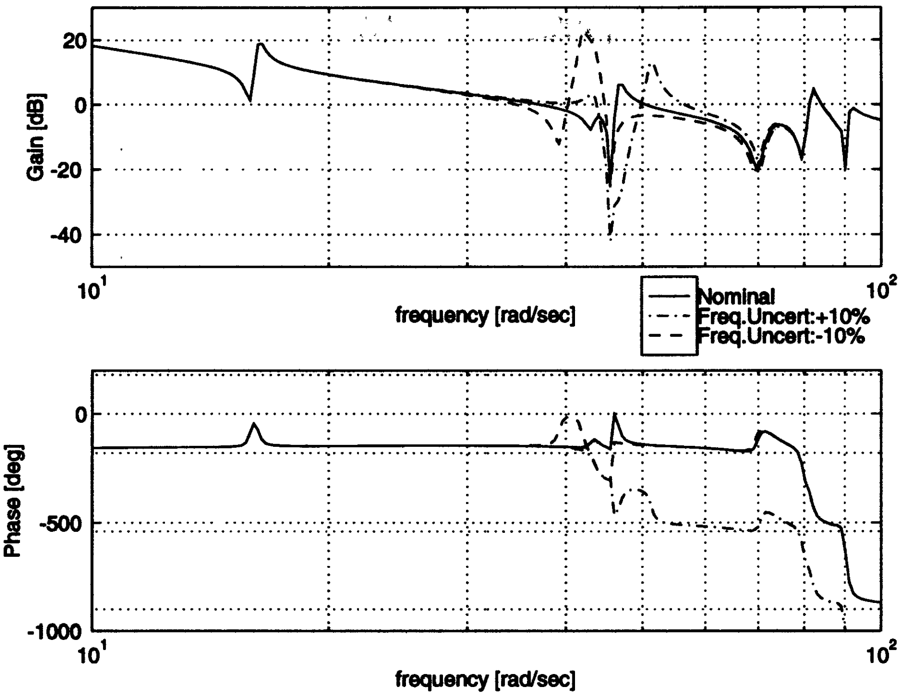

Figure 3-10: Bode plots of the loop transfer functions of the low authority LQG compensator and the plant system disturbed in the second mode frequency

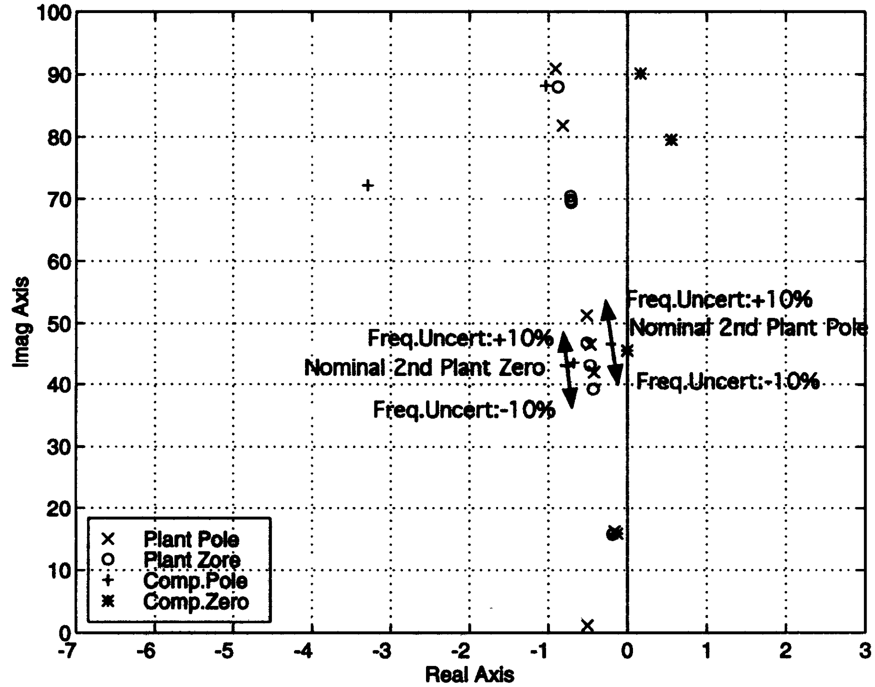

Figure 3-11: Pole-zero location of the low authority LQG compensator and the plant system disturbed in the second mode frequency

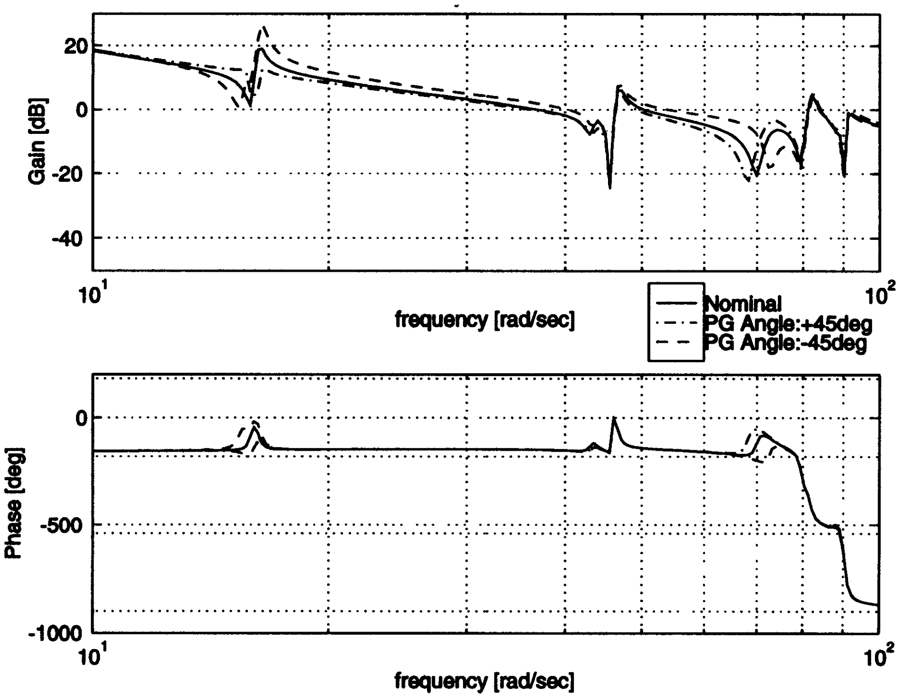

Figure 3-12: Bode plots of the loop transfer functions of the low authority LQG compensator and the plant system disturbed by the primary gimbal average angle

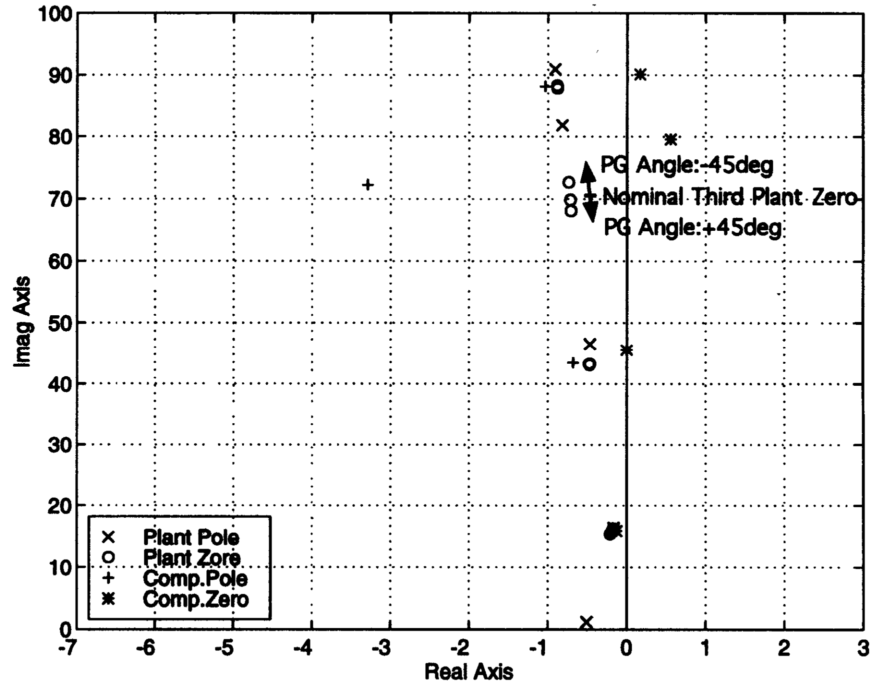

Figure 3-13: Pole-zero location of the low authority LQG compensator and the plant system disturbed by the primary gimbal average angle

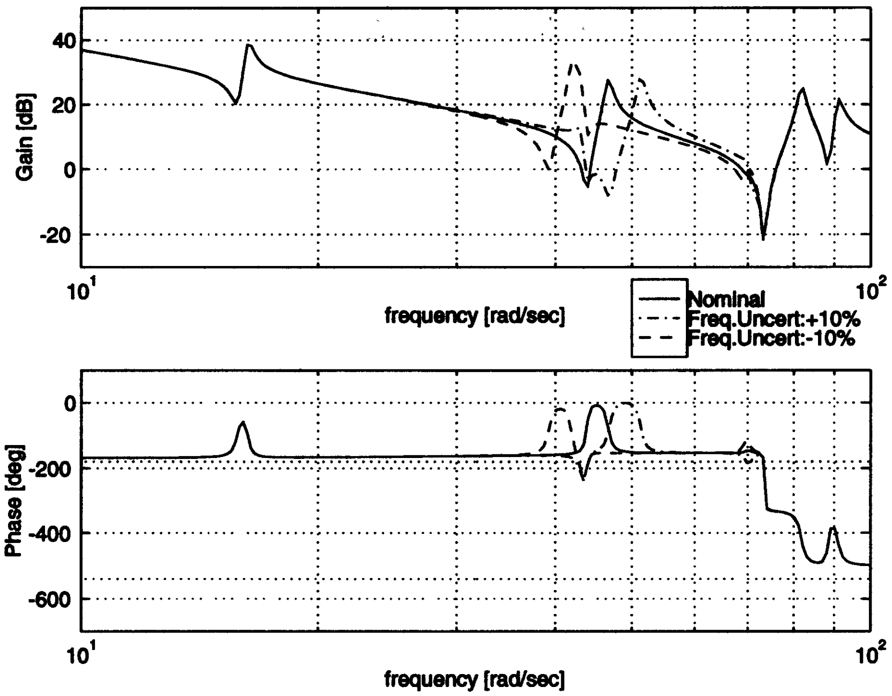

Figure 3-14: Bode plots of the loop transfer functions of the high authority LQG compensator and the plant system disturbed in the second mode frequency

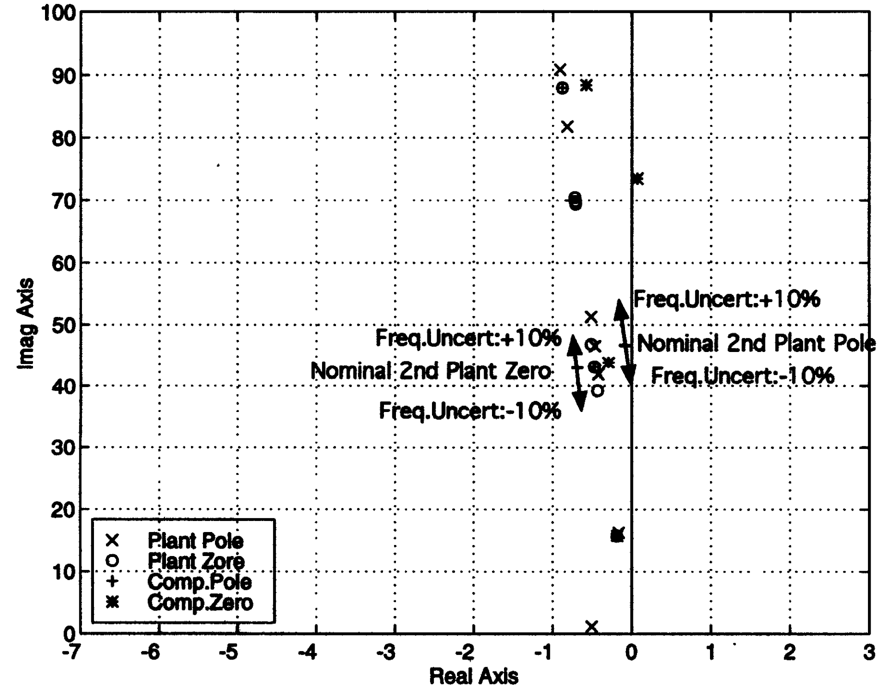

Figure 3-15: Pole-zero location of the high authority LQG compensator and the plant system disturbed in the second mode frequency

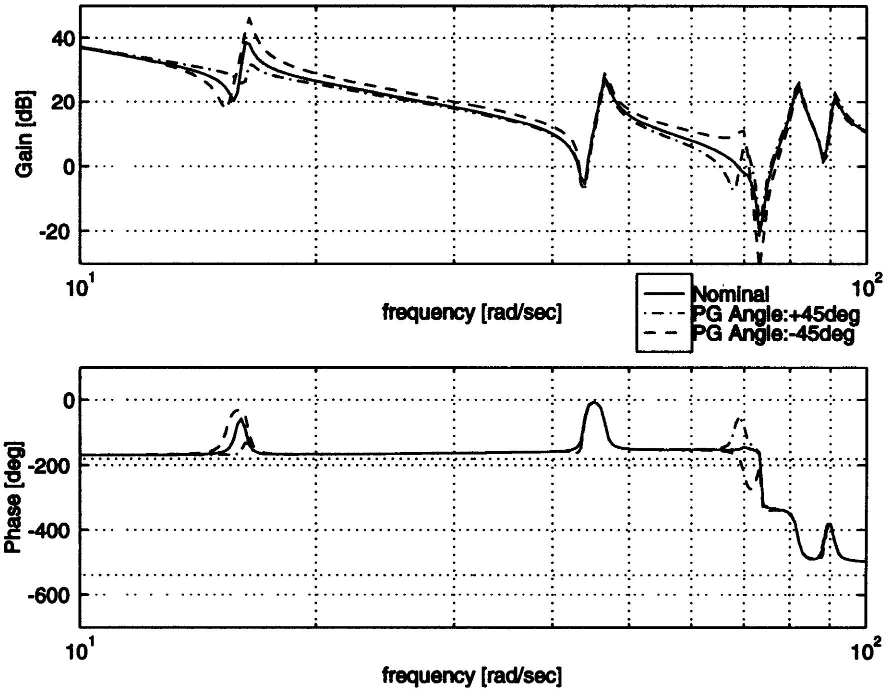

Figure 3-16: Bode plots of the loop transfer functions of the high authority LQG compensator and the plant system disturbed by the primary gimbal average angle

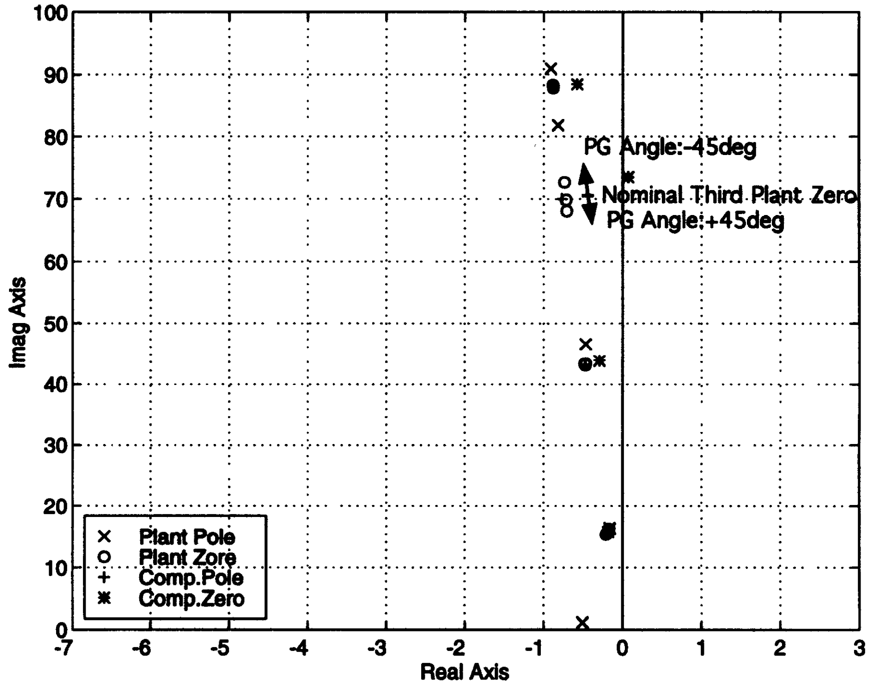

Figure 3-17: Pole-zero location of the high authority LQG compensator and the plant system disturbed by the primary gimbal average angle

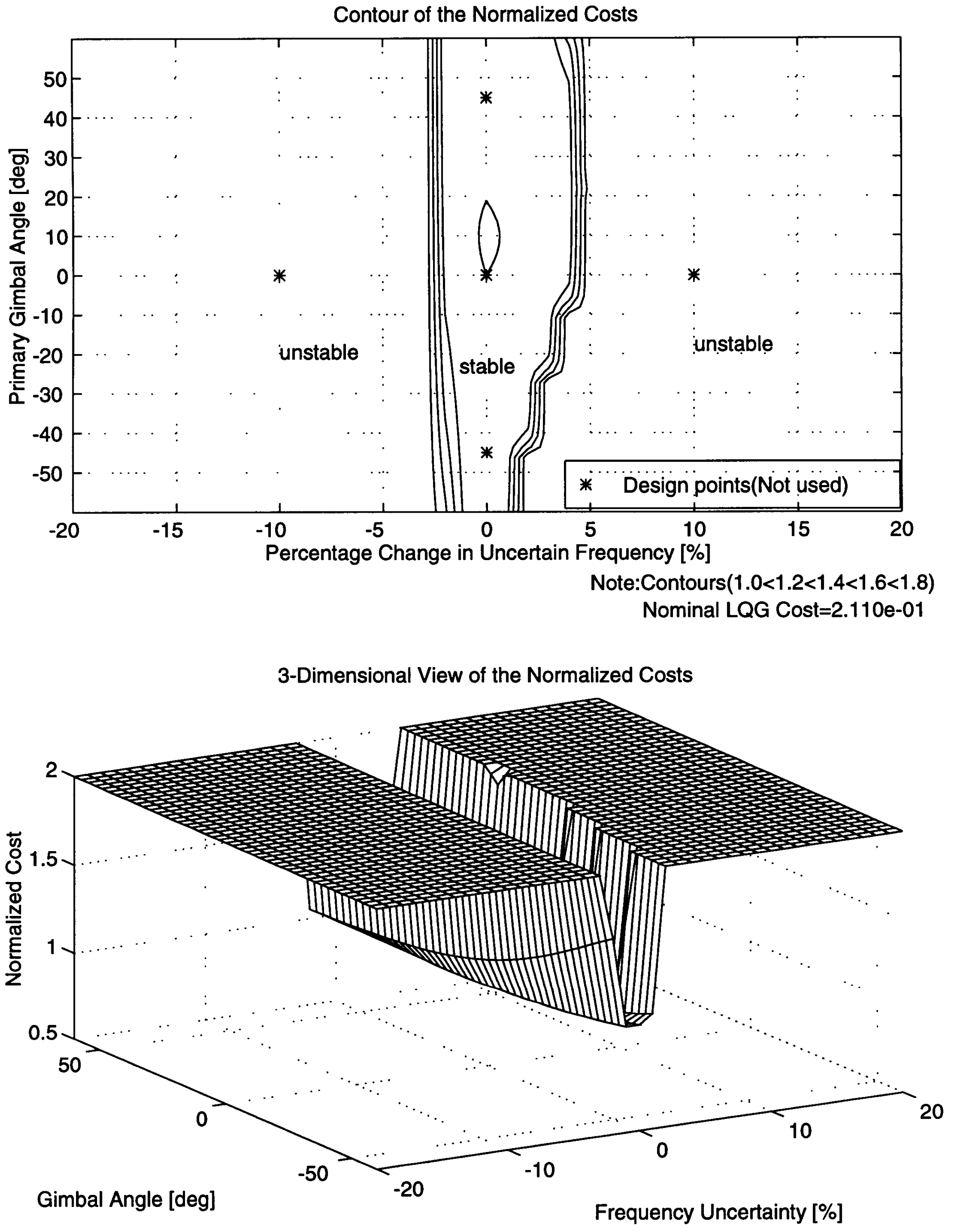

Figure 3-18: LQG cost of the closed loop system with the low authority LQG compensator

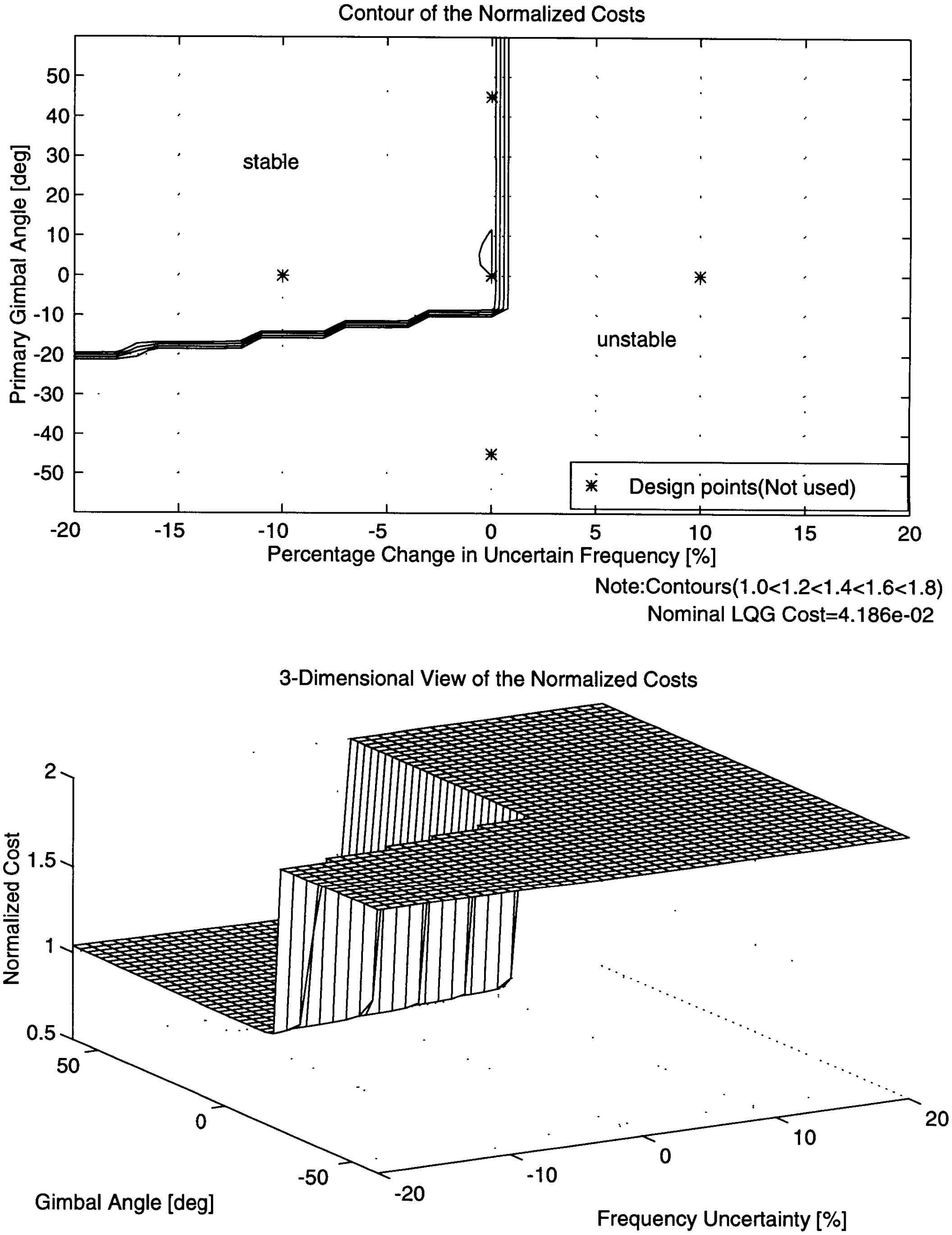

Figure 3-19: LQG cost of the closed loop system with the high authority LQG compensator

3.3 MM Designs

The LQG designs in the Section 3.2 concludes that the LQG method cannot satisfy the design requirements, stability guarantee for ±10% frequency uncertainty in the second bending mode and $\pm 45deg$ primary gimbal average angle. The Multiple Model (MM) method is applied to gain robust stability for the frequency uncertainty and the primary gimbal average angle.

The high authority LQG compensator is modified with the MM method, because it has the eccentric stable region around the nominal point and low robustness performance.

To expand the stable region of the closed loop system using the MM method, two steps need to be carried out, because there are two types of off-nominal factors: frequency uncertainty and primary gimbal average angle. In both design steps, the design strategy mentioned in Section 2.2.2, except for the initial matrix set for the second step, is followed. The resulting MM compensator in the first step is used as the initial matrix set for the second step.

In this design, the MM compensator which guarantees stability for the frequency uncertainty is designed in the first step, and then the MM compensator which guarantees stability for both off-nominal factors is designed in the second step. The former is called the FU-MM compensator and the latter the FU&PG-MM compensator for convenience.

The results of the MM designs are summarized in Table 3.6 in advance. The

Table 3.6: Summary of the MM designs for the SISO plant system of the 4-mode flexible MACE

Design Case	Weights			Crossover Frequency	Performance Gain	Nominal LQG Cost
	State C_z	Control D_{zu} ρ	Sensor Noise D_{yw} θ	$[rad/sec]$	$[dB]$	
LQG(High)	1.0	1.0×10^{-3}	1.0×10^{-3}	334.8	−53.443	4.186×10^{-2}
MM:FU	1.0	1.0×10^{-3}	1.0×10^{-3}	335.7	−53.369	4.192×10^{-2}
MM:FU&PG	1.0	1.0×10^{-3}	1.0×10^{-3}	336.2	−53.317	4.224×10^{-2}

(Note) FU:±10% Frequency Uncertainty guarantee,
PG:$\pm 45deg$ Primary Gimbal average angle guarantee.

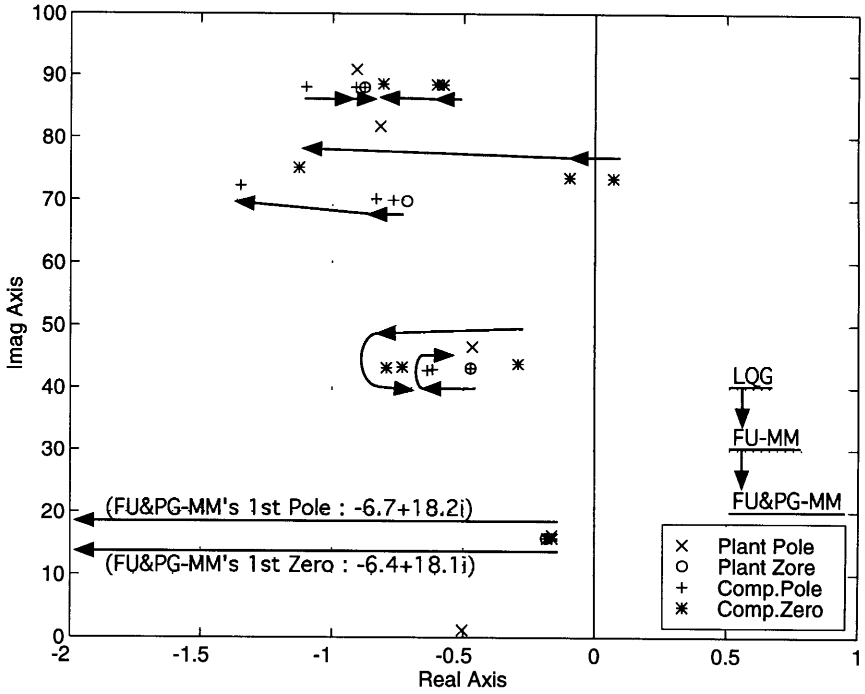

Figure 3-20: Pole-zero location of the MM compensators and the nominal plant system

crossover frequency, performance gain, and nominal LQG cost keep almost constant. This implies that the MM method provides robust stability for multiple off-nominal factors without loss of nominal performance.

Figure 3-20 shows the movement of the compensator poles and zeros. All compensator zeros move away from the plant zeros in the negative direction of the real axis. In the robustness improvement from the LQG to FU-MM, the movements of second compensator pole and zero are remarkable, because the frequency uncertainty of the plant second pole is the main off-nominal factor in this design step. This second pole-zero movement desensitizes the closed loop system to the destruction of the pole-zero pattern.

In the robustness improvement from the FU-MM to The FU&PG-MM, the first and third pole-zero locations are significantly changed. These movements relate to the movements of the first and third plant zeros which are stimulated by the second off-nominal factor, *i.e.* the primary gimbal average angle. The FU&PG-MM compensator does not have a nonminimum phase zero.

Another interesting point of the pole-zero location is the movement of the second compensator pole and zero. In the first design step, the second compensator pole moves in the negative direction of the real axis. This movement provides larger separation between the second plant zero and the second compensator pole itself. In the second design step, however, the second compensator pole moves back in the positive direction of the real axis. The second compensator zero also moves in the same way. Obviously, the two design requirements are contrary to each other with respect to the location of the second compensator pole and zero.

3.3.1 FU-MM compensator

As the first step of the MM design, the compensator which guarantees stability for the frequency uncertainty in the second bending mode is designed through expanding the stable region of the LQG compensator in the direction of the frequency uncertainty. The high authority LQG compensator designed in Section 3.2 is used as the initial matrix set.

Three design points are set in the first design step: the nominal design point and two off-nominal design points which are deviated from the nominal design point in the positive and negative directions of the frequency uncertainty. The magnitude of the deviation is gradually enlarged from 1% to 10% in the MM design process. The closed loop system with the high authority LQG compensator used as the initial matrix set is stable for ±1% frequency uncertainty. The cost weights, β_i, are set to 0.9 for the nominal design point and 0.05 for both off-nominal design points.

In Figure 3-21, the frequency response of the FU-MM compensator is plotted with that of the high authority LQG compensator. The only notable difference between the LQG compensator and FU-MM compensator is gain decrease at $43 rad/sec$, which corresponds to the frequency of the second compensator zero. This gain decrease contributes to the desensitization of the closed loop system to disturbance in that frequency range, which is observed in Figure 3-22. However, due to the slight degradation of performance below $40 rad/sec$, the performance gain of the FU-MM compensator is almost the same as that of the original LQG compensator listed in Table 3.6.

The Bode plot of the loop transfer function in Figure 3-23 implies that the FU-MM compensator has stability robustness for the ±10 frequency uncertainty in the second bending mode. The phase of the +10% case comes below $-180 deg$ at $42 rad/sec$ but recovers at $43 rad/sec$ before the gain becomes negative values in dB. Therefore, one of the design requirements is satisfied by the FU-MM compensator.

As shown in Figure 3-25, however, the Bode plot of the loop transfer function with the plant disturbed by the primary gimbal average angle indicates that the second requirement is not satisfied yet. The third plant zero deviated by the $-45deg$ primary gimbal average angle comes above the third compensator pole in the frequency direction as illustrated in Figure 3-26. This zero movement destabilizes the closed loop system at $69rad/sec$. Because of the third compensator zero, which is located near the imaginary axis at $74rad/sec$, every gain plot has a deep valley at that frequency. This zero location significantly relates to the destabilization of the closed loop system.

The LQG cost illustrated in Figure 3-27 implies that the MM method effectively expands the stability region of the compensator in the direction of the frequency uncertainty. The FU-MM compensator provides good performance within the region between the two off-nominal design points at $\pm 10\%$ frequency uncertainties. The degree of the performance degradation for $\pm 10\%$ frequency uncertainty remains less than 20%. This plot also indicates that the closed loop system becomes unstable for the off-nominal plant system with $-12deg$ primary gimbal angle.

The next design step needs to be carried out to expand the stability region of the compensator in the direction of the other off-nominal factor, *i.e.* the primary gimbal average angle.

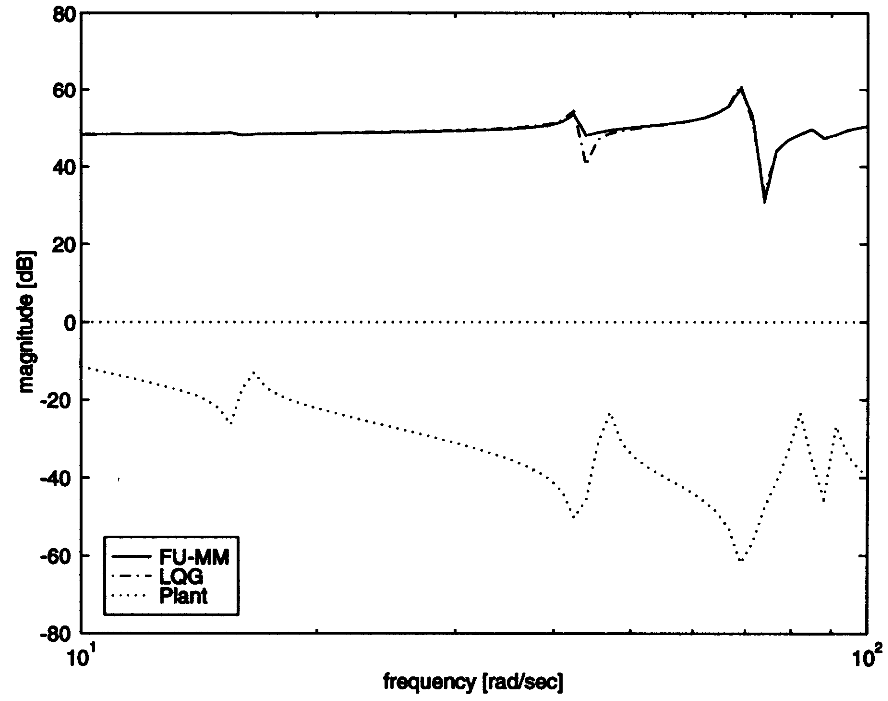

Figure 3-21: Frequency responses of the FU-MM compensator and the plant system

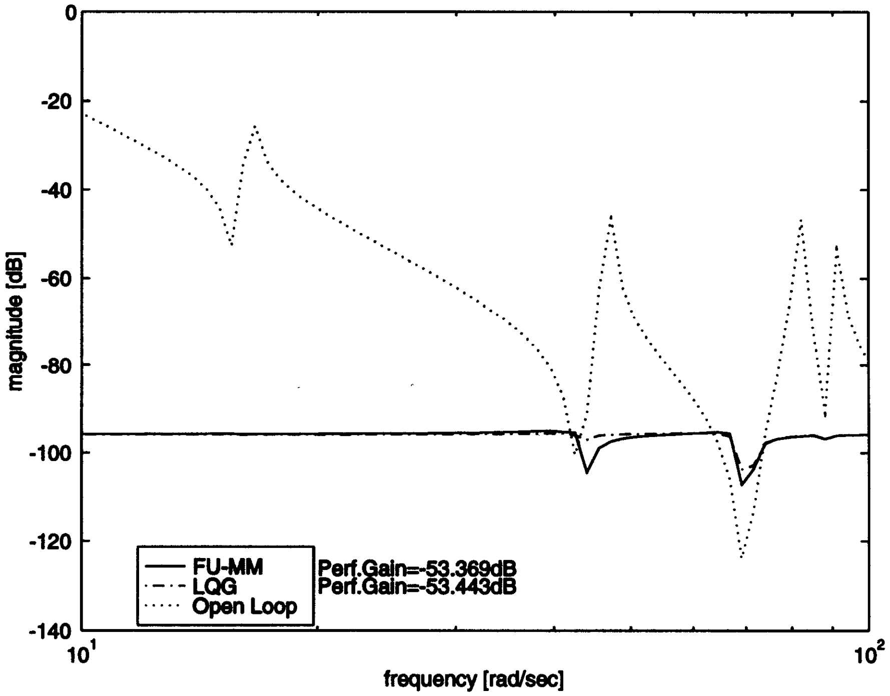

Figure 3-22: Performance of the FU-MM compensator

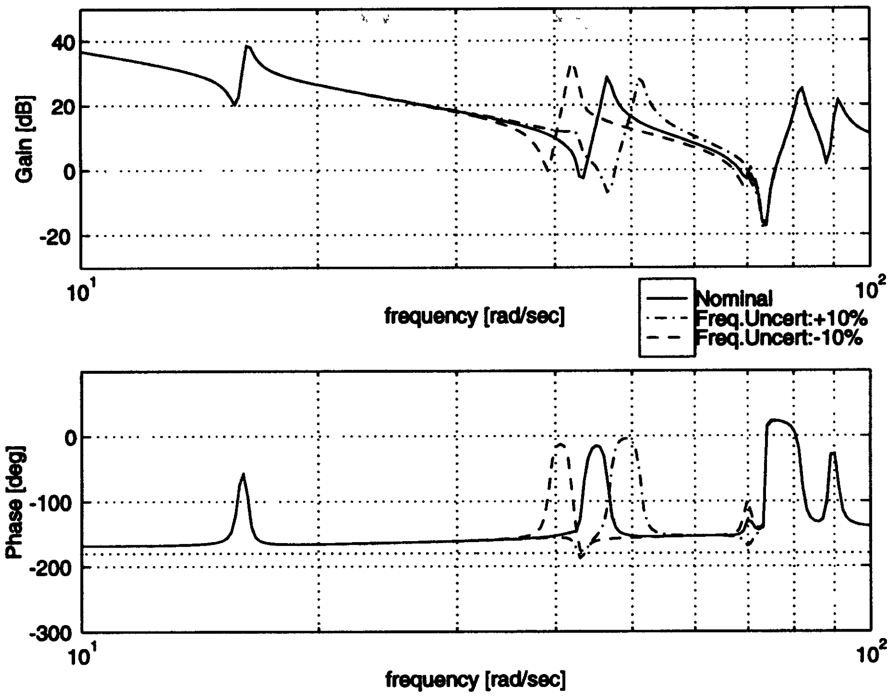

Figure 3-23: Bode plots of the loop transfer functions of the FU-MM compensator and the plant system disturbed in the second mode frequency

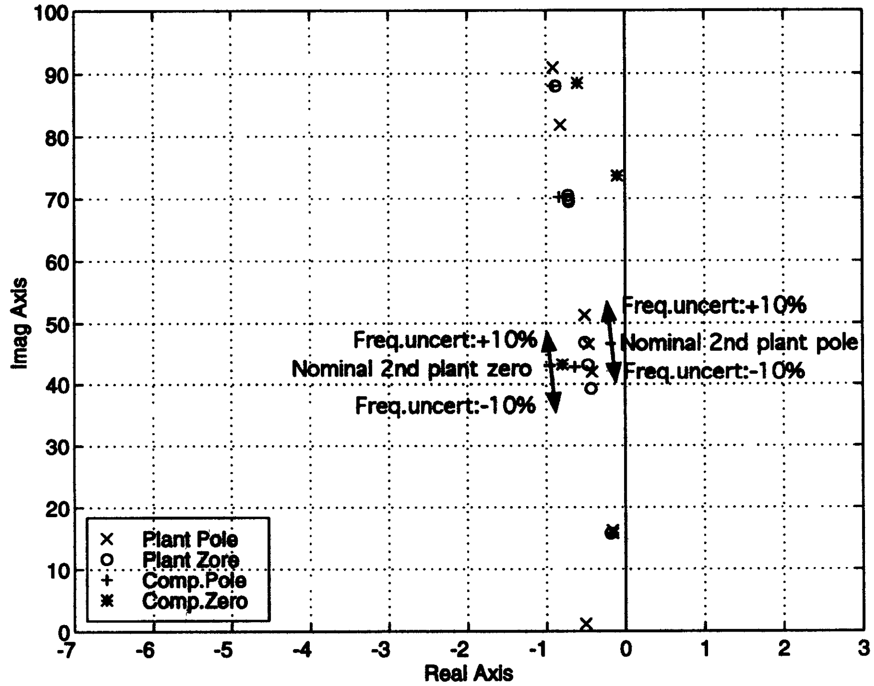

Figure 3-24: Pole-zero location of the FU-MM compensator and the plant system disturbed in the second mode frequency

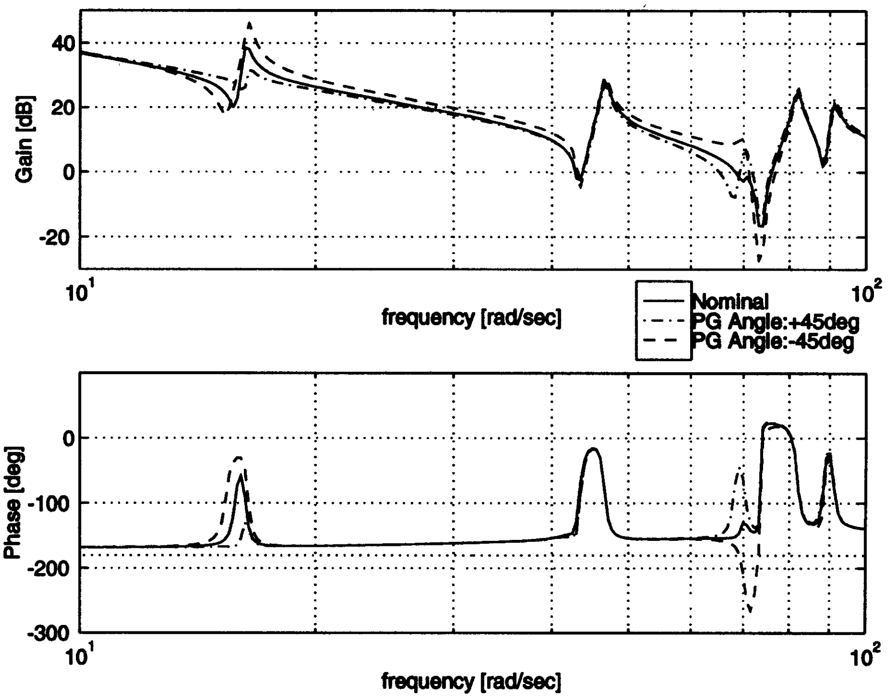

Figure 3-25: Bode plots of the loop transfer functions of the FU-MM compensator and the plant system disturbed by the primary gimbal average angle

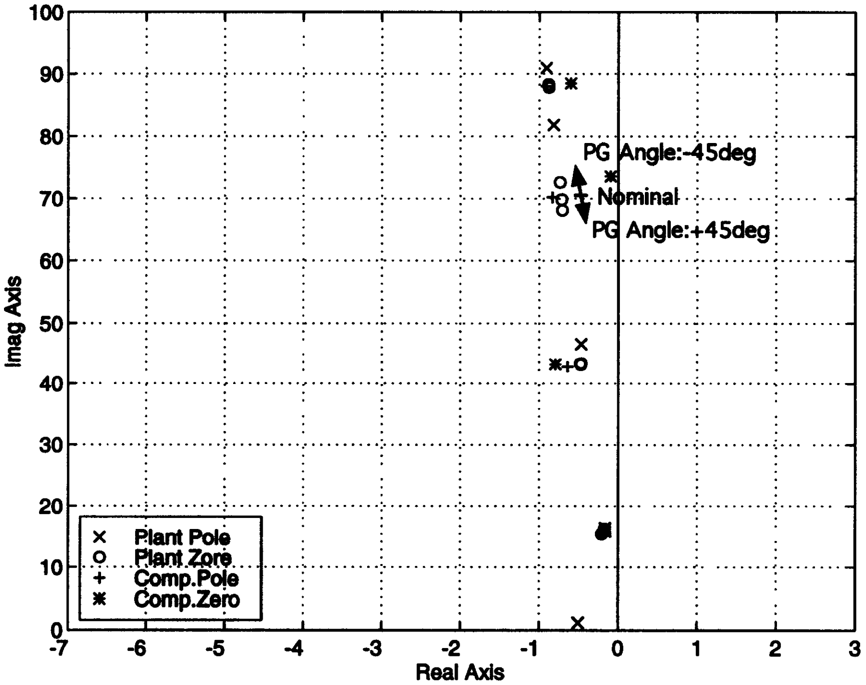

Figure 3-26: Pole-zero location of the FU-MM compensator and the plant system disturbed by the primary gimbal average angle

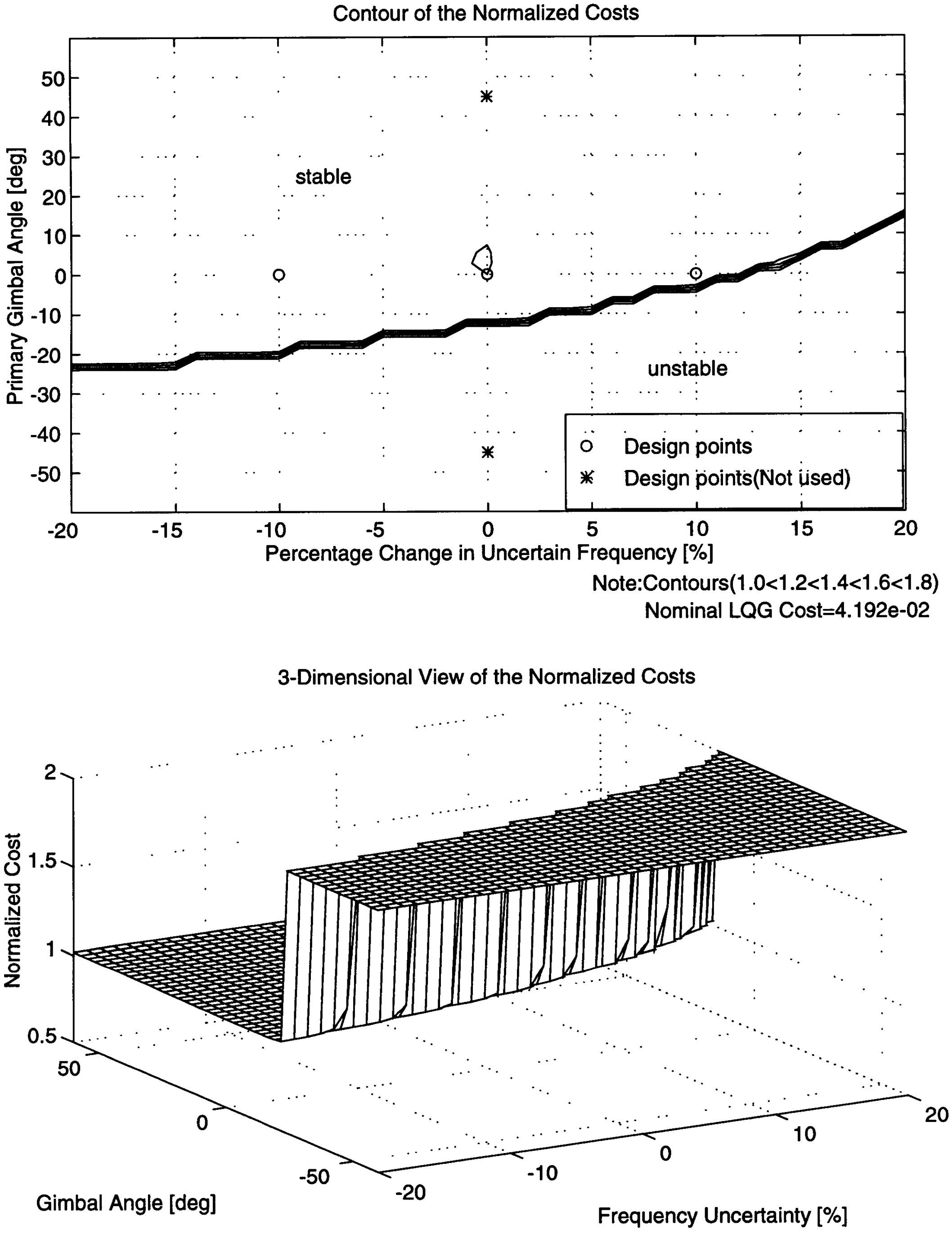

Contour of the Normalized Costs

Note:Contours(1.0<1.2<1.4<1.6<1.8)
Nominal LQG Cost=4.192e-02

3-Dimensional View of the Normalized Costs

Figure 3-27: LQG cost of the closed loop system with the FU-MM compensator

3.3.2 FU&PG-MM compensator

To satisfy the two design requirements, the robust stability of the FU-MM compensator for the primary gimbal average angle has to be improved. With the use of the MM method, the stable region is expanded in the direction of the other off-nominal factor, the primary gimbal average angle, without losing the robust stability for the frequency uncertainty.

Two more off-nominal design points need to be added in the second step of the MM design. Thus, there are five design points in total: the nominal design point, two off-nominal design points deviated in the positive and negative directions of the frequency uncertainty, and two new off-nominal design points deviated in the positive and negative directions of the primary gimbal angle. The primary gimbal angle of the off-nominal design points is gradually increased from $12deg$ to $45deg$ in the MM design process.

The FU-MM compensator designed in Section 3.3.1 is used as the initial matrix set in the second design step. Since the closed loop system with the FU-MM compensator is stable for $\pm 12deg$ primary gimbal average angle, the first set of off nominal design points is chosen at $\pm 12deg$ primary gimbal angle. The cost weights, β_i, are set to 0.3 for the nominal design point and two off nominal design points of the primary gimbal average angle, and 0.05 for the two off-nominal design points of the frequency uncertainty. Thus, an resulting compensator can be expected to have good robust performance for large primary gimbal average angle which is equivalent to the nominal performance.

The frequency response of the FU&PG-MM compensator is plotted with the frequency responses of the LQG and FU-MM compensators in Figure 3-28. The frequency increase of the second peak around $70rad/sec$ and the gain increase around $75rad/sec$ can be identified. These changes relate to the movement of the third compensator pole and zero observed in Figure 3-20 shown at the beginning of this section.

The FU&PG-MM compensator significantly desensitizes the closed loop system around $70rad/sec$ as shown in Figure 3-29. However, the performance gain of FU&PG-

MM compensator is almost the same as the performance gains of the original LQG and FU-MM compensators listed in Table 3.6, because of the further performance degradation between $30 rad/sec$ and $40 rad/sec$ and the degradation around $60 rad/sec$.

The Bode plots of the loop transfer functions shown in Figure 3-30 and Figure 3-32 imply that the FU&PG-MM compensator provides stability robustness for the two off-nominal factors, and the design requirements are satisfied. While the pole-zero pattern is disordered by the off-nominal factors as observed in Figure 3-31 and Figure 3-33, the expanded distances in damping ratio direction between the poles and zeros keep the phase of the loop transfer functions bounded between $0 deg$ and $-180 deg$.

LQG cost of the closed loop system with the FU&PG-MM compensator illustrated in Figure 3-34 indicates the MM method expands the stable region around the nominal point, which includes the four off-nominal design points, ±10% frequency uncertainties in the second bending mode and $\pm 45 deg$ primary gimbal angle. Furthermore, the MM method provides excellent robust performance within the required off-nominal region. The performance degradation is kept less than 5% within the entire region around all design points.

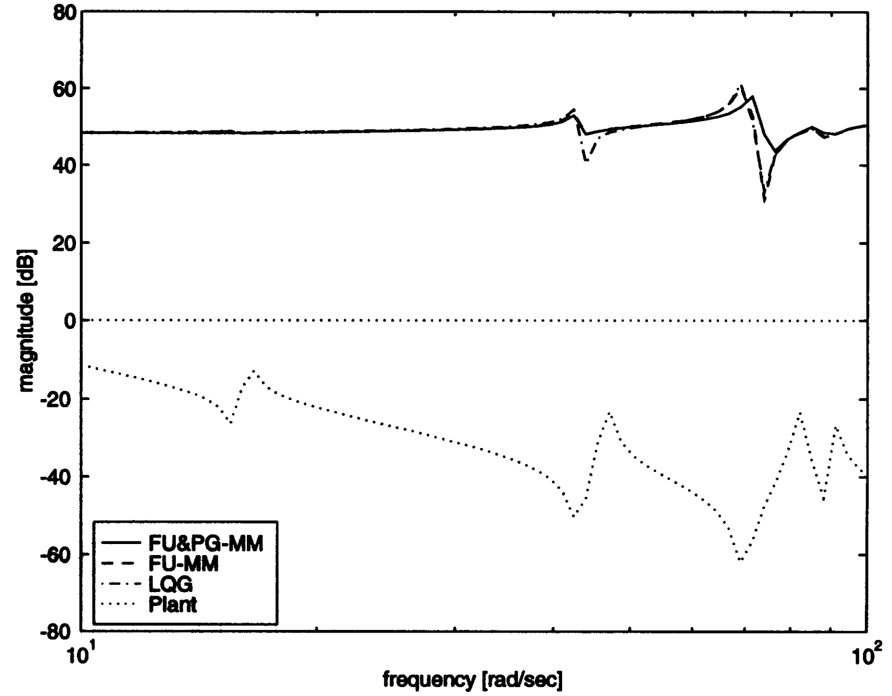

Figure 3-28: Frequency responses of the FU&PG-MM compensator and the plant system

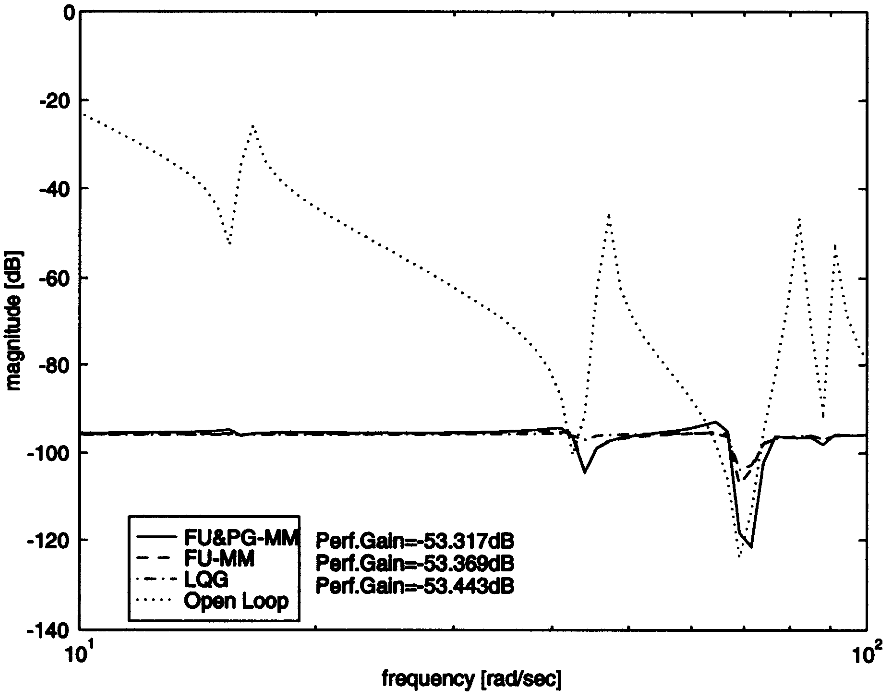

Figure 3-29: Performance of the FU&PG-MM compensator

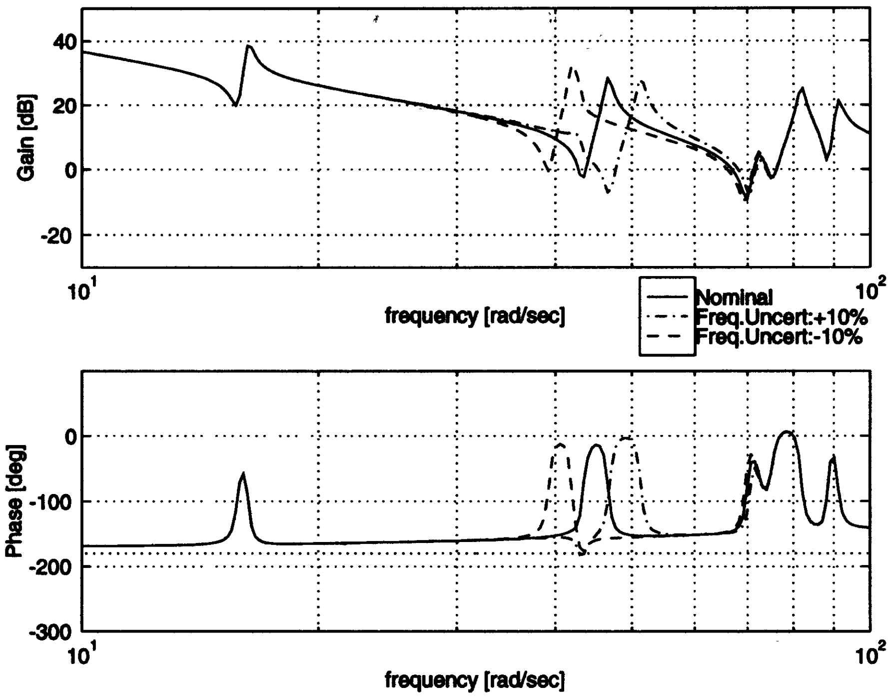

Figure 3-30: Bode plots of the loop transfer functions of the FU&PG-MM compensator and the plant system disturbed in the second mode frequency

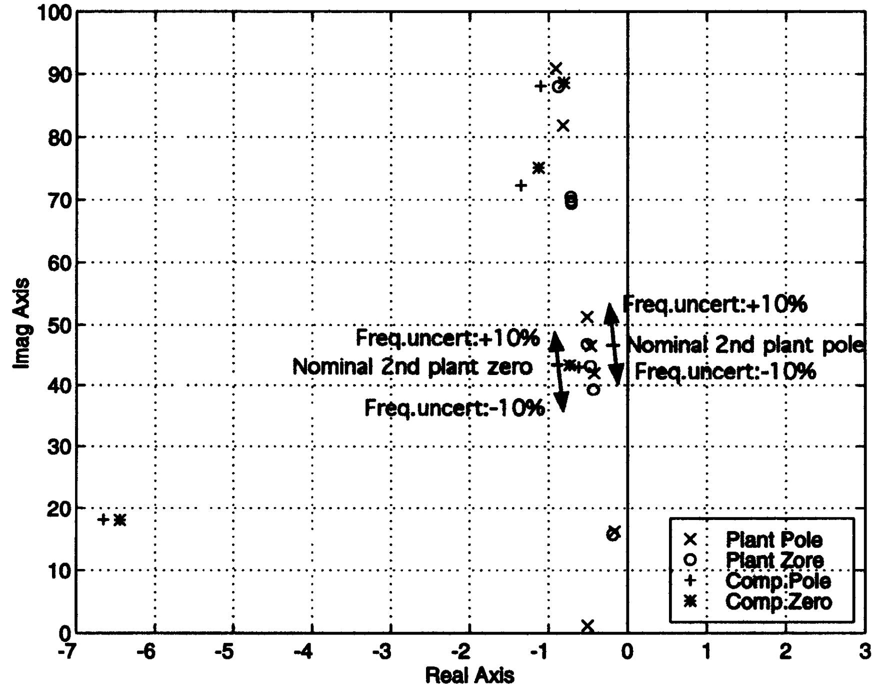

Figure 3-31: Pole-zero location of the FU&PG-MM compensator and the plant system disturbed in the second mode frequency

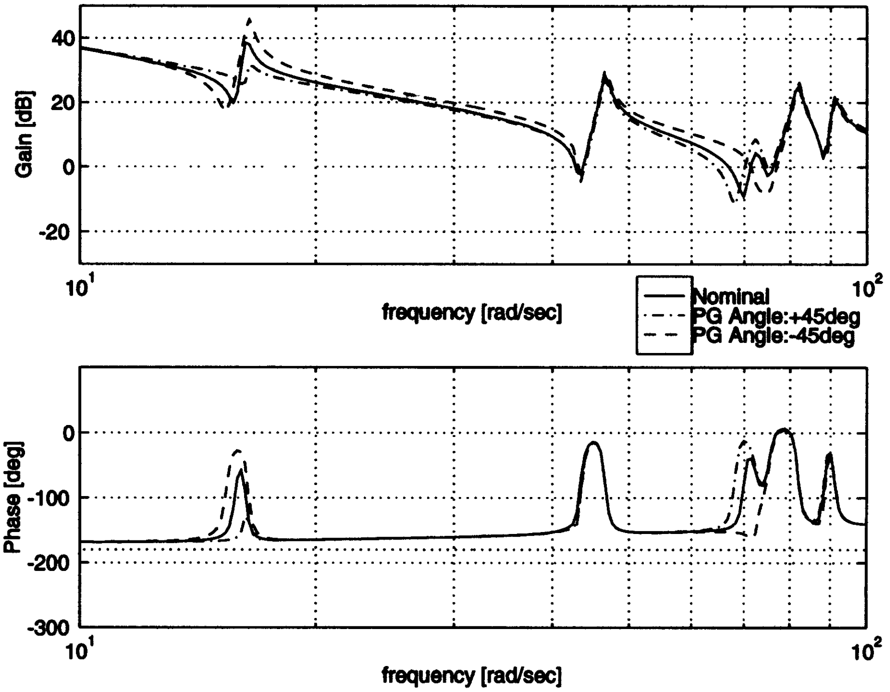

Figure 3-32: Bode plots of the loop transfer functions of the FU&PG-MM compensator and the plant system disturbed by the primary gimbal average angle

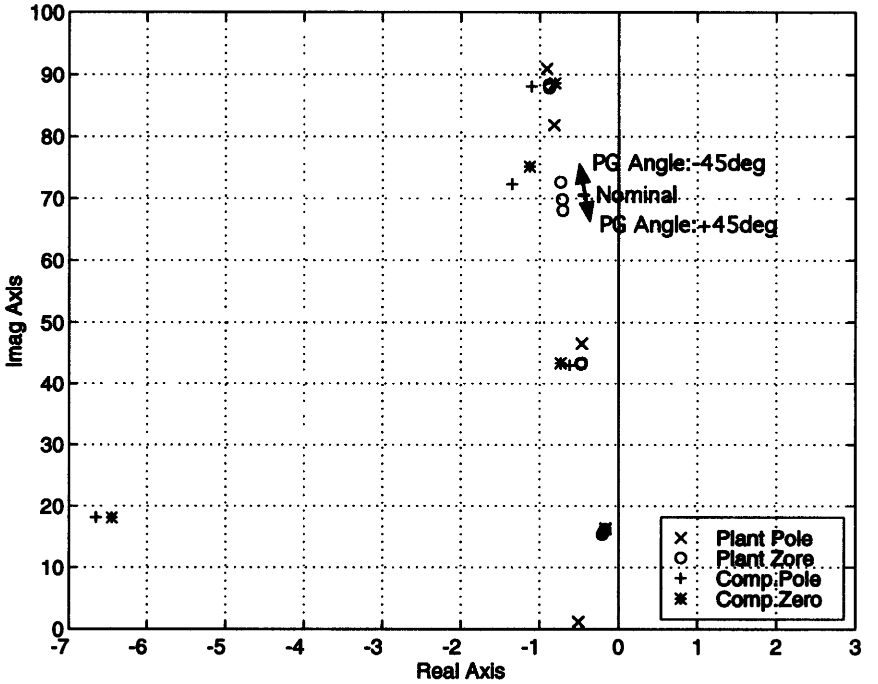

Figure 3-33: Pole-zero location of the FU&PG-MM compensator and the plant system disturbed by the primary gimbal average angle

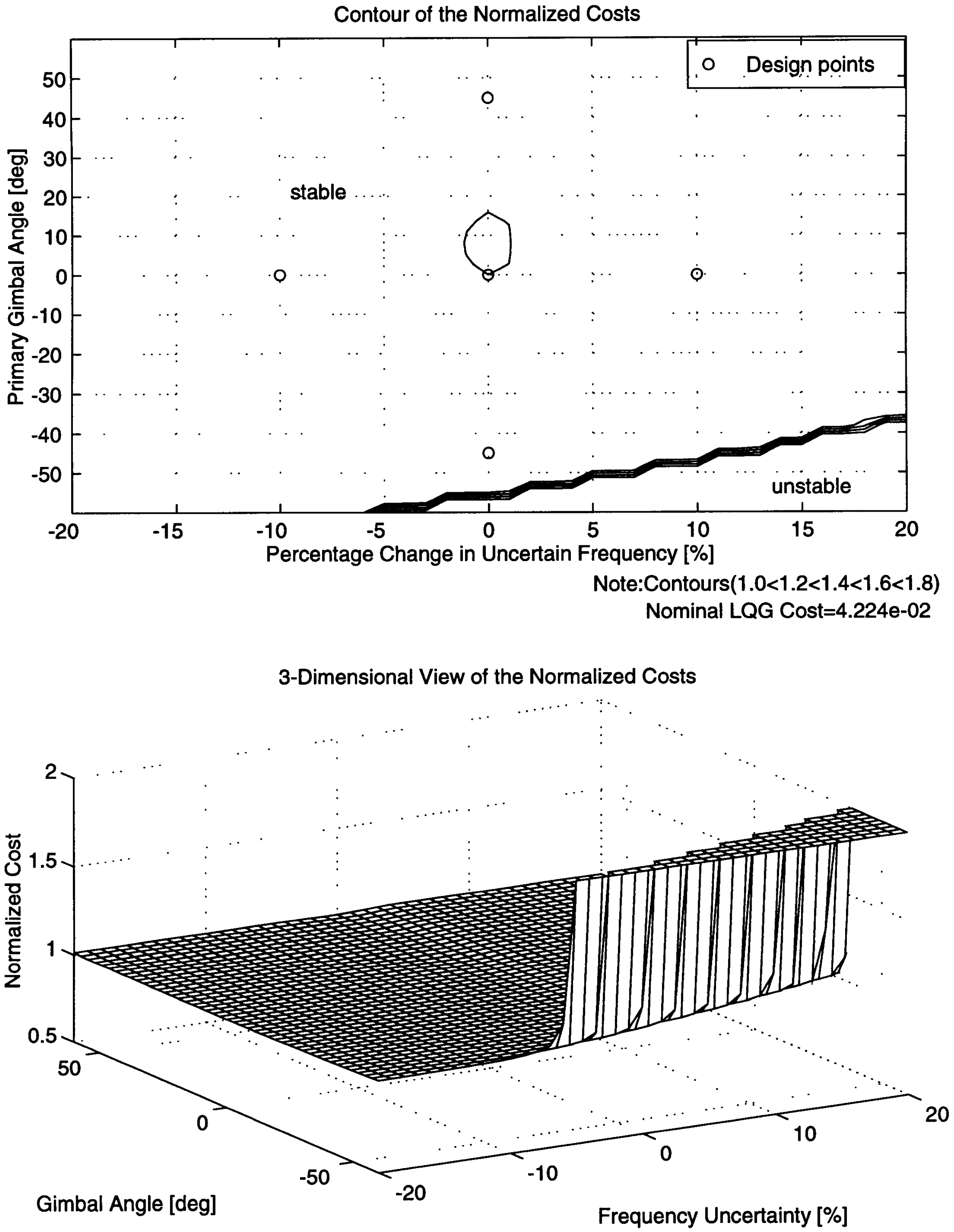
Contour of the Normalized Costs

Note:Contours(1.0<1.2<1.4<1.6<1.8)
Nominal LQG Cost=4.224e-02

3-Dimensional View of the Normalized Costs

Figure 3-34: LQG cost of the closed loop system with the FU&PG-MM compensator

3.4 Conclusions

The MM solution, which stabilizes the SISO MACE plant system with two off-nominal factors, is obtained successfully in this control design. The most outstanding feature of the MM method is to enhance robust stability and robust performance of compensators with small losses of nominal performance.

Figure 3-35 shows this valuable feature very well. The LQG costs of the closed loop system with the LQG, FU-MM, and FU&PG-MM compensators are plotted as functions of frequency uncertainty or primary gimbal angle. Note that the LQG costs are normalized with the nominal LQG cost of the LQG compensator (4.186×10^{-2}). The plot indicates that the two MM compensators provide robust stability for the targeted off-nominal deviations, the ±10% frequency uncertainty and $\pm 45 deg$ primary gimbal average angle, and robust performance. The degradation of performance is less than 5% within the desired off nominal region. Furthermore, the nominal LQG cost of the FU&PG-MM compensator exceeds that of the LQG compensator by only 0.9%. This implies that both compensators have almost the same nominal performance.

Therefore, the designs made in this section conclude that the MM method is an excellent robust control design technique for plant systems with multiple parameterized off-nominal factors. However, control designers have to be aware of the drawback of the MM method, the large computational load.

There are some factors which increase the computational load in the MM method. At first, a numerical optimization method has to be adopted to find the optimal MM solution, because there is no analytical equation which gives the MM solution. In any numerical optimization method, several iterative calculations must be performed to find a converged solution. Secondly, because targeted off-nominal design points are usually outside of the stable region of the original compensator, several intermediate design steps need to be set. In each design step, the deviation of the off-nominal design points from the nominal is increased. Thirdly, because the number of the variables in the optimization calculation is large and the LQG cost is a highly nonlinear function, the numerical calculation is very sensitive. Therefore, the increment of the deviation in each design step has to be small enough to prevent numerical instability in the optimization calculation. Finally, if plant systems have multiple types of off-nominal factors, outer design steps need to be set. The number of outer design steps is the same as that of off-nominal factors.

In the MM design in this chapter, for instance, two outer design steps are set, since there are two types of off-nominal factors. In each outer design step, nine inner design steps for the frequency uncertainty and seven inner design steps for the primary gimbal average angle are set to reach the targeted off-nominal deviations. In each inner design step, more than 100 iterative calculations need to be performed before finding the optimal solution.

Fortunately, the recent development of control design tools, such as MATLAB [39], allows designers to adopt the MM method as a practical robust design technique.

Another matter to be attended to is to find local minimum points instead of a real minimum point. This is a general problem in optimization of a multivariable function. While local minimum solutions guarantee stability for designated off-nominal design points, they bring about worse robust performance than that of a real optimal solution and a wasteful degradation of a nominal performance.

To avoid capturing local minimum solutions, more than one initial guesses should be examined. If every initial guess gives the same solution, the solution is the most likely optimal solution. Another measure for the local minimum problem is the method of progressively moving the off-nominal design points, which is used in the designs in this section. Because LQG solutions used as an initial guess are a optimum solution, a MM solution for off-nominal design points with a small increment of deviation is not significantly different from the original LQG solution or the previous MM solutions. Plots of the weighted sum of the LQG costs and the nominal LQG cost shown in Figure 3-36 are helpful to avoid obtaining local minima. Both values in the FU-MM and FU&PG-MM designs vary smoothly. Therefore, the MM solutions obtained in this section are likely optimal solutions.

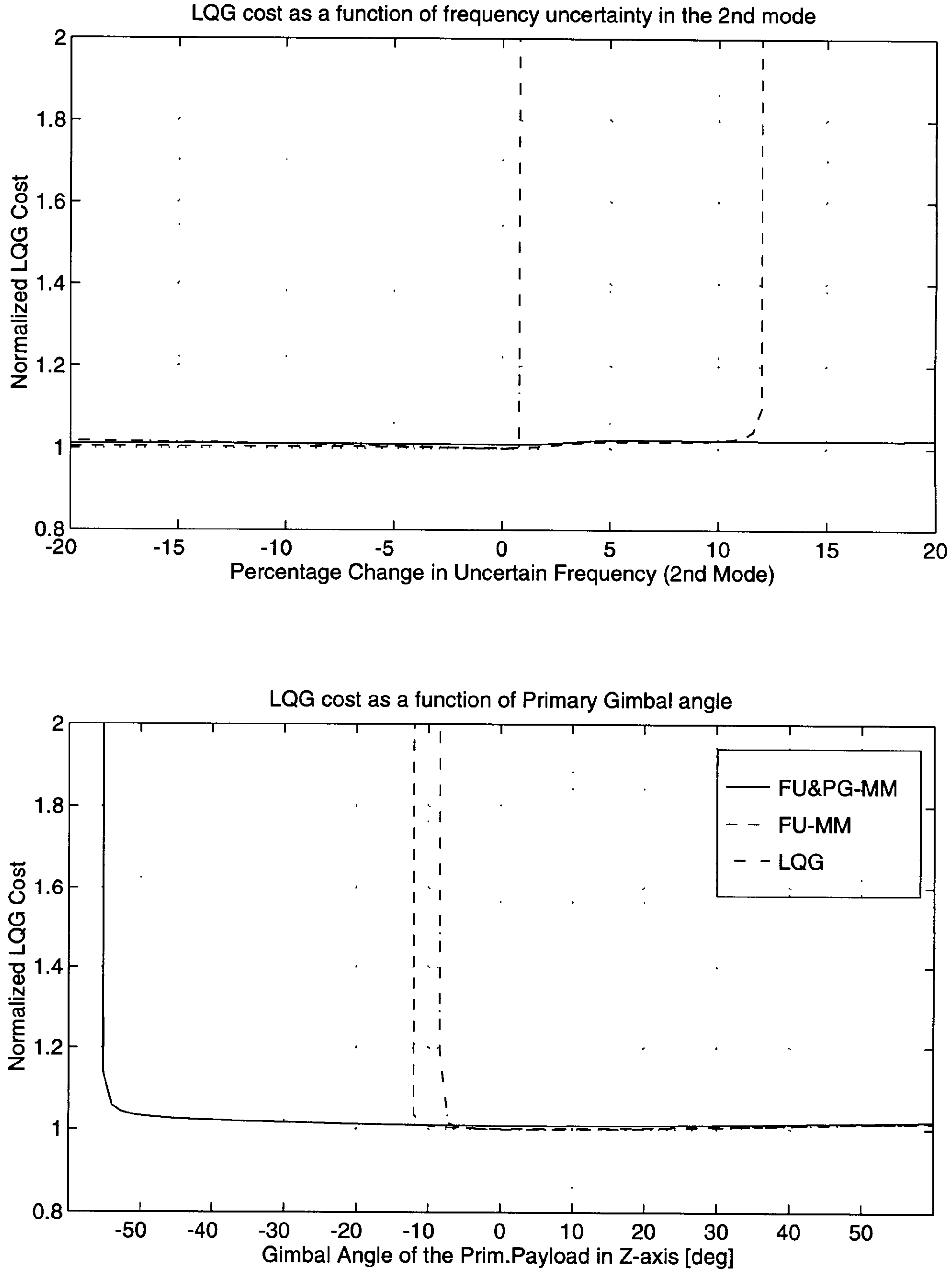

Figure 3-35: Comparison of LQG costs of the MM compensators

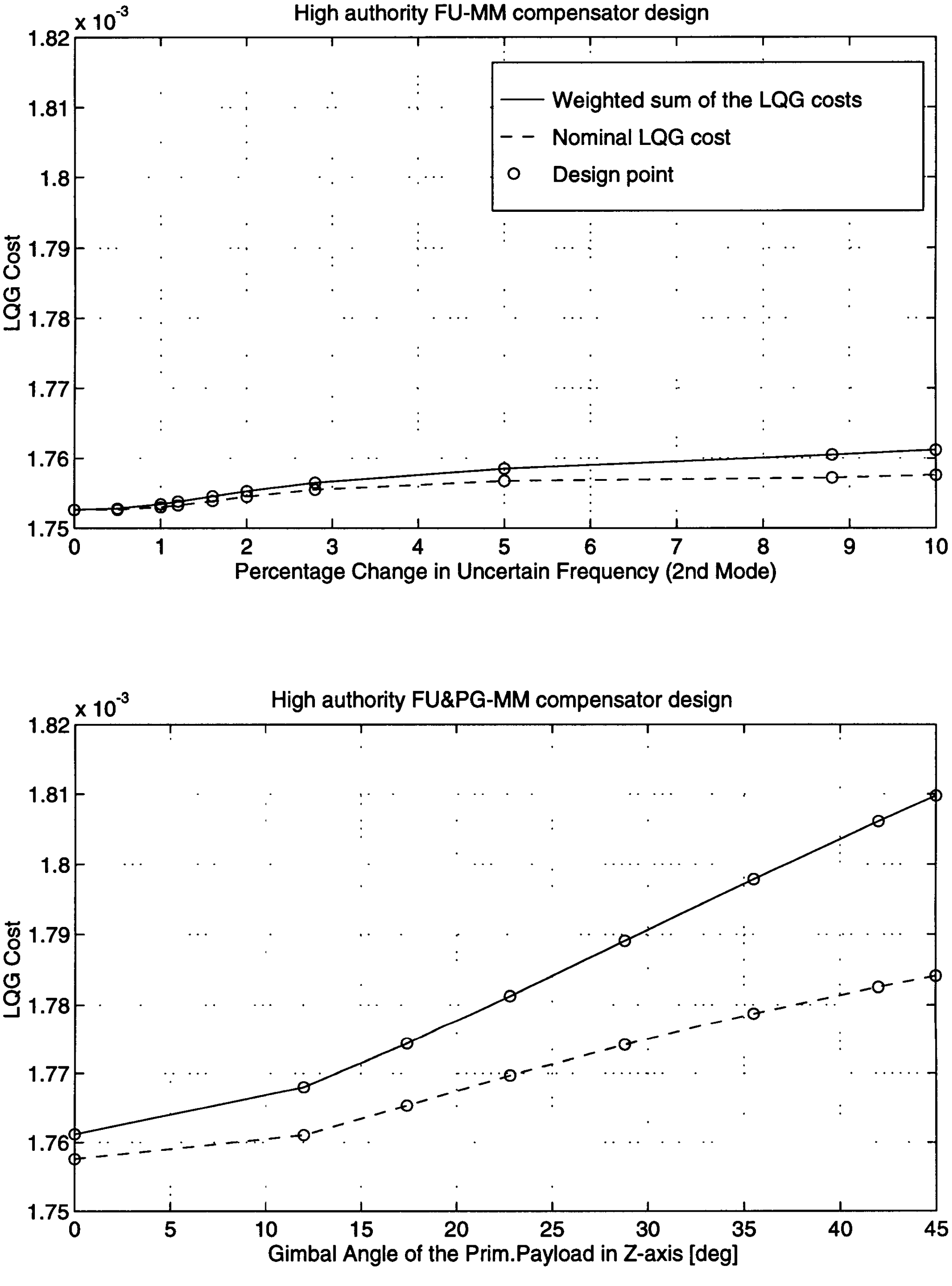

Figure 3-36: Changes of the weighted sum of the LQG costs and the nominal LQG cost in the MM designs

Chapter 4

MIMO Control Designs for the 4-Mode Flexible MACE Model

In the previous chapter, robust compensators for the SISO plant system of the 4-mode flexible MACE model are successfully obtained. The MM technique demonstrates that it effectively expands the stability bounds of the LQG compensators which are used as an initial compensator in an optimization calculation. The control input, disturbance input, sensor output, and performance output are collocated at the same position in the SISO problem.

In real design problems, however, inputs and outputs are more than one and they are not collocated. In particular, disturbance inputs are located at different places from those of sensor and performance outputs. Future space systems, such as space stations and space platforms, have multiple missions and a complicated bus system. Many kinds of mission systems including movable devices are equipped to the space systems and can be a disturbance source for each other. The control designers for the future space systems are faced with a MIMO problem.

The MACE test article is designed as a typical future space system and has seven actuators and nine sensors. The secondary gimbal can simulate an uncollocated disturbance source. In this chapter, the MIMO problem for the 4-mode flexible MACE model is dealt with as a more realistic design problem.

4.1 MIMO Problem

This section presents the MIMO problem for the 4-mode flexible MACE model. At first, the MIMO model and two off-nominal factors are defined. The two off-nominal factors are frequency uncertainty in all Z-axis bending modes and primary gimbal average angle. Secondly, the effects of the off-nominal factors on the MIMO model are examined. Finally, the design strategy in the MIMO problem follows the model definition.

4.1.1 MIMO Plant System

The 4-mode flexible MACE model, which is developed in Section 3.1, simulates the X-Y plane dynamics of the MACE test article. This model has three actuators and three sensors; the former is the primary and secondary gimbals and the reaction wheel, and the latter, two inertial rate gyros and one encoder. The secondary gimbal acts as a disturbance source, which is located at a different place from the other inputs and outputs. Figure 4-1 illustrates the MIMO plant system of the 4-mode flexible MACE model, and Table 4.1 summarizes the configuration of the MIMO plant system.

The objective in the MIMO problem is to design compensators to control the attitude of the entire body and the primary gimbal position in a large angle tracking mode in the presence of the disturbance produced by the secondary gimbal. The design requirement for the compensators is to obtain guaranteed robustness for the following two off-nominal factors:

- $\pm 2.5\%$ frequency uncertainties in all Z-axis bending modes;
- $\pm 45 deg$ primary gimbal average angles.

The MIMO plant has the same four Z-axis bending modes as the SISO system listed in Table 4.2. The influence of the off-nominal factors on the MIMO system can be observed in the singular value plots of the plant system illustrated in Figures 4-2 and 4-3. Because of the constant percentage in the frequency uncertainty for all

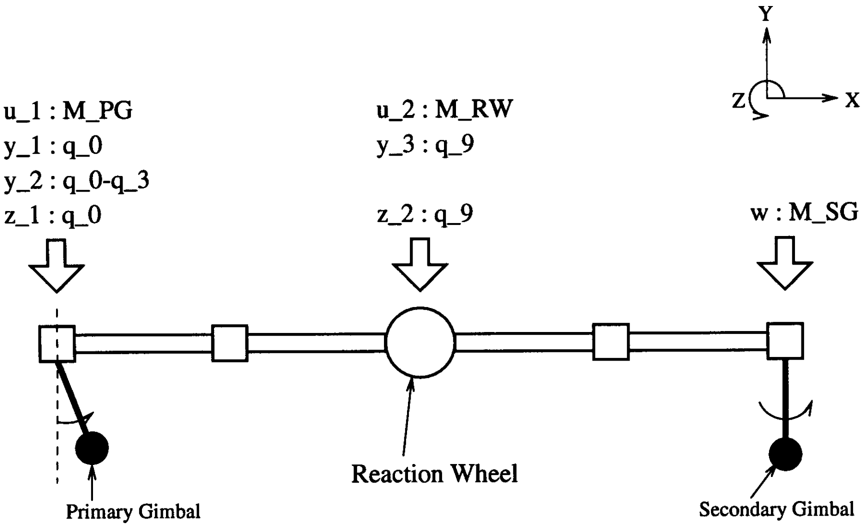

Figure 4-1: MIMO plant system of the 4-mode flexible MACE model

modes, the higher Z-axis bending mode has a larger frequency deviation as shown in Figure 4-2. On the other hand, Figure 4-3 indicates that changes of the primary gimbal angle mainly influence the first mode at $2.6Hz$. In particular, the plant system is more sensitive to the negative primary gimbal angle change.

From both plots, the two off-nominal factors differently affect the MIMO plant. Therefore, it is meaningful to set off-nominal design points with respect to both off-nominal factors.

Table 4.1: Configuration of the MIMO plant system of the 4-mode flexible MACE model

item	contents
Order of the system	10 (4 Z-bending modes & primary gimbal rotational mode)
Control input	Primary gimbal torque about Z axis at the end node #1
	Reaction wheel torque about Z axis at the center node
Sensor output	Relative angle, $q_0 - q_3$, about Z axis at the end node (Encoder output)
	Inertial angle of the primary gimbal's payload, q_0, about Z axis at the end node #1 (Rate gyro output)
	Inertial angle of the center node, q_9, about Z axis (Rate gyro output)
Disturbance input	Secondary gimbal's disturbance torque about Z axis at the end node #2 (uncollocated at the positions of the control inputs)
Performance output	Inertial angle of the primary gimbal's payload, q_0, about Z axis at the end node #1 (collocated at the same position of the sensor output)
	Inertial angle of the center node, q_9, about Z axis (collocated at the same position of the sensor output)

Table 4.2: Nominal bending modes of the 4-mode flexible MACE model

Description	Nominal Frequency [Hz]	Nominal Damping Ratio
1st Z-bending mode	2.59	0.01
2nd Z-bending mode	7.42	0.01
3rd Z-bending mode	13.02	0.01
4th Z-bending mode	14.47	0.01

(Note) Reproduction of Table 3.2 in Section 3.1.1.

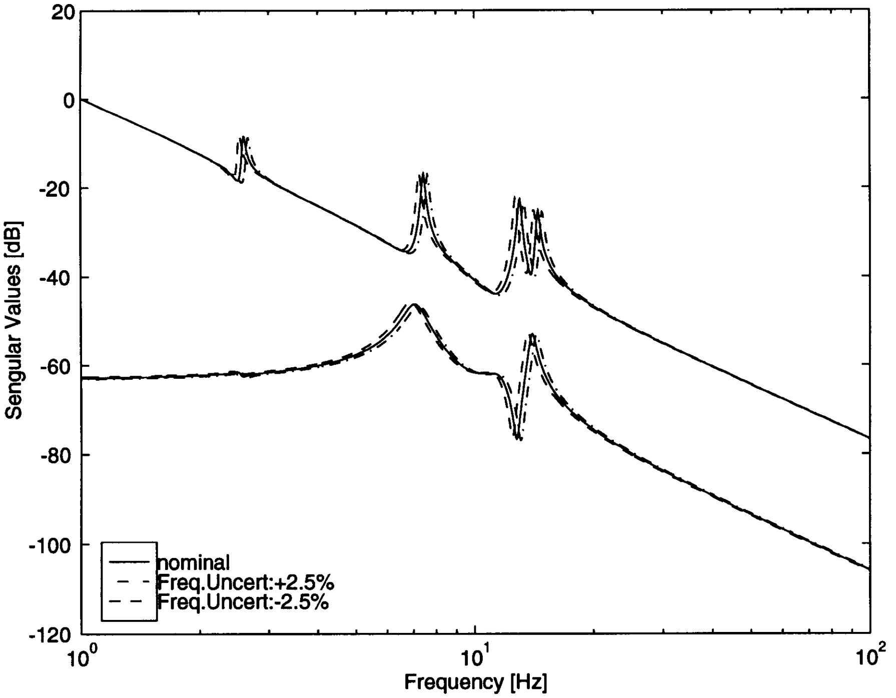

Figure 4-2: Singular value plots of the transfer matrix from the control inputs to the sensor outputs of the MIMO plant with the frequency uncertainty changes

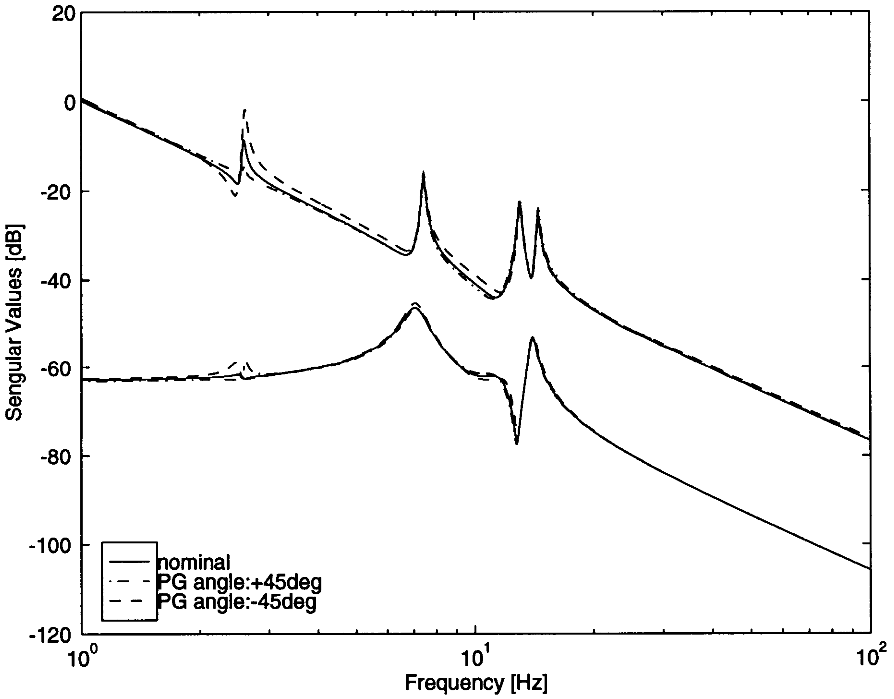

Figure 4-3: Singular value plots of the transfer matrix from the control inputs to the sensor outputs of the MIMO plant with the primary gimbal angle changes

4.1.2 Design Strategy

The same design procedure as that of the SISO design in Chapter 3 is followed in the MIMO design. LQG compensators, which have different levels of control authority, are designed at first and are used as an initial matrix set for the following MM designs.

While the number of the state variables in the MIMO plant is the same as that in the SISO plant, the MIMO plant has two control outputs and three sensor inputs. Thus, the number of control weights is doubled and the number of sensor noise weights is tripled. Tuning those weights to obtain high performance compensators is a very important procedure in LQG design. However, the main objective of this study is to demonstrate the effectiveness of MM designs. Therefore, scalar weights, ρ and θ introduced by Equations (2.25) and (2.26) in Section 2.1.1, are adopted in the MIMO design.

The MM designs are divided into two design series; FU-MM designs and FU&PG-MM designs. FU-MM compensators guarantee robust stability for the off-nominal factor of frequency uncertainty, while FU&PG-MM compensators guarantee robust stability for both of the off-nominal factors of frequency uncertainty and primary gimbal average angle. Therefore, three design points and five design points are designated in the two design series, respectively.

The basic strategy of setting cost weights, β_i, is that performance robustness takes precedence with respect to the primary gimbal average angle, while stability robustness takes precedence with respect to the frequency uncertainty. This is because high performance is demanded at any primary gimbal average angle, while stability is required at least within the designated frequency uncertainty region. Therefore, the cost weights are set as follows in each design series: 0.9 for the nominal design point and 0.05 for the two off-nominal design points with respect to frequency uncertainty in the FU-MM designs; 0.3 for the nominal point and two off-nominal points with respect to primary gimbal average angle and 0.05 for the two off-nominal points with respect to frequency uncertainty in the FU&PG-MM designs. These cost weights allow us to expect that a resulting MM compensator keeps equivalent performance for $\pm 45 deg$ primary gimbal average angle.

In the MM designs, the progressive method, in which the off-nominal design points are expanded in each design step, is adopted. The MM designs start with the LQG compensators obtained in advance. Although there is no guarantee to obtain the global minimum point, the progressive method is useful in reducing the possibility of capturing local minimum points.

4.2 LQG Designs

Three LQG compensators are designed and examined in this section. They are called low authority, middle authority, and high authority. By setting a control weight, ρ, and using the Balanced Weight Condition introduced in Section 2.1.2, a sensor noise weight, θ, is uniquely determined. The resulting balanced weights are listed in Table 4.3 with performance gains and nominal LQG costs. The LQG technique easily gives compensators with high nominal performance.

The singular values of the LQG compensators are plotted in Figure 4-4. The higher the control authority is, the higher gains it has in the entire frequency region. In particular, the gains of the high authority compensator above $100 rad/sec$ are considerably higher than the others. The performance plots illustrated in Figure 4-5 indicate that the performance of the high authority compensator below $100 rad/sec$ is improved from that of the low authority compensator by $40 dB$, while the performance above $200 rad/sec$ is lower than the low authority compensator's. This is because the frequencies of all modes of the plant are below $100 rad/sec$. However, the net result is that the performance of the high authority compensator is better than that of the low authority compensator by $16 dB$, as listed in Table 4.3.

The LQG cost plots as a function of frequency uncertainty or primary gimbal angle, illustrated in Figure 4-6, reveal that the high authority compensator has poor robustness for positive frequency uncertainty, while it has excellent nominal performance. Note that the LQG costs are normalized by the nominal LQG cost of the high authority compensator. The stability boundaries for both off-nominal factors are

Table 4.3: Summary of the LQG designs for the MIMO, 4-mode flexible MACE model

Design Case	Weights			Performance	Nominal
	State	Control	Sensor Noise	Gain	LQG Cost
Control Authority	C_z	D_{zu}	D_{yw}		
		ρ	θ	$[dB]$	
Low	1.0	3.50×10^{-3}	2.9875×10^{-3}	−37.685	4.863×10^{-2}
Middle	1.0	1.00×10^{-3}	1.5169×10^{-3}	−42.040	2.936×10^{-2}
High	1.0	1.00×10^{-4}	3.5024×10^{-4}	−53.889	7.882×10^{-3}

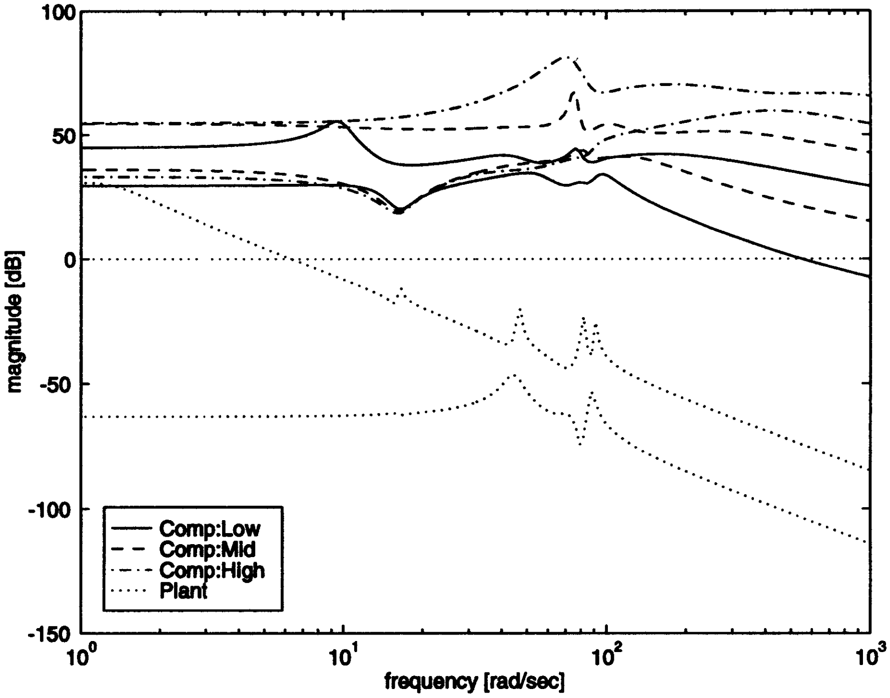

Figure 4-4: Singular value plots of the LQG compensators and the plant system

listed in Table 4.4. The three LQG compensators do not satisfy the design requirement; robust stability for ±2.5% frequency uncertainty and $\pm 45deg$ primary gimbal average angle.

The LQG costs as a function of both off-nominal factors are illustrated in Figures 4-7, 4-8, and 4-9. These plots show the compensator's robust stability and performance for the combination of the two off-nominal factors. Note that the outermost contour in the two-dimensional plots corresponds to the boundary of the stable region, and that the flat surfaces in the three-dimensional plots roughly correspond to the unstable region.

These plots reveal that the stability boundary in the positive side of the frequency uncertainty comes close to the nominal design point as the control authority is increased, while the stable region in the negative side of the frequency uncertainty becomes wider. This is because, as observed in the SISO designs in Section 3.2 (Figure 3-6), all compensator poles and zeros are located between a corresponding plant zero and pole, and approach plant zeros from higher frequency side as the control

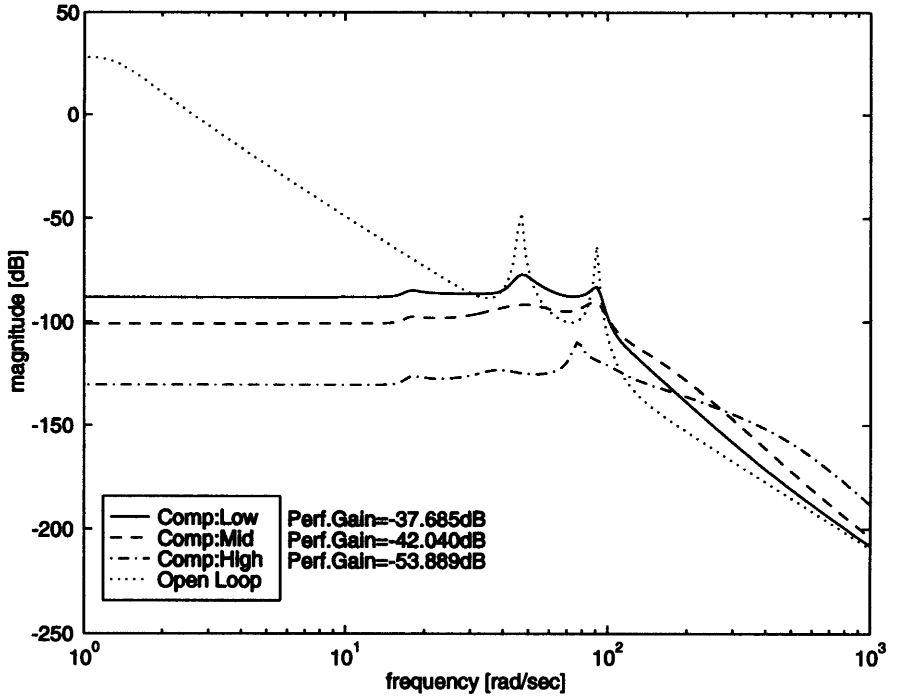

Figure 4-5: Performance of the LQG compensators

authority is increased. However, these poles and zeros keep their pattern in the frequency direction: plant zero-compensator pole-compensator zero-plant pole from lower frequency to higher frequency. Therefore, the higher authority LQG compensator has smaller frequency separation between a compensator pole and a plant zero, while it has larger frequency separation between a compensator zero and a plant pole. The smaller positive frequency uncertainty destabilizes the closed loop system with the higher authority compensator, while the system can endure the larger negative frequency uncertainty.

Although the plots in Figures 4-7, 4-8, and 4-9 show that the higher authority LQG compensator has wider stability region, the stability region of the higher authority compensator extends eccentrically in the negative direction of the frequency uncertainty. And the higher authority compensator's performance robust region in which the normalized LQG cost is less than two is narrower. Note that *performance robust region* indicates a region where performance is insensitive to off-nominal parameter variations. These imply that the higher authority compensator has poorer

Table 4.4: Stability boundaries of the LQG compensators

Design Case	Frequency Uncertainty [%]		Primary Gimbal Angle [*deg*]	
	lower	upper	lower	upper
Low LQG	-2.40	4.80	-42.0	> 60.0
Mid. LQG	-12.00	5.20	-36.0	> 60.0
High LQG	-18.80	1.60	-33.6	> 60.0

robust performance.

In all LQG design cases, one or two targeted design points are outside of the stability region. Therefore, the robustness of the LQG compensators need to be improved by the MM technique to achieve the design requirements.

Since the plant in this design is a MIMO system, the Bode plot cannot be used to examine stability. Instead, the Nichols plot based on the Multivariable Nyquist Criterion and the sensitivity plot introduced in Section 2.3.2 indicate stability and sensitivity information. Figures 4-10 and 4-11 show the Nichols plots in the case of the high authority compensator. Since this compensator has two sets of unstable poles, the closed loop system is stable if the number of left to right passes over the critical points is two. Notice that the plant system only has stable poles.

The top plot in Figure 4-10 shows the Nichols plot of the nominal case which has two left-to-right passes over the critical points. This implies that the nominal closed loop system is stable. However, the middle plot in Figure 4-10, which shows the Nichols plot in the case of +2.5% frequency uncertainty in all modes, indicates that the closed loop system is unstable because there is only one left-to-right pass. In fact, the closed loop system has an unstable pole at $83 rad/sec$. The Nichols plot between $80 rad/sec$ and $90 rad/sec$, which is emphasized in Figure 4-10, passes under the critical point. This relates to the unstable closed loop pole at $83 rad/sec$.

In general, however, it is difficult to predict sensitivity of stability from the Nichols plot. For example, The Nichols plot between $80 rad/sec$ and $90 rad/sec$ in the nominal case is not the nearest to the critical point in Figure 4-10. The sensitivity plot supplements this defect of the Nichols plot. Note that the sensitivity plot means a minimum singular value plot of $I + G_{yu}(j\omega)\, K(j\omega)$.

Figure 4-12 shows the sensitivity plots of the nominal case and two off-nominal cases: $+1.0\%$ frequency uncertainty case; $-30deg$ primary gimbal angle case. The closed loop system is stable in both off-nominal cases. In $+1.0\%$ frequency uncertainty case, the upper plot in Figure 4-12, there is a large difference between the nominal and off-nominal plots around $80rad/sec$. This difference implies that the closed loop system is sensitive to the frequency uncertainty and can be destabilized at that frequency by the frequency uncertainty. In the same way, in $-30deg$ primary gimbal angle case, the lower plot in Figure 4-12, a large difference between the nominal and off-nominal plots is observed around $15rad/sec$. This also implies that the closed loop system is sensitive to the primary gimbal angle change at that frequency. These observations correspond with the Nichols plots in Figures 4-10 and 4-11.

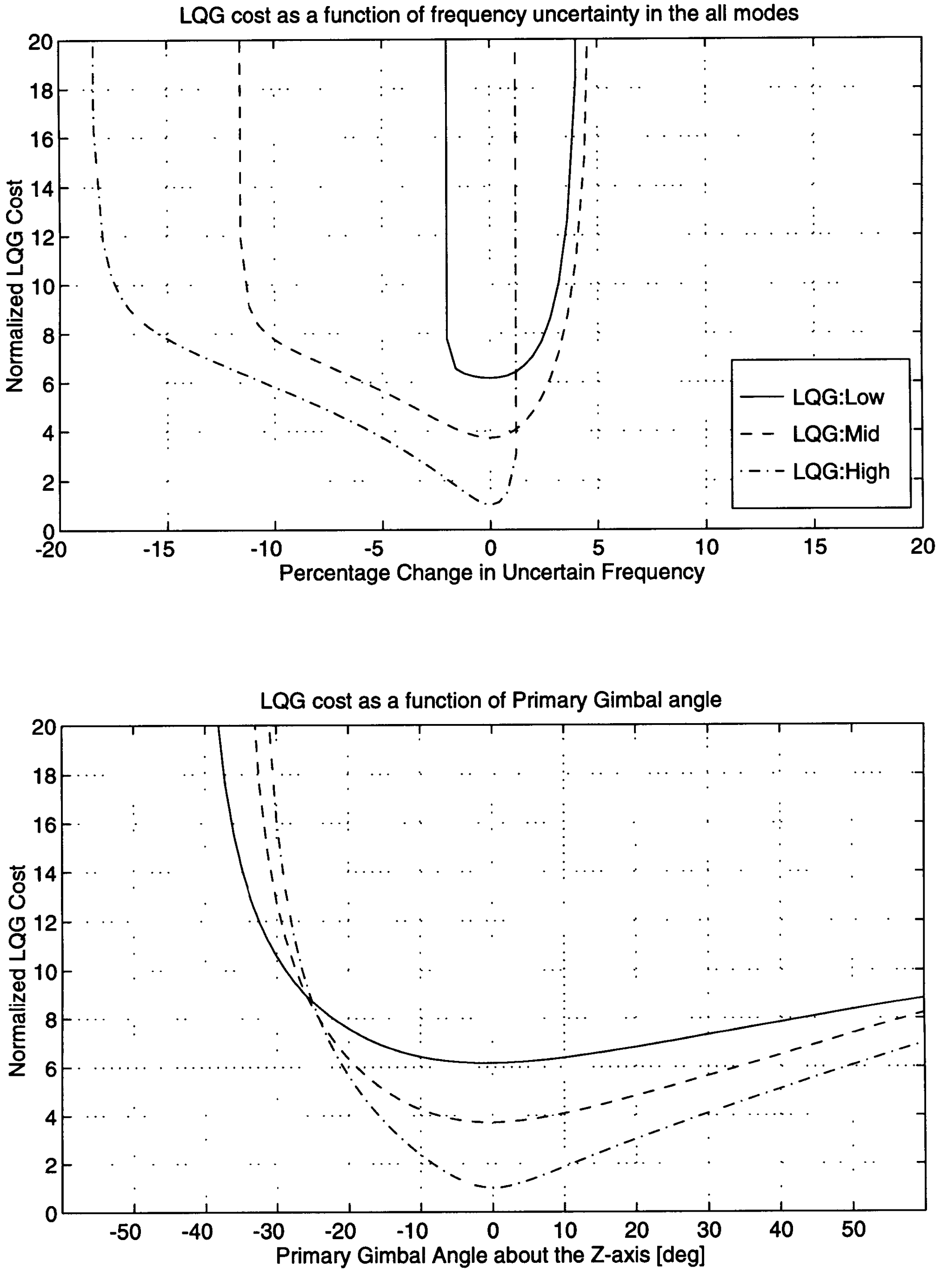

Figure 4-6: Comparison of the LQG costs of the LQG compensators

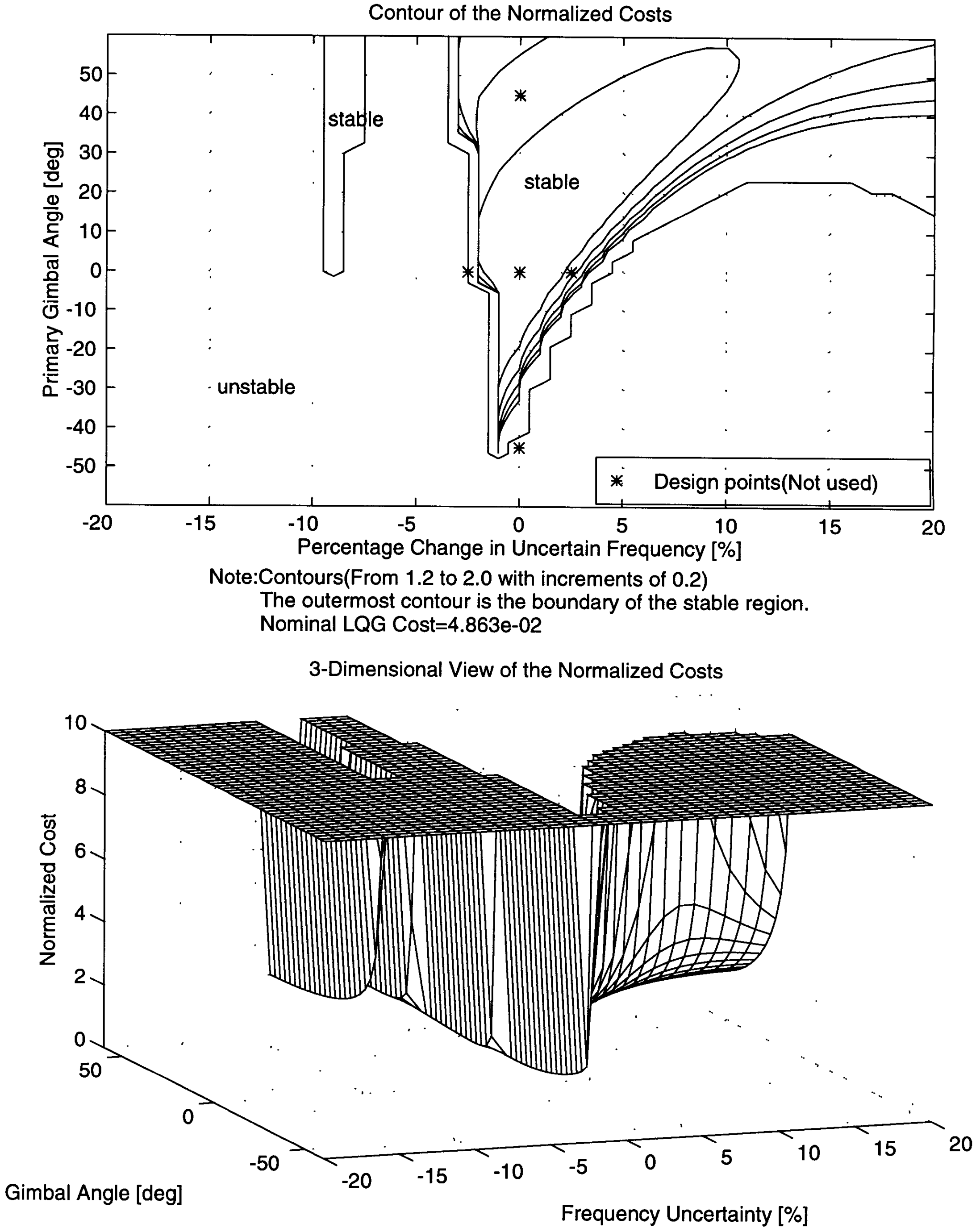

Contour of the Normalized Costs

Note:Contours(From 1.2 to 2.0 with increments of 0.2)
The outermost contour is the boundary of the stable region.
Nominal LQG Cost=4.863e-02

3-Dimensional View of the Normalized Costs

Figure 4-7: LQG cost of the closed loop system with the low authority LQG compensator

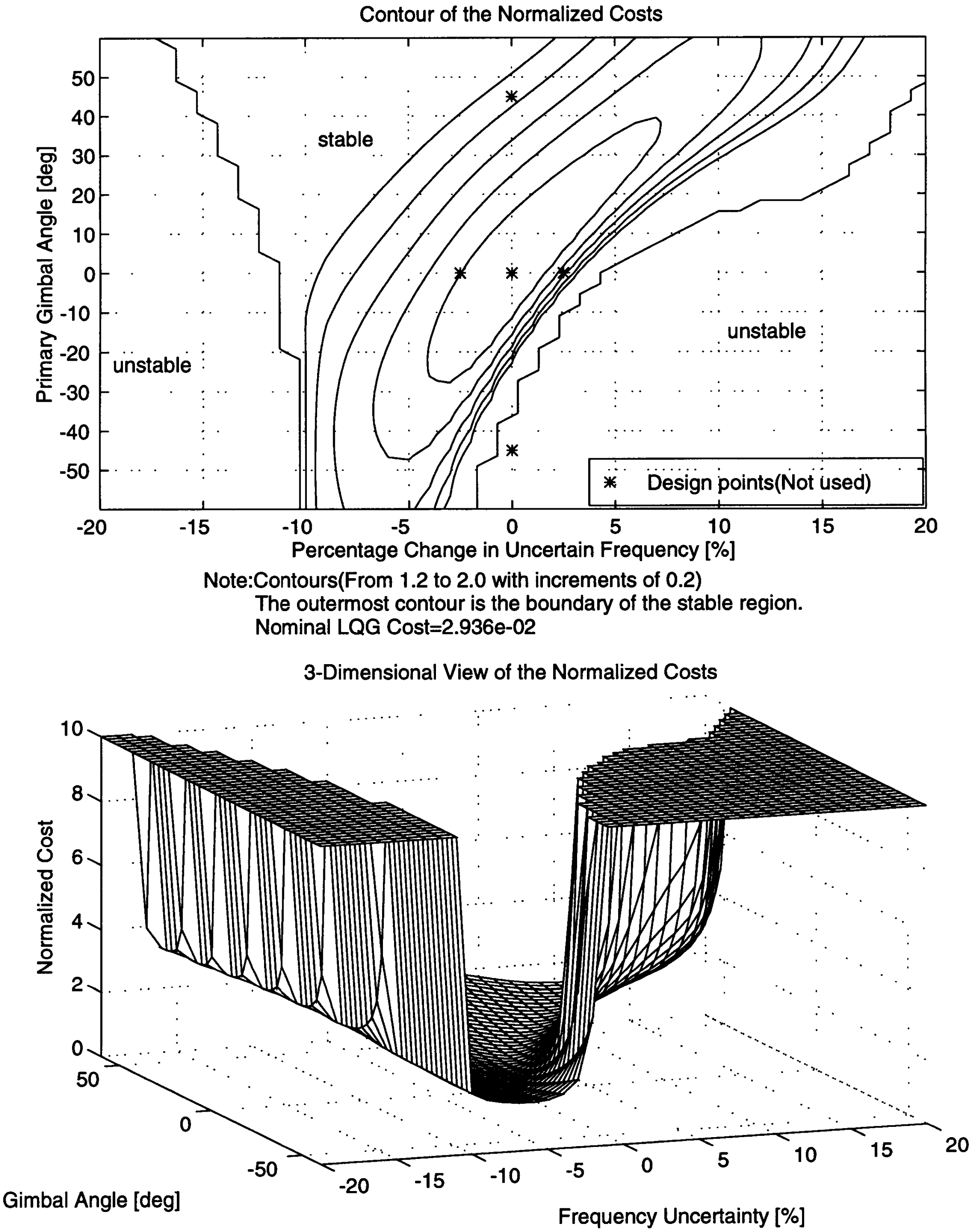

Figure 4-8: LQG cost of the closed loop system with the middle authority LQG compensator

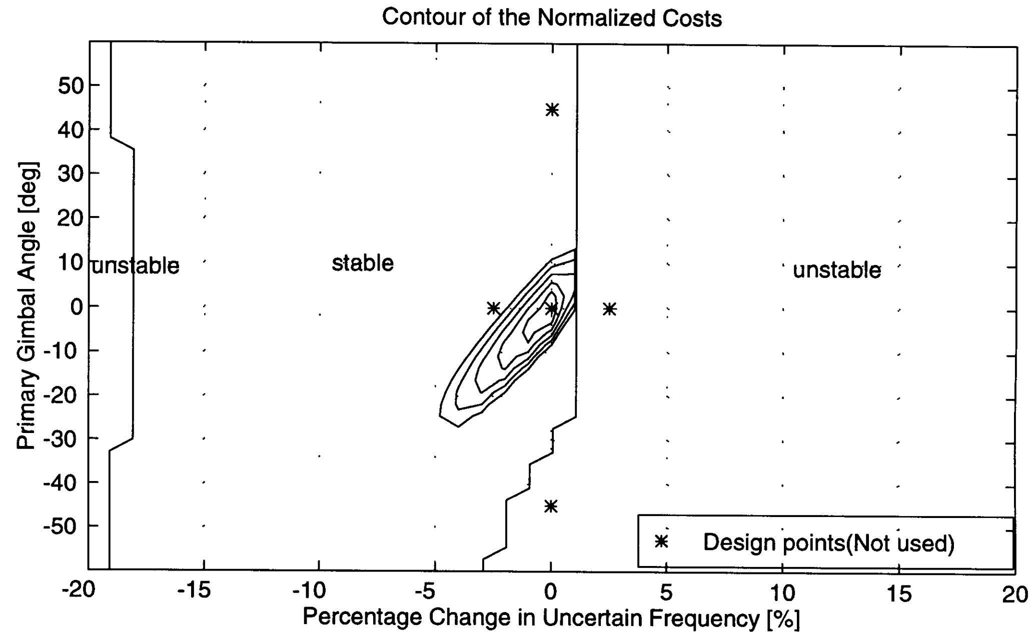

Contour of the Normalized Costs

Note:Contours(From 1.2 to 2.0 with increments of 0.2)
The outermost contour is the boundary of the stable region.
Nominal LQG Cost=7.882e-03

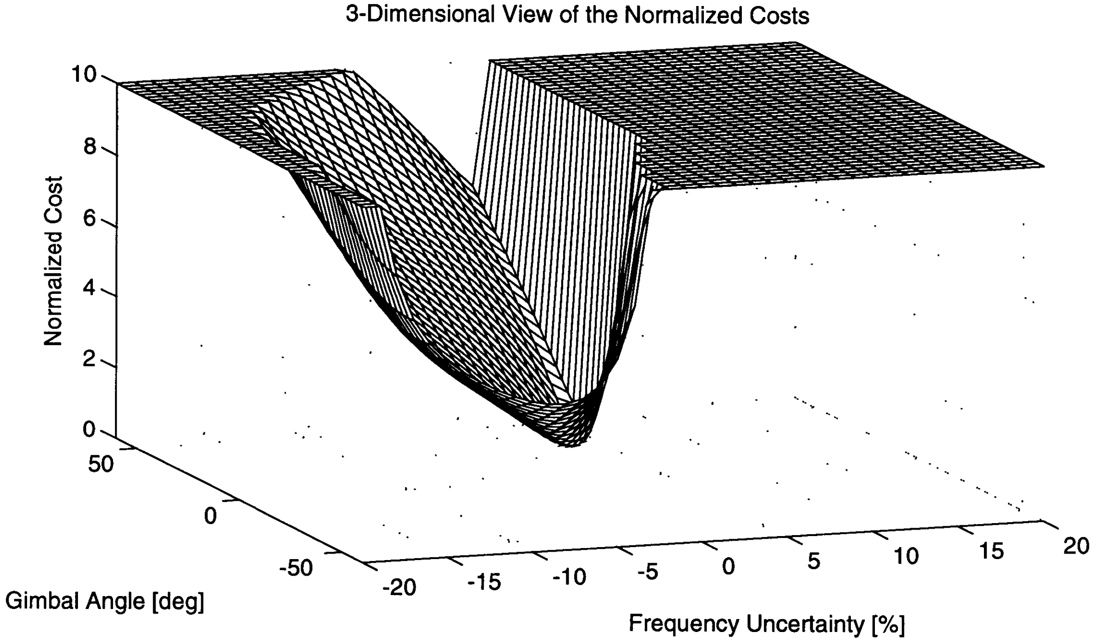

3-Dimensional View of the Normalized Costs

Figure 4-9: LQG cost of the closed loop system with the high authority LQG compensator

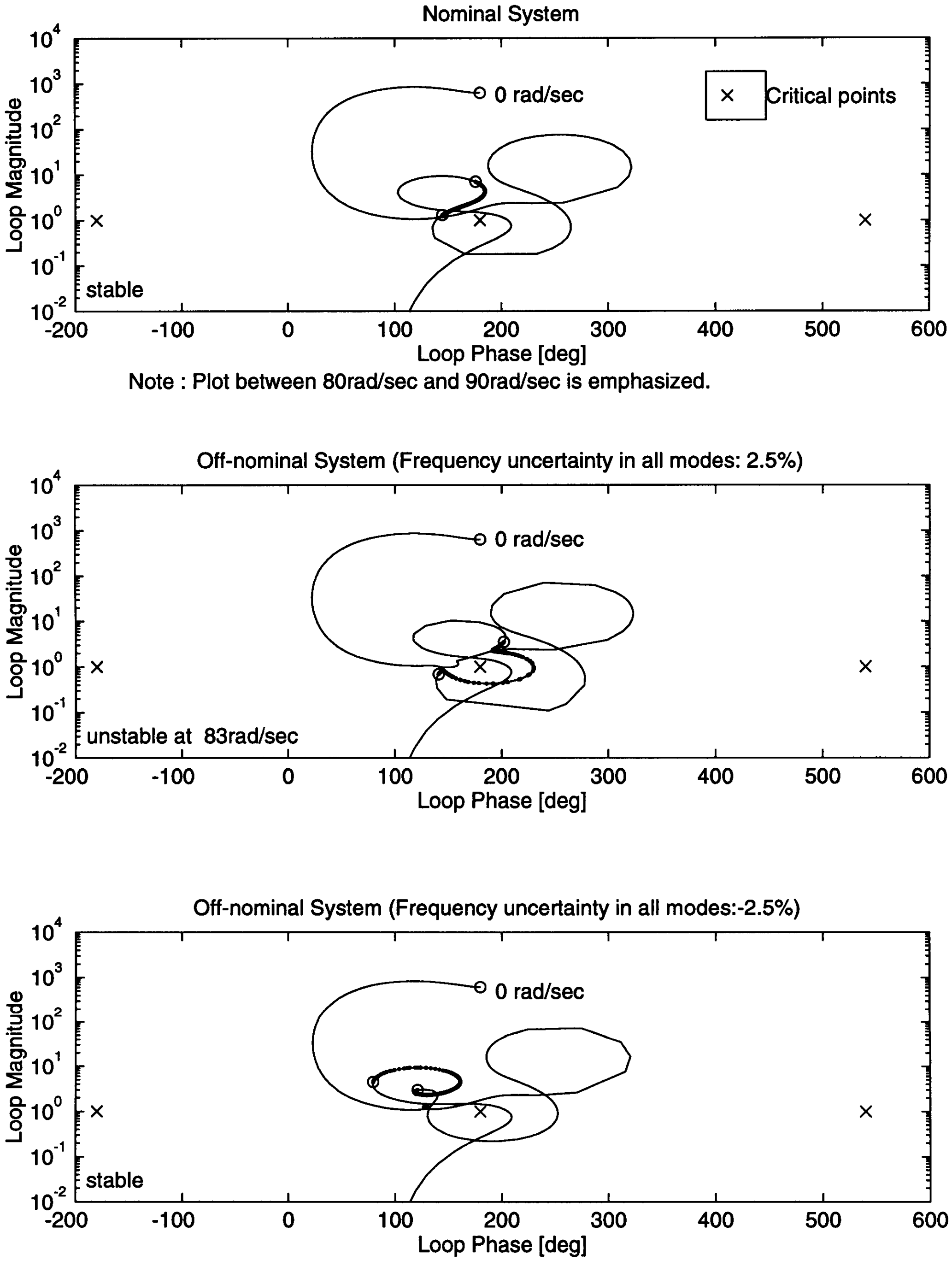

Note : Plot between 80rad/sec and 90rad/sec is emphasized.

Figure 4-10: Nichols plot : High authority LQG compensator and the plant system perturbed by frequency uncertainty

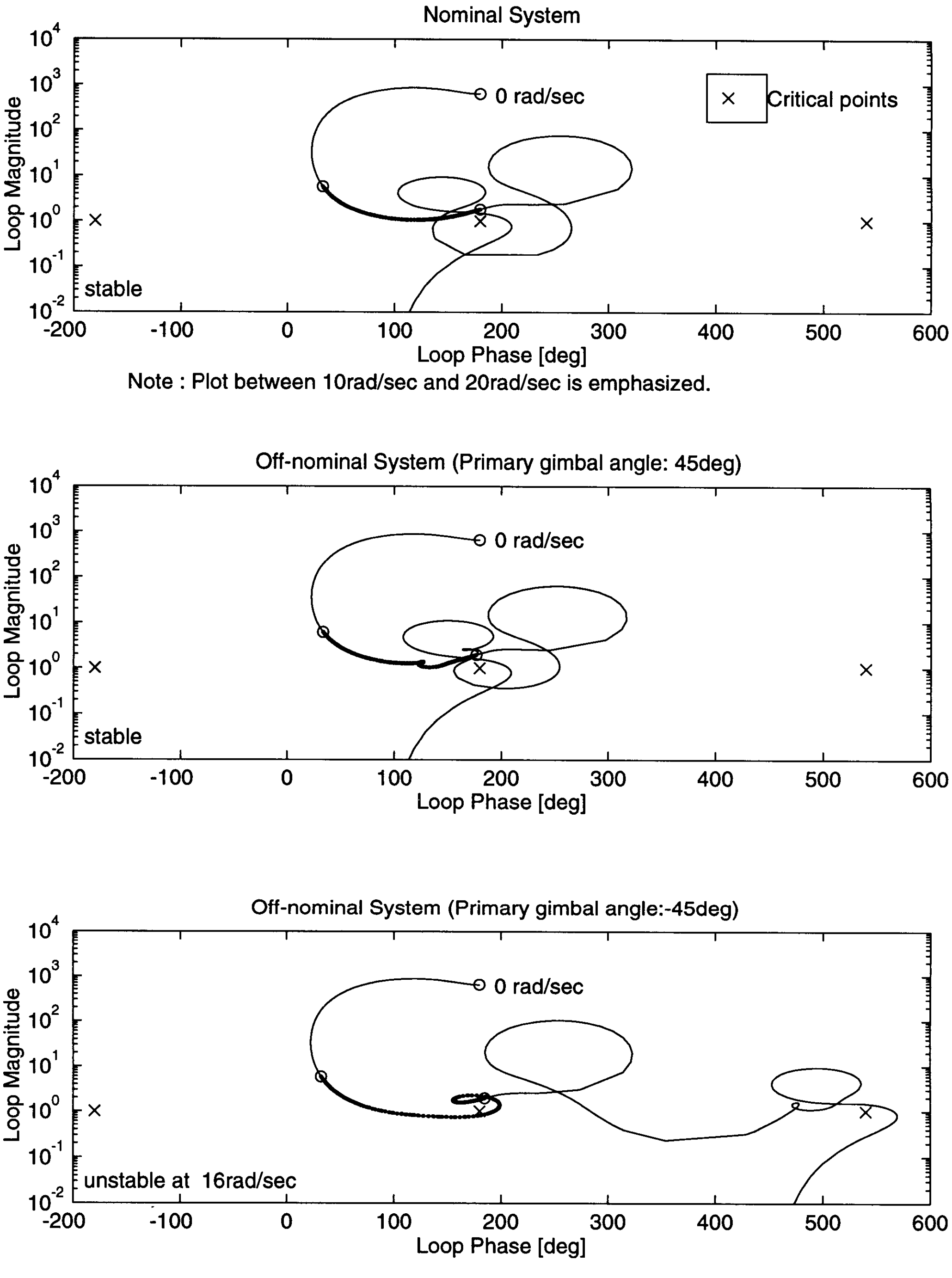

Note : Plot between 10rad/sec and 20rad/sec is emphasized.

Figure 4-11: Nichols plot : High authority LQG compensator and the plant system perturbed by primary gimbal average angle

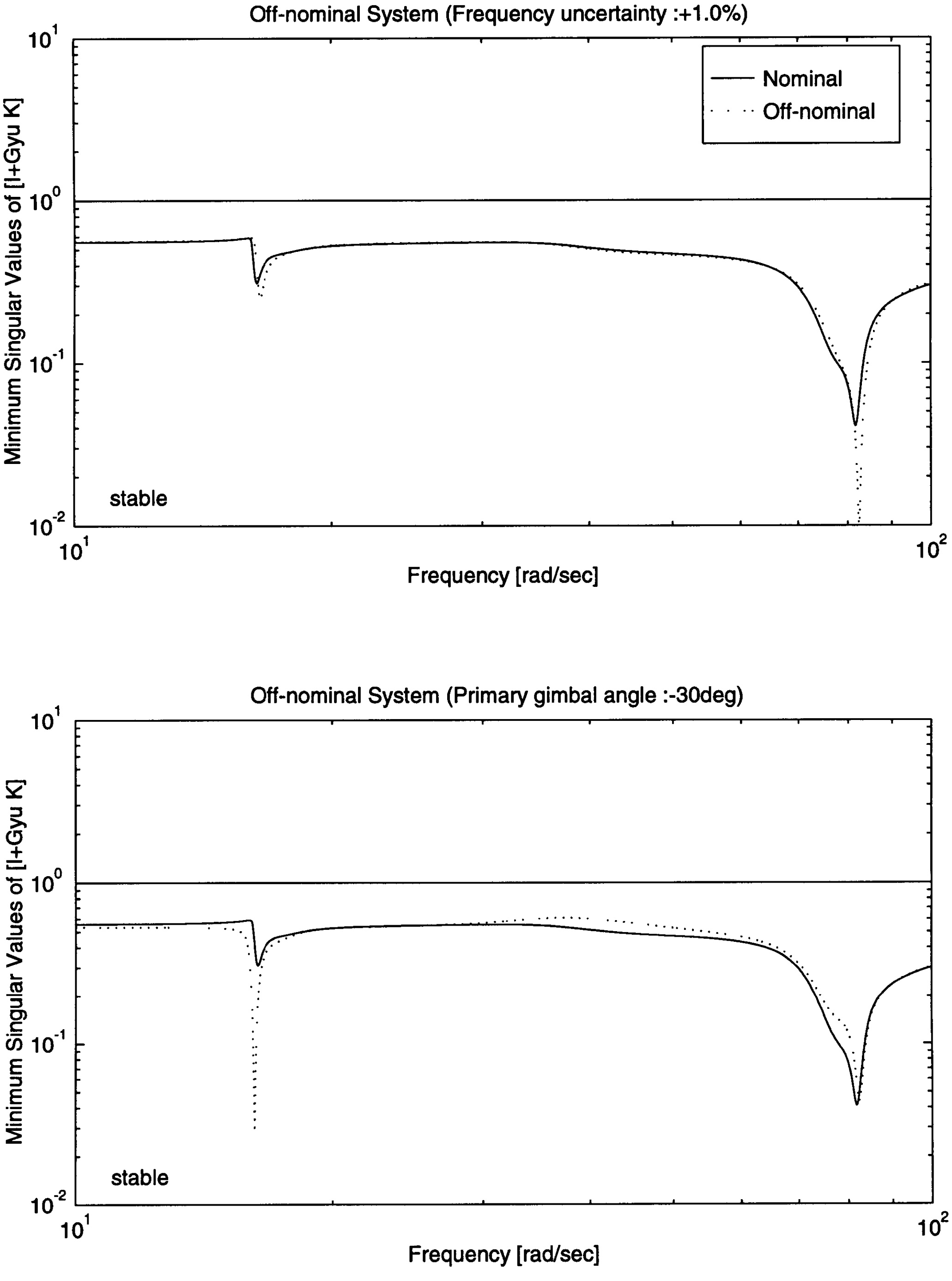

Figure 4-12: Sensitivity plot ($\underline{\sigma}[I + G_{yu}\,K]$) : High authority LQG compensator

4.3 MM Designs

As performed in the previous section, the LQG technique provides compensators for the MIMO plant system with ease. Although the LQG compensators have excellent nominal performance, their robustness for the off-nominal factors defined in the beginning of this chapter is poor and does not meet the design requirement. In this section, the LQG compensators are modified with the MM technique to satisfy the design requirement.

Since all targeted design points do not lie inside of the stable region of the LQG compensator, intermediate design points need to be set. As described in Section 4.1.2, the progressive method is applied in order to obtain FU-MM compensators at first which guarantee robust stability for frequency uncertainty in all Z-bending modes, and then FU&PG-MM compensators which guarantee both off-nominal factors.

The design results are summarized in Table 4.5. The same weights as the LQG designs are used for each level of control authority. The performance gain, which indicates a difference of the state cost between the open loop system and the closed loop system, is degraded in all MM compensators, However, the degradation is $1.2dB$ at worst in the high authority case. Although the difference of the nominal LQG cost between the LQG compensator and the FU&PG-MM compensator is more noticeable in the higher control authority case as shown in Figure 4-13, the loss of the nominal LQG cost is only 16% in the high authority case. Considering the improvement in robustness, this loss is a reasonable sacrifice.

In the following subsections, the MM designs in the low and high control authority cases are discussed and compared.

Table 4.5: Summary of the MM designs for the MIMO, 4-mode flexible MACE model

Design Case	Weights			Performance Gain	Nominal LQG Cost
	State C_z	Control D_{zu} ρ	Sensor Noise D_{yw} θ	$[dB]$	
Low LQG	1.0	3.50×10^{-3}	2.9875×10^{-3}	-37.685	4.863×10^{-2}
Low FU-MM	1.0	3.50×10^{-3}	2.9875×10^{-3}	-37.656	4.878×10^{-2}
Low FU&PG-MM	1.0	3.50×10^{-3}	2.9875×10^{-3}	-37.388	4.947×10^{-2}
Mid. LQG	1.0	1.00×10^{-3}	1.5169×10^{-3}	-42.040	2.936×10^{-2}
Mid. FU-MM	1.0	1.00×10^{-3}	1.5169×10^{-3}	-42.003	2.947×10^{-2}
Mid. FU&PG-MM	1.0	1.00×10^{-3}	1.5169×10^{-3}	-41.700	3.013×10^{-2}
High LQG	1.0	1.00×10^{-4}	3.5024×10^{-4}	-53.889	7.882×10^{-3}
High FU-MM	1.0	1.00×10^{-4}	3.5024×10^{-4}	-53.657	8.064×10^{-3}
High FU&PG-MM	1.0	1.00×10^{-4}	3.5024×10^{-4}	-52.672	9.147×10^{-3}

(Note) FU:±2.5% Frequency Uncertainty guarantee,
PG:±45deg Primary Gimbal average angle guarantee.

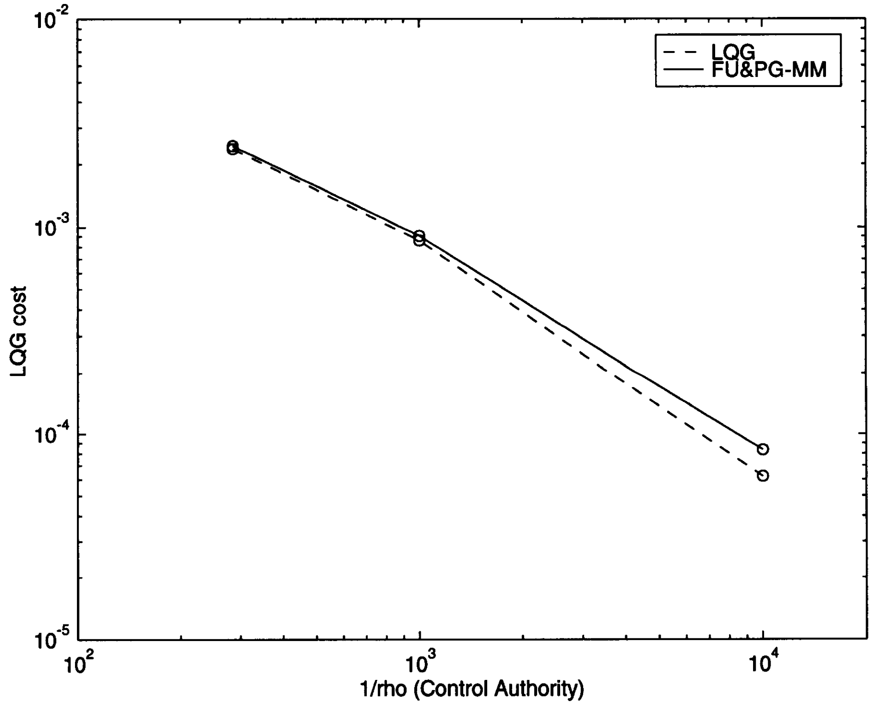

Figure 4-13: Changes of the nominal LQG cost as a function of the control authority

4.3.1 Low Authority MM Compensators

The low authority FU&PG-MM compensator is found by modifying the low authority LQG compensator. The FU-MM compensator is obtained as an intermediate compensator to guarantee robust stability for frequency uncertainty.

The singular values of those MM compensators are plotted in Figure 4-14 with the singular values of the low authority LQG compensator. Two differences between the FU&PG-MM compensator and the other compensators are identified: the maximum singular values of the FU&PG-MM compensator below $10rad/sec$ are lower than those of the others by $5dB$; the FU&PG-MM compensator has a tall peak at $16rad/sec$, which corresponds to the frequency of the first bending mode. The latter difference is meaningful, because the off-nominal factor of primary gimbal average angle, which is dealt with in the FU&PG-MM design, mainly influences the first bending mode of the plant system as discussed in Section 4.1.1.

As illustrated in Figure 4-15, the performance of the FU&PG-MM compensator around $16rad/sec$ is improved, while the performance below $10rad/sec$ is degraded by $5dB$. Because of the performance improvement above $100rad/sec$, the performance gain decreases by only $0.3dB$ between the original LQG compensator and the FU&PG-MM compensator as listed in Table 4.5.

The stability boundaries of the MM compensators are listed in Table 4.6. Both low authority FU-MM and FU&PG-MM compensators satisfy the design requirement of robust stability. The achieved stability boundaries for both low authority MM compensators significantly exceed the targeted off-nominal design points, ±2.5% fre-

Table 4.6: Stability boundaries of the low authority MM compensators

Design Case	Frequency Uncertainty [%]		Primary Gimbal Angle [deg]	
	lower	upper	lower	upper
Low LQG	−2.40	4.80	−42.0	> 60.0
Low FU-MM	−5.60	10.80	< −60.0	> 60.0
Low FU&PG-MM	−13.60	12.40	< −60.0	> 60.0

(Note) FU:±2.5% Frequency Uncertainty guarantee,
PG:±45deg Primary Gimbal average angle guarantee.

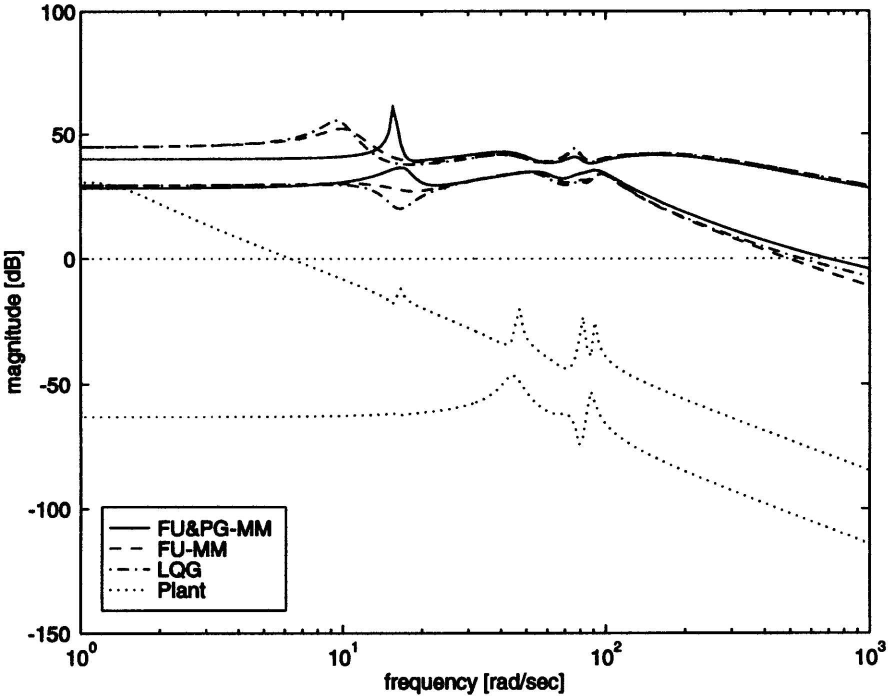

Figure 4-14: Singular value plots of the low authority MM compensators and the plant system

quency uncertainty and ±45deg primary gimbal average angle. The stability boundary of the FU-MM compensator for the frequency uncertainty is two times as large as the targeted. This conservatism becomes larger in the FU&PG-MM compensator; the FU&PG-MM's stability boundary for the frequency uncertainty is four times as large as the targeted. These can be observed in the LQG cost plots as a function of the frequency uncertainty in all modes or the primary gimbal angle in Figure 4-16. The plots show that both low authority MM compensators provide high robust performance for both targeted off-nominal points as well as robust stability.

This conservatism can be reduced by decreasing the cost weights, β_i, on the off-nominal design points. In this design case, however, the extreme robustness of the FU&PG-MM compensator is obtained with only 2% nominal performance loss. Therefore, taking the small loss of nominal performance into consideration, this conservatism is not a serious problem. This indicates that the effectiveness of the MM technique.

Another interesting feature in Figure 4-16 is that the LQG cost of the off-nominal

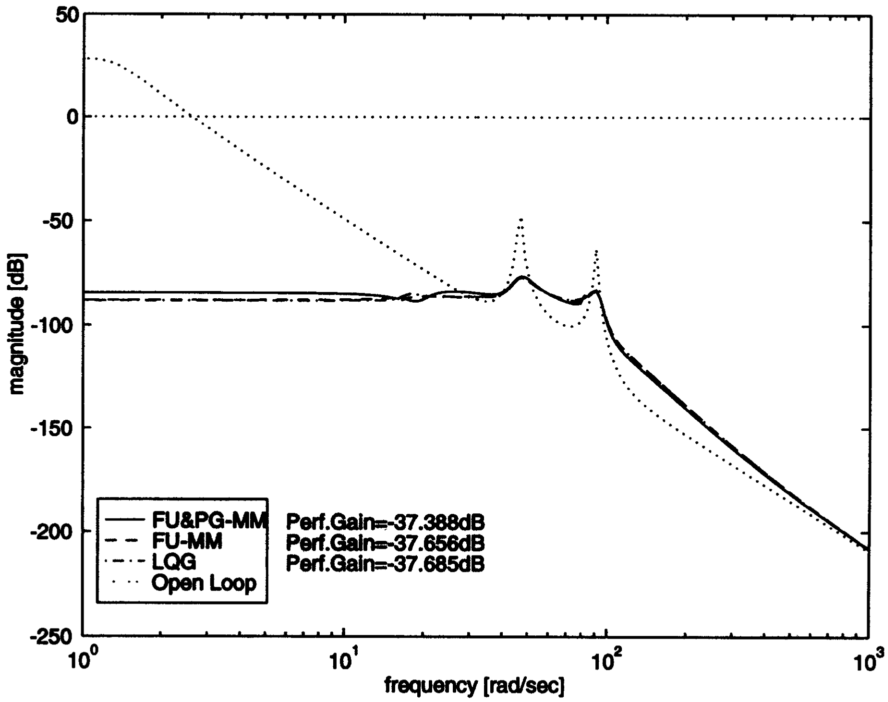

Figure 4-15: Performance of the low authority MM compensators

system with large primary gimbal average angle is lower than the nominal LQG cost. This implies that the plant system with these particular primary gimbal configurations is easier to be controlled than the nominal configuration.

The LQG costs illustrated in Figure 4-17 implies that the stable region of the low authority FU-MM compensator is significantly expanded in both the direction of frequency uncertainty and primary gimbal angle, in contrast with the plot of the low authority LQG compensator shown in Figure 4-7. Although the FU-MM compensator was not designed with consideration of the second off-nominal factor, *i.e.* the primary gimbal average angle, all four targeted off-nominal design points come inside of the stable region. The performance degradation at all off-nominal design points is below 20%. The requirement established at the beginning of this design is satisfied with the FU-MM compensator. As shown in Figure 4-18, however, by performing the next MM design step to obtain the FU&PG-MM compensator, the robust performance with respect to the primary gimbal average angle is greatly improved with only 2% loss in nominal performance. The regions in which the normalized LQG cost is below one can be found along the 0% frequency uncertainty line. Two off-nominal design points for the primary gimbal average angle are located in these regions.

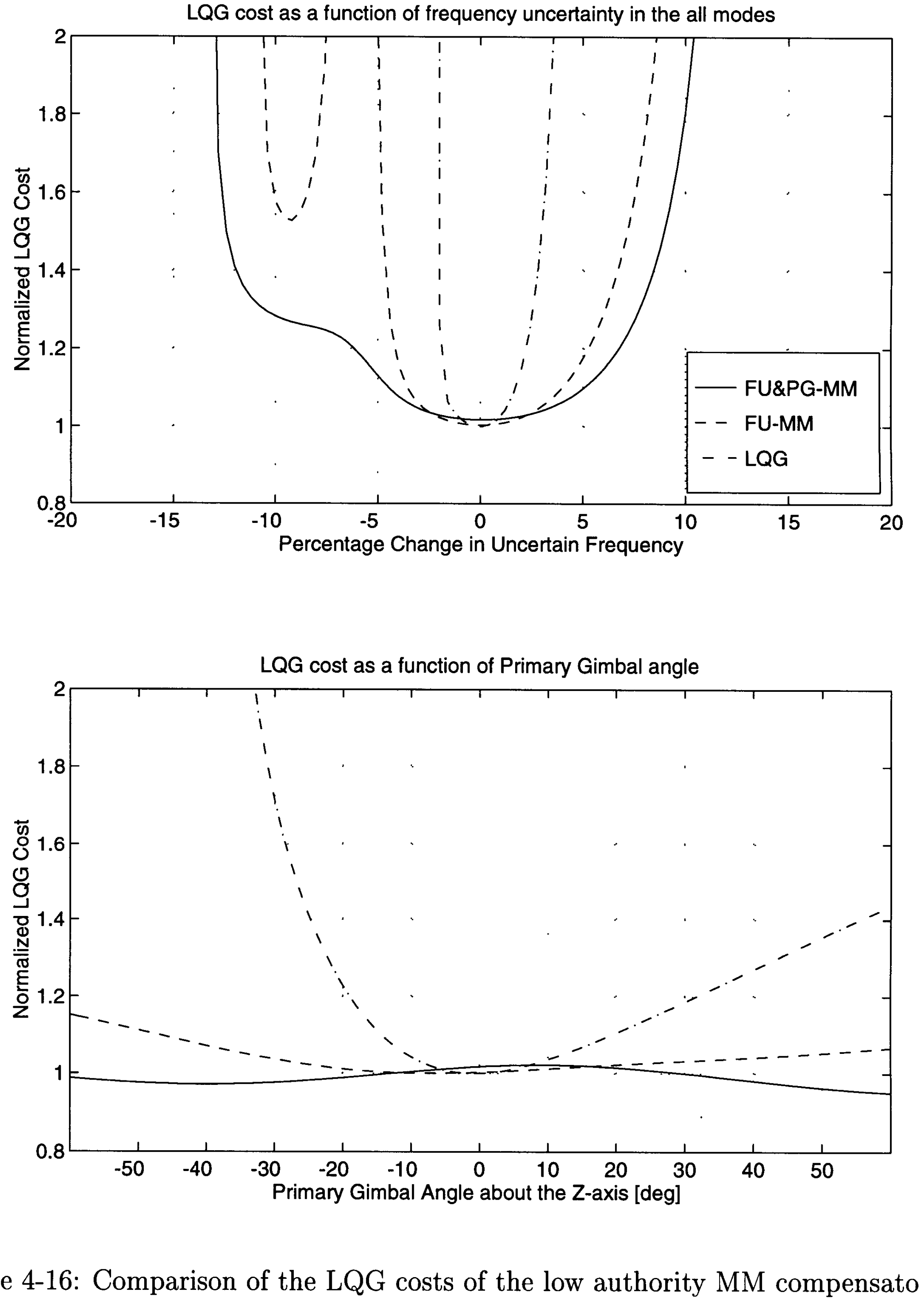

Figure 4-16: Comparison of the LQG costs of the low authority MM compensators

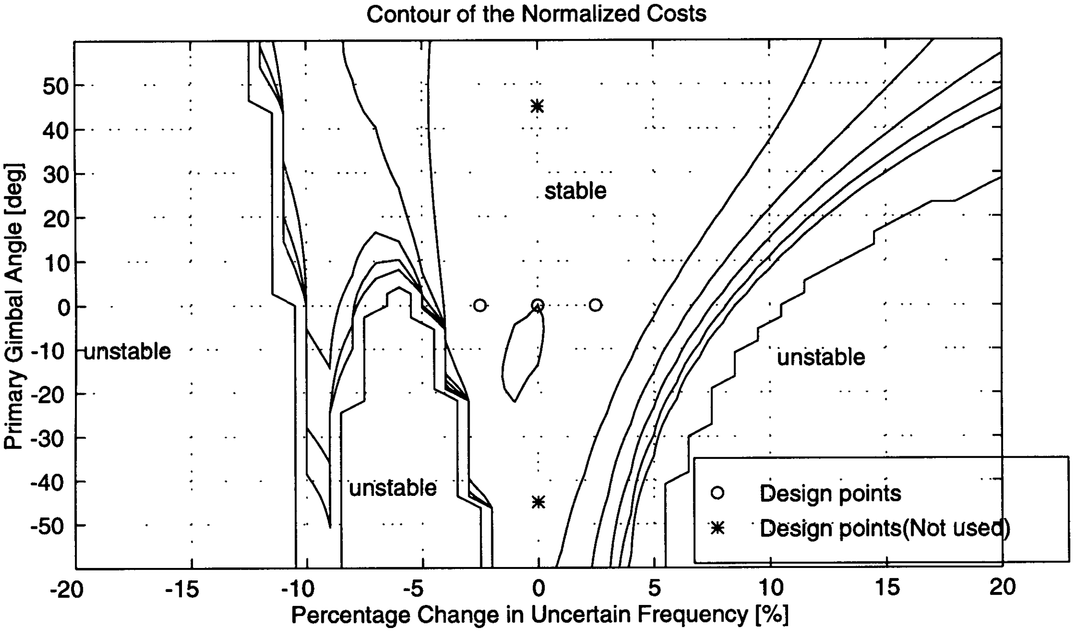

Note:Contours(From 1.0 to 2.0 with increments of 0.2)
The outermost contour is the boundary of the stable region.
Nominal LQG Cost=4.878e-02

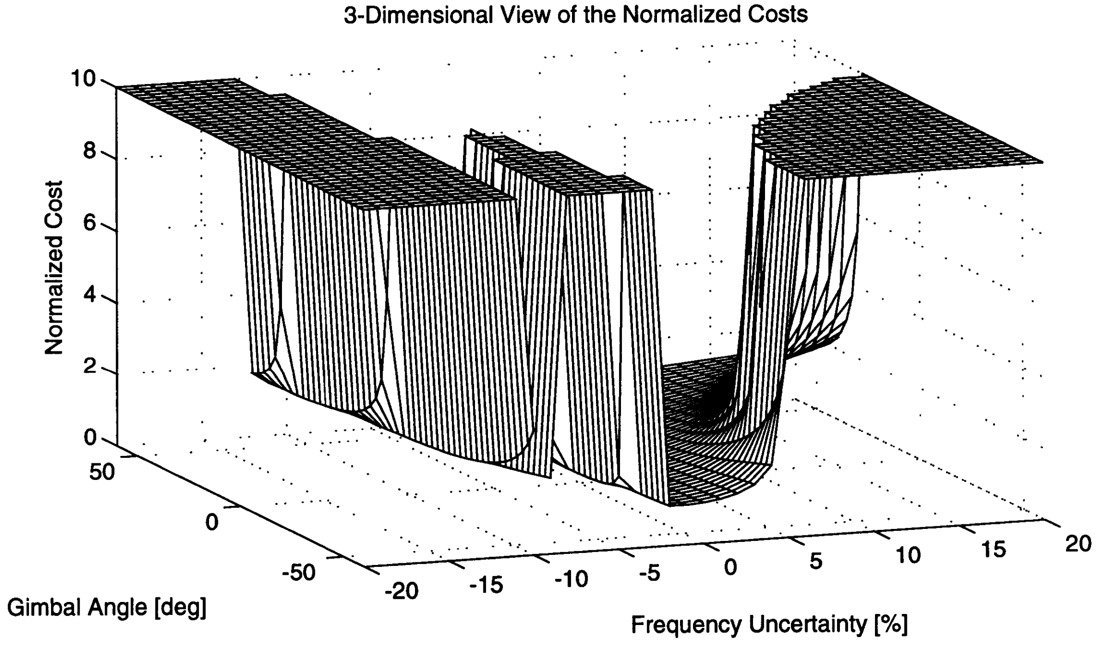

Figure 4-17: LQG cost of the closed loop system with the low authority FU-MM compensator

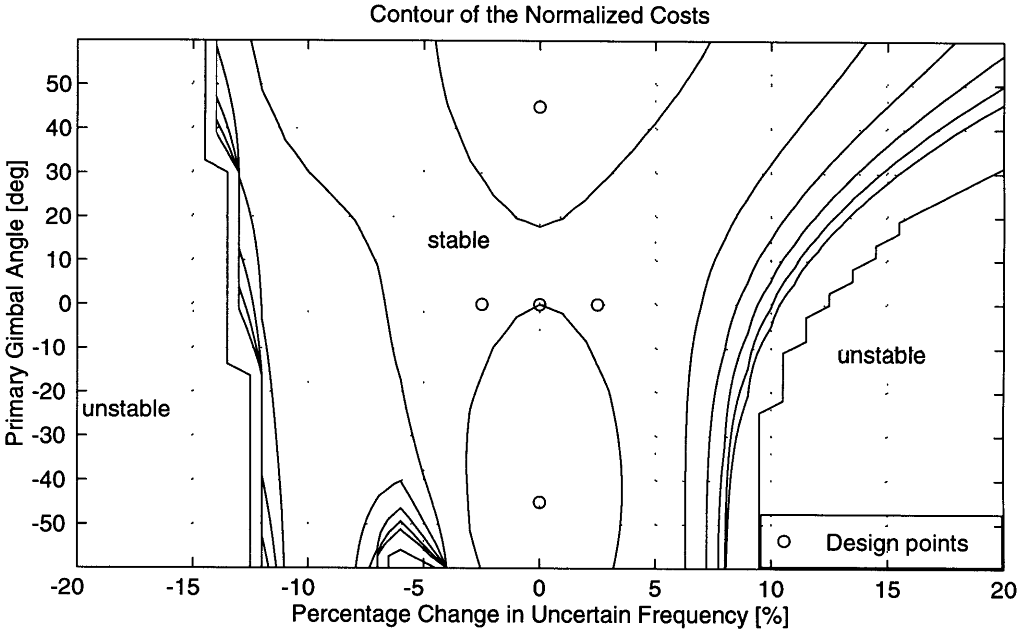
Contour of the Normalized Costs

Note:Contours(From 1.0 to 2.0 with increments of 0.2)
The outermost contour is the boundary of the stable region.
Nominal LQG Cost=4.947e-02

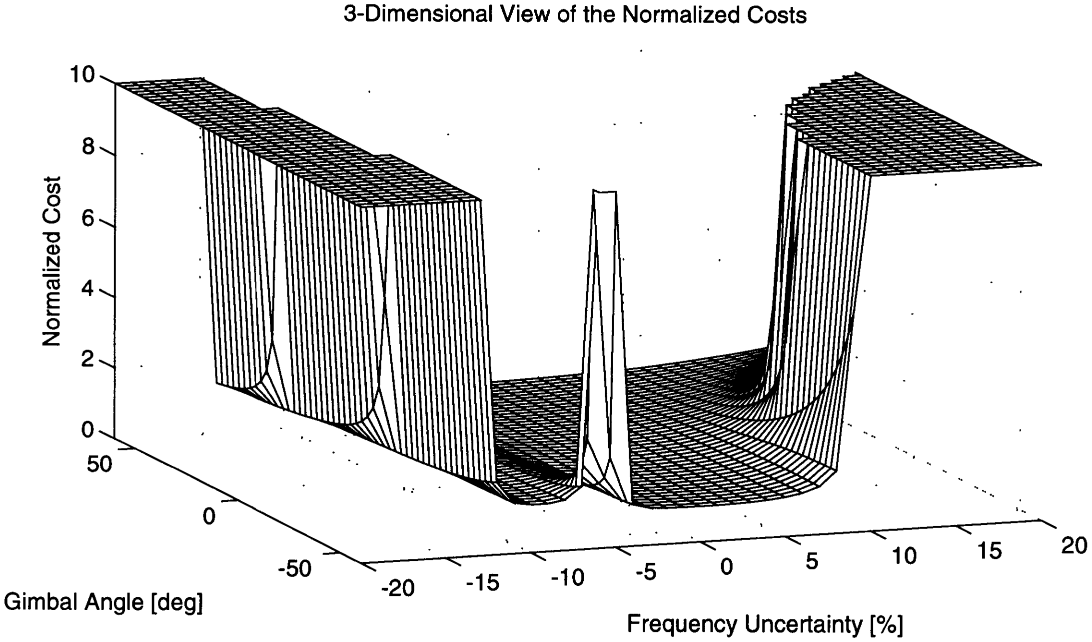
3-Dimensional View of the Normalized Costs

Figure 4-18: LQG cost of the closed loop system with the low authority FU&PG-MM compensator

4.3.2 High Authority MM Compensators

In the higher control authority case, the high authority LQG compensator obtained in Section 4.2 is modified to guarantee the stability robustness for the two off-nominal factors. The singular values of the resulting MM compensators are plotted in Figure 4-19. A tall peak appears at $78 rad/sec$ in the plot of the FU-MM compensator and moves to $84 rad/sec$ in the plot of the FU&PG-MM compensator. This frequency region corresponds to the frequency of the third nominal Z-bending mode, $81.8 rad/sec$. Another noticeable feature in the singular value plots is that the FU&PG-MM's maximum singular values around $17 rad/sec$ are kept low, while the values at other frequencies become higher. This frequency region corresponds to the frequency, $16.3 rad/sec$, of the first nominal Z-bending mode, which is dominantly influenced by the primary gimbal average angle

The performance plot of the FU-MM compensator in Figure 4-20 is not greatly different from that of the original high authority LQG compensator. This results in only $0.23 dB$ loss of nominal performance over the LQG compensator. On the other hand, significant performance degradation can be recognized in the FU&PG-MM's performance plot, while the FU&PG-MM compensator has better performance above $230 rad/sec$. This results in $1.2 dB$ loss of nominal performance over the LQG compensator.

In the same way in the low authority case, the stability boundaries listed in Table 4.7 imply that the high authority FU-MM compensator satisfies the design requirement of robust stability. The achieved stability boundary of the FU-MM com-

Table 4.7: Stability boundaries of the high authority MM compensators

Design Case	Frequency Uncertainty [%]		Primary Gimbal Angle [*deg*]	
	lower	upper	lower	upper
High LQG	−18.80	1.60	−33.6	> 60.0
High FU-MM	< −20.00	5.60	< −60.0	> 60.0
High FU&PG-MM	< −20.00	6.40	< −60.0	> 60.0

(Note) FU:±2.5% Frequency Uncertainty guarantee,
PG:±45*deg* Primary Gimbal average angle guarantee.

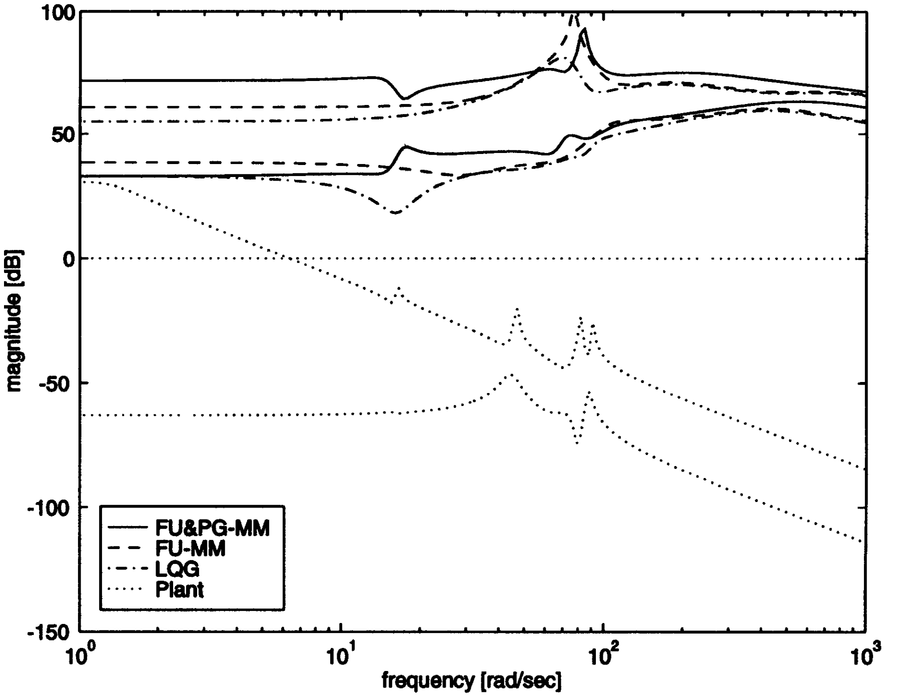

Figure 4-19: Singular value plots of the high authority MM compensators and the plant system

pensator for the frequency uncertainty is two times as large as the targeted boundary, 2.5%. This stability boundary is kept in the high authority FU&PG-MM compensator, while conservatism extremely becomes large in the low control authority design case.

The LQG cost plots in Figure 4-21 indicate that the FU-MM compensator is obtained with only 2.3% loss of nominal performance. Although robust performance of the FU-MM compensator is significantly improved in comparison with that of the original LQG compensator, the normalized LQG costs for the off-nominal deign points of ±45*deg* primary gimbal average angles are above two. This means that performance degradation is more than 100%. Robust performance for the primary gimbal average angle needs to be improved.

As a result of 16% nominal performance loss, the FU&PG-MM compensator obtains significant improvement of robust performance for the primary gimbal average angle shown in Figure 4-21. Since the nominal performance of the high authority LQG compensator is six times as high as that of the low authority compensator as

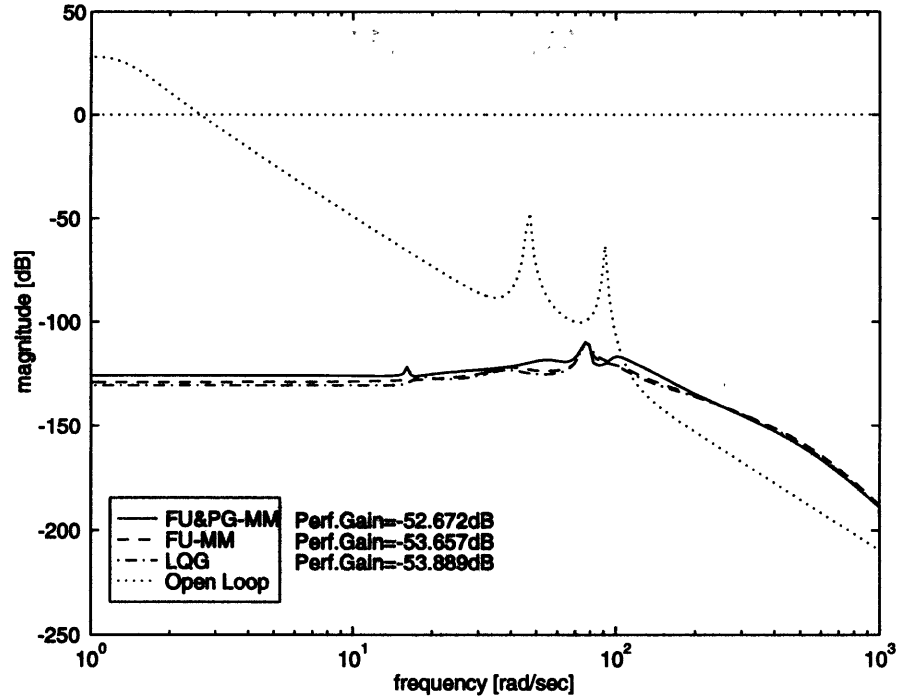

Figure 4-20: Performance of the high authority MM compensators

shown in Figure 4-6, this 16% nominal performance loss is a reasonable sacrifice. The MM technique provides a high performance compensator which satisfies the design requirement.

These improvements of robustness can be clearly recognized in the LQG cost plots in Figures 4-22 and 4-23. In comparison with the plot of the high authority LQG compensator in Figure 4-9, the performance robust region around the nominal design point is substantially expanded. Note that *performance robust region* indicates a region where performance is insensitive to off-nominal parameter variations. In particular, the FU&PG-MM compensator can be expected to operate in the desired off-nominal region with less than 20% performance degradation. This degraded performance for off-nominal conditions is still 4.5 times as high as performance of the low authority compensators.

The Nichols plots in Figures 4-24 and 4-25 also show that the robust stability requirement is achieved with the high authority FU&PG-MM compensator. Notice that the FU&PG-MM compensator has two sets of unstable poles, while the plant system only has stable poles. The plots in the regions from $10 rad/sec$ to $20 rad/sec$ and $80 rad/sec$ to $90 rad/sec$ lie farther from the critical points than those of the original high authority LQG compensator in Figures 4-10 and 4-11. The off-nominal closed loop systems of the original LQG compensator have unstable poles in those frequency regions.

Finally, the sensitivity plots, $\underline{\sigma}[I + G_{yu}(j\omega)\,K(j\omega)]$, are shown in Figure 4-26 with the off-nominal plots for $+1.0\%$ frequency uncertainty and $-30 deg$ primary gimbal angle. The differences between the nominal plots and the off-nominal plots are small, while large differences are identified in the high authority LQG compensator in Figure 4-12. This implies that the closed loop system of the high authority compensator is desensitized to both off-nominal factors.

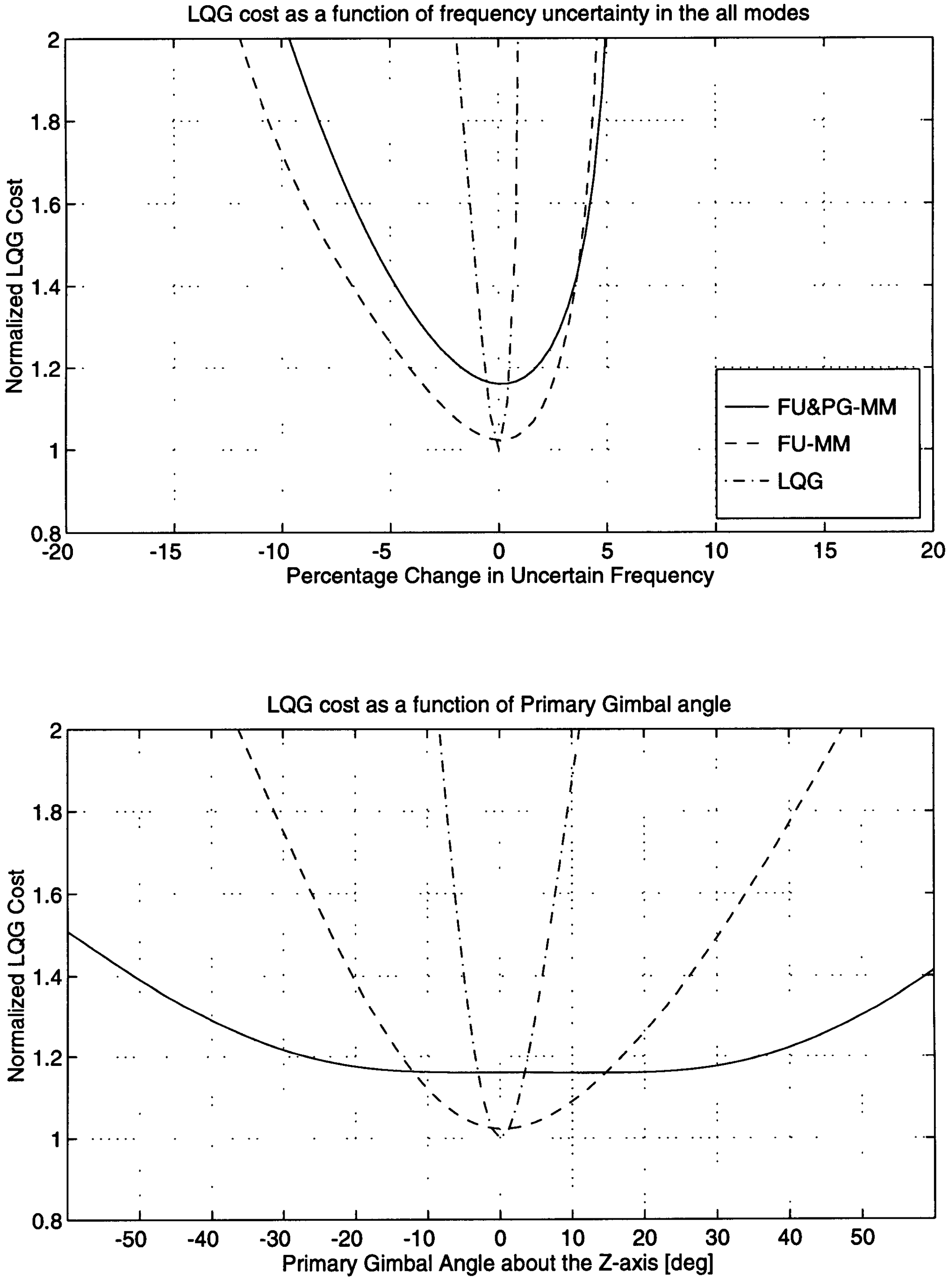

Figure 4-21: Comparison of the LQG costs of the high authority MM compensators

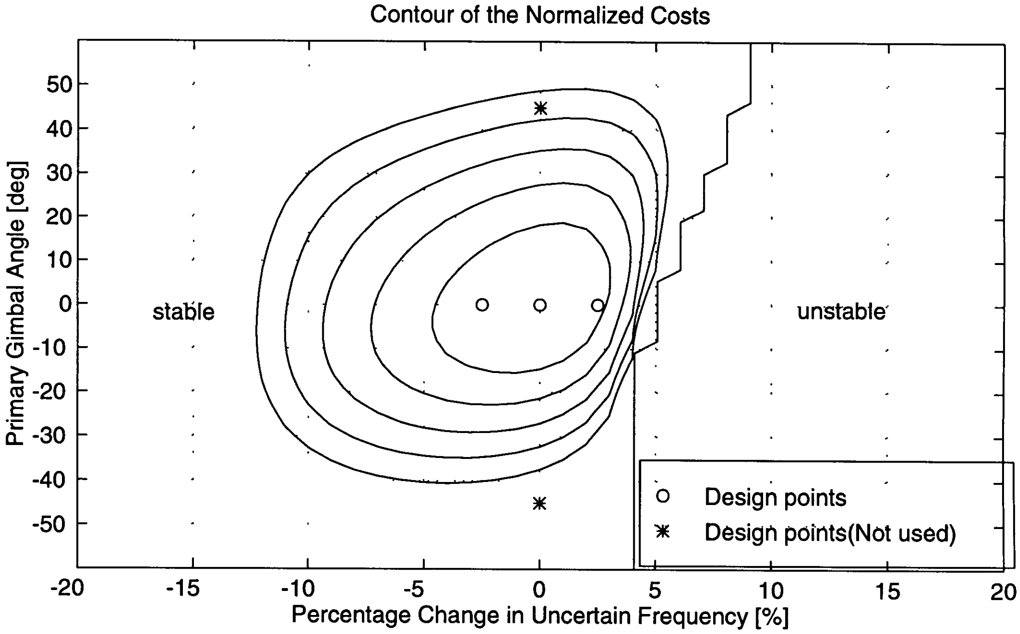
Contour of the Normalized Costs

Note:Contours(From 1.2 to 2.0 with increments of 0.2)
The outermost contour is the boundary of the stable region.
Nominal LQG Cost=8.064e-03

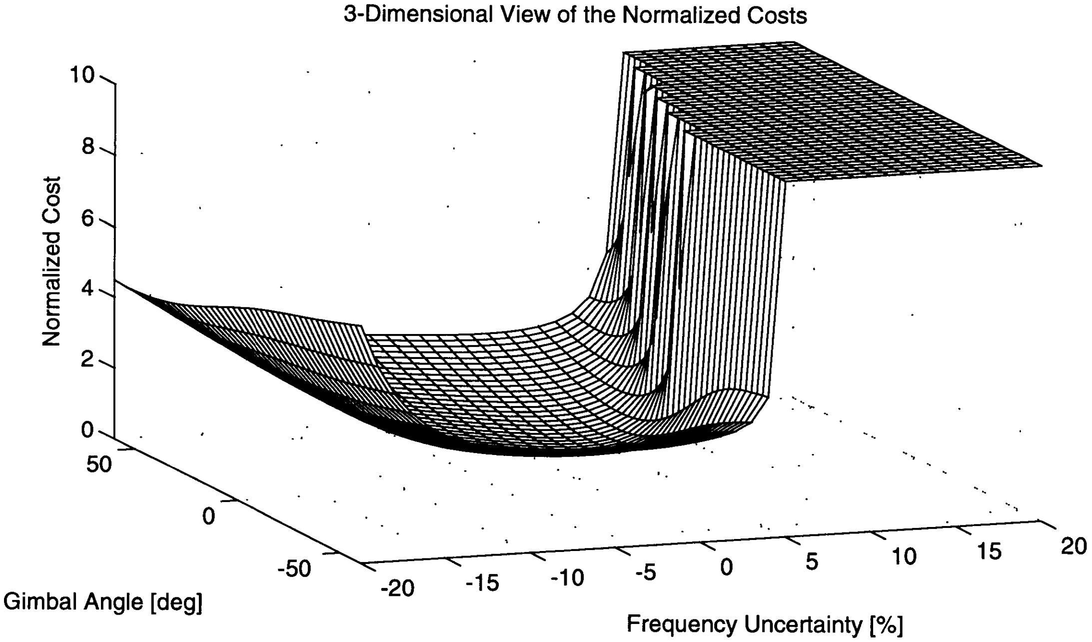
3-Dimensional View of the Normalized Costs

Figure 4-22: LQG cost of the closed loop system with the high authority FU-MM compensator

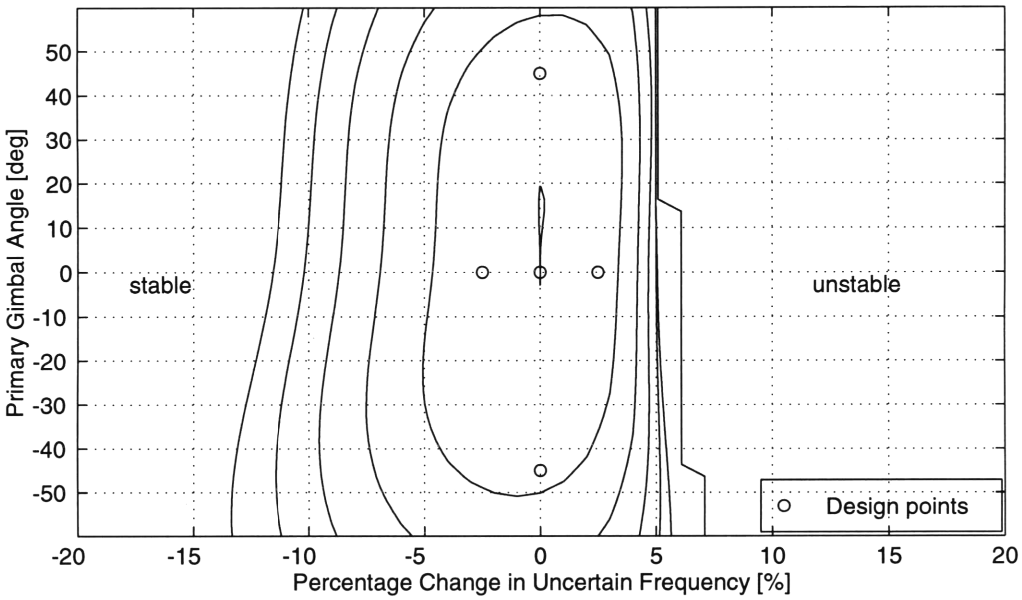

Contour of the Normalized Costs

Note:Contours(From 1.0 to 2.0 with increments of 0.2)
The outermost contour is the boundary of the stable region.
Nominal LQG Cost=9.147e-03

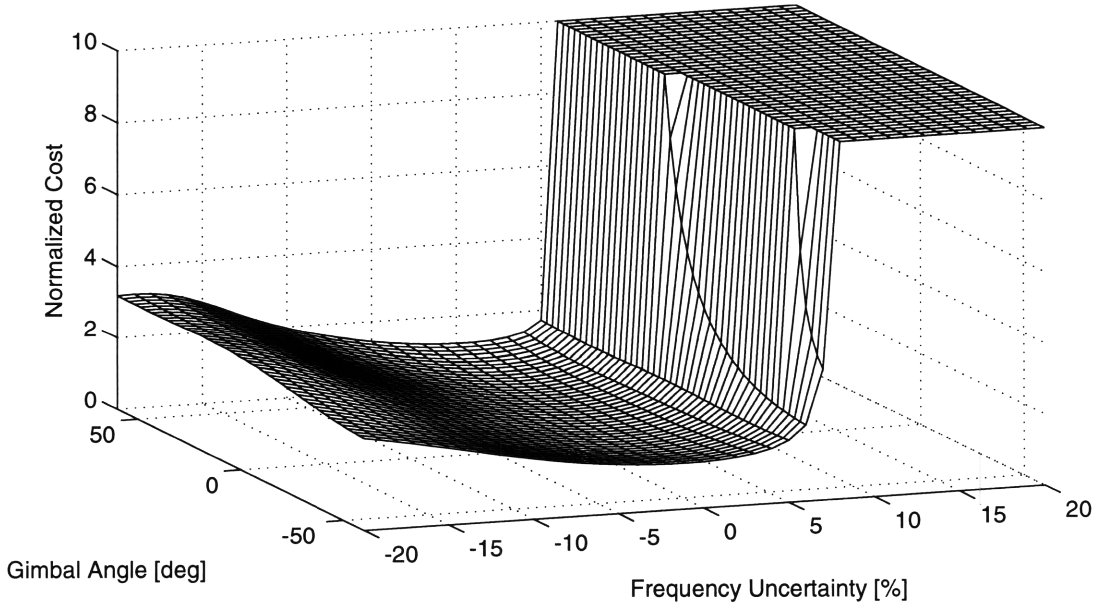

3-Dimensional View of the Normalized Costs

Figure 4-23: LQG cost of the closed loop system with the high authority FU&PG-MM compensator

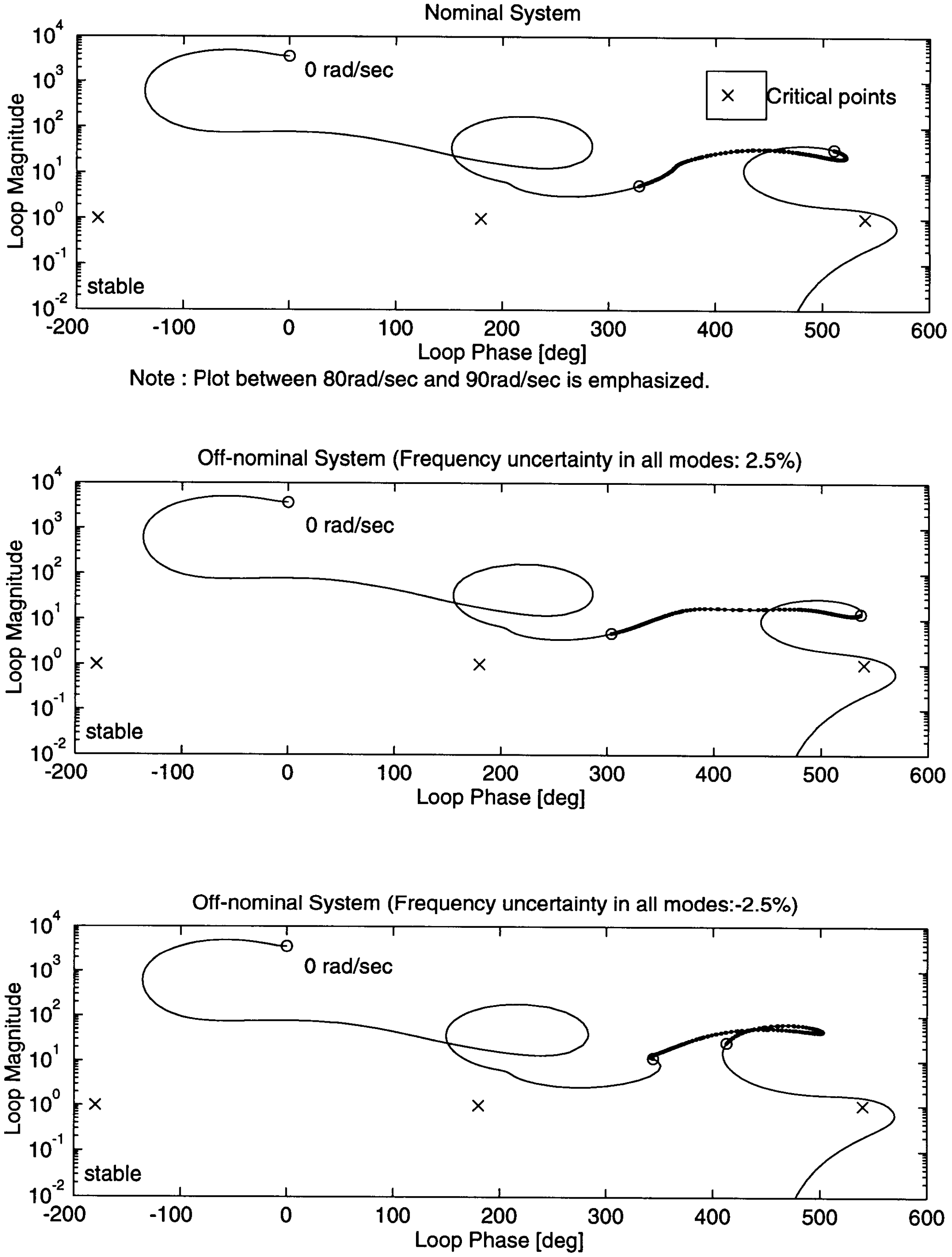

Note : Plot between 80rad/sec and 90rad/sec is emphasized.

Figure 4-24: Nichols plot : High authority FU&PG-MM compensator and the plant system perturbed by frequency uncertainty

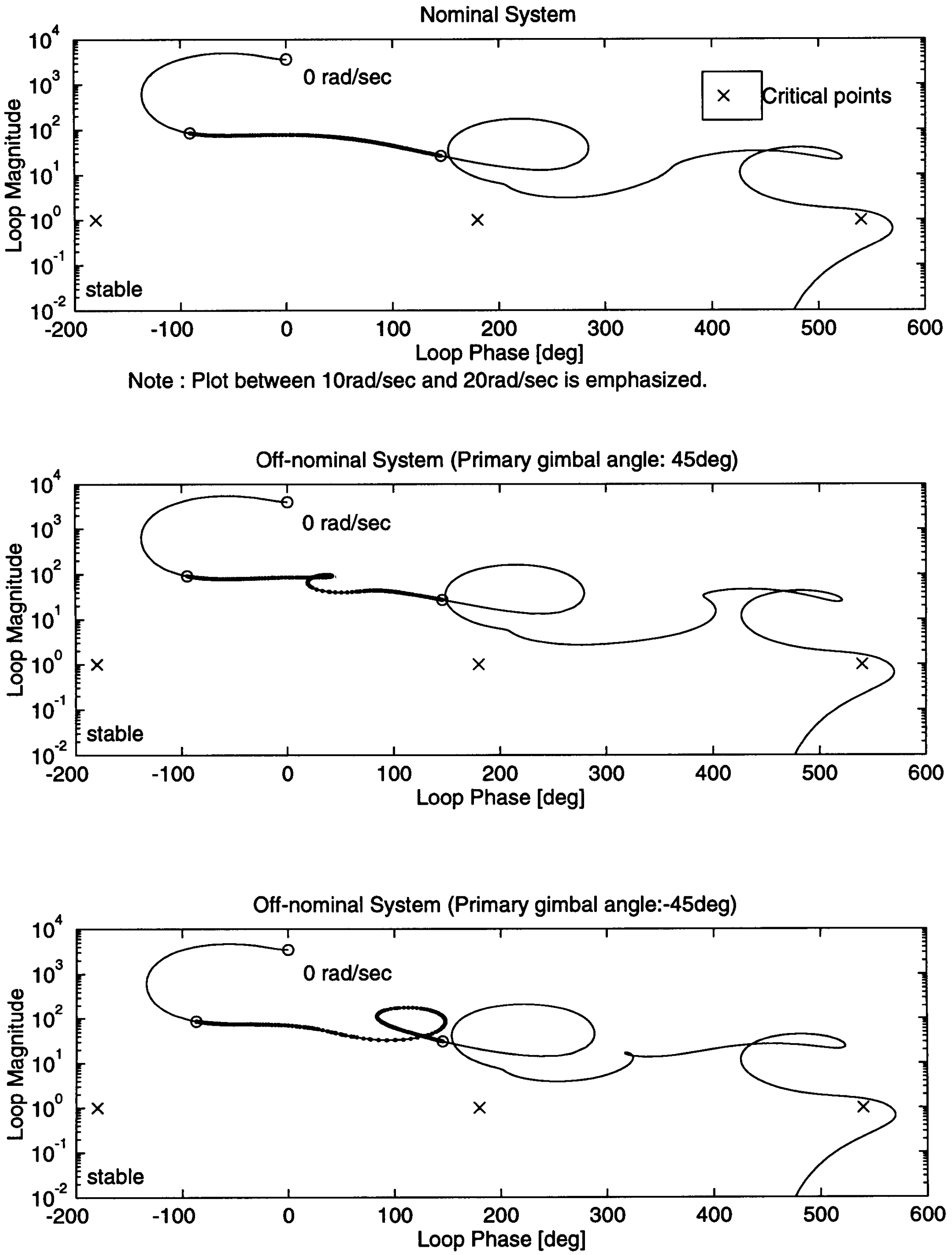

Nominal System

Note : Plot between 10rad/sec and 20rad/sec is emphasized.

Off-nominal System (Primary gimbal angle: 45deg)

Off-nominal System (Primary gimbal angle:-45deg)

Figure 4-25: Nichols plot : High authority FU&PG-MM compensator and the plant system perturbed by primary gimbal average angle

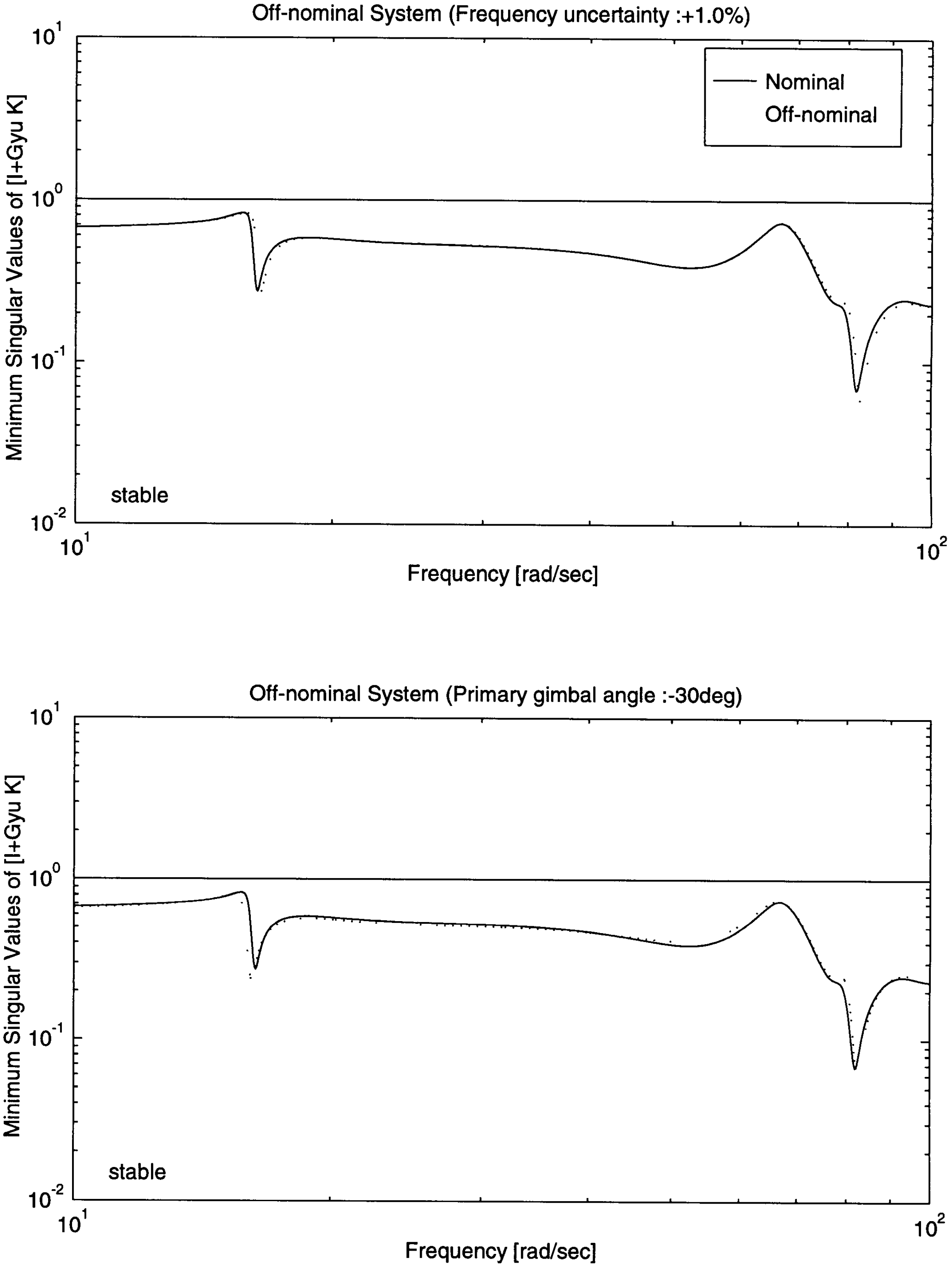

Figure 4-26: Sensitivity plot ($\underline{\sigma}[I + G_{yu} K]$) : High authority FU&PG-MM compensator

4.4 Conclusions

Three design series based on control authority were performed, and they provided the robust compensators which guaranteed stability for the two off-nominal factors; $\pm 2.5\%$ frequency uncertainty in all Z-bending modes and $\pm 45deg$ primary gimbal average angle. The MM technique was shown to be effective at stabilizing the plant under the nonlinear inertia change associated with different gimbal average angles.

While the FU-MM compensators are obtained as an intermediate compensator with less than 2% nominal LQG cost increase, the FU&PG-MM compensators are obtained with at most 16% nominal LQG cost increase. The higher the control authority, the greater the loss in nominal performance between the LQG and MM designs.

The off-nominal factor in the first step of the MM designs is the frequency uncertainty in all Z-bending modes. In all three design cases, the resulting FU-MM compensators provide robust stability not only for the frequency uncertainty but also for the off-nominal primary gimbal average angle. This is because any off-nominal factors result in changes of the pole-zero structure of the plant system. As demonstrated in this chapter, however, if another off-nominal factor in addition to the frequency uncertainty in all modes is considered in the MM design, the MM technique effectively improves robustness for the additional off-nominal factor.

However, control designers have to keep in mind the drawback of the MM technique, the large amount of calculation load. An increase in the number of off-nominal factors in the MM design directly leads to an increase in calculation load. The most important consideration in robust control design is to understand which off-nominal factors are important to include in the design process.

Chapter 5

Conclusions

Three sets of control designs are performed with the Multiple Model (MM) technique: the sample designs; the SISO designs for the MACE test article; and the MIMO designs for the MACE test article.

The sample designs in Chapter 2 reveal the destabilization mechanism of control systems for lightly damped structural plants as well as the effectiveness on the MM technique. The destabilization deeply relates to the destruction of pole-zero structure of a plant and a compensator.

The SISO designs for the MACE test article in Chapter 3 imply that the MM technique effectively enhances robust stability and performance of compensators for two off-nominal factors: frequency uncertainty in the second Z-axis bending mode and primary gimbal average angle.

In the MIMO designs for the MACE test article in Chapter 4, presented as a realistic design case, the MM technique also demonstrates its effectiveness. Three design series using different control authorities are performed. In all design series, the FU-MM compensators, which guarantee stability under frequency uncertainty in all Z-axis bending modes, provide robust stability not only for frequency uncertainty but also for the other off-nominal factor, primary gimbal average angle. This is because any off-nominal factors result in changes of the pole-zero structure of a plant system. However, when the second off-nominal factor, *i.e.* primary gimbal average angle, is considered in the MM designs, the MM compensators provide excellent robust performance for this particular off-nominal factor. In the highest control authority case, the MM compensator keeps performance degradation within the designated off-nominal region to less than 20%, while the original LQG compensator cannot provide stability for all off-nominal design points. The MM compensator is obtained with 16% nominal performance loss in comparison with that of the original high authority LQG compensator. This nominal performance loss is reasonably small in comparison with that of the low authority LQG compensator, which provides the closest stable region to the design requirements. The nominal performance of the resulting high authority MM compensator is still 5.3 times as high as that of the low authority LQG compensator.

However, two main drawbacks in the MM technique need to be recognized: computational drawback and robust stability for an intermediate off-nominal point between specified design points. The computational drawback is divided into two problems: high computational load and the local minimum problem. Both problems originate in the numerical multivariable optimization used in the MM design. To obtain higher performance compensator, the local minimum problem is more serious. This problem is general in numerical optimization methods; nobody can prove that a minimum point obtained by numerical optimization methods is not a local minimum point but a global minimum point.

To avoid obtaining local minima, the MM technique requires an appropriate initial design which is close to the ultimate design. However, the process of obtaining the appropriate initial design can be an extensive robust control design because the initial design must be stable for all design points including targeted off-nominal design points. Therefore, although several MM design steps need to be performed, the progressive technique which is used in the MM designs in this research can be one of the measures to heighten a possibility of obtaining a global minimum solution. In the progressive technique, an LQG optimal solution is used as an initial design, and off-nominal design points are progressively moved from the nominal point to targeted off-nominal design points. Increases of the nominal LQG cost need to be monitored as shown in the SISO designs in Chapter 3.

In all MM design problems in this study, MM compensators are successfully obtained, and they provide robust stability for the appropriate off-nominal region which includes all the specified design points. Although the MM technique guarantees stability for all the specified design points, it does not guarantee an intermediate off-nominal point between the specified design points. This means that a stable region provided by the MM technique can be broken between specified design points, if off-nominal design points are improperly selected and/or cost weights, β_i, on design points are inappropriately set in a MM design. Therefore, it is necessary to perform a stability test, such as the LQG cost plot used in this study, to confirm stability of a resulting compensator for a desired off-nominal region.

This study proves the effectiveness of the MM technique for designing control for space structure systems which have multiple, real-parametric off-nominal factors including nonlinear inertia properties. Although the MM technique has the drawbacks discussed above, it is a practical robust control design technique. In aerospace engineering, the MM technique is applicable to many design problems with nonlinear properties such as a reentry attitude control design for a space shuttle.

Appendix A

Derivatives of the Weighted Sum of the LQG costs in the MM Method

This appendix presents the derivations of the partial derivatives of the weighted sum of the LQG costs used in the Multiple Model (MM) technique.

The weighted sum of the LQG costs with the constraint for stability is given by

$$J_a = \sum_{i=1}^{n_{DP}} \beta_i \, trace \left[\tilde{C}_i \tilde{Q}_i \tilde{C}_i^T + \tilde{P}_i \left(\tilde{A}_i \tilde{Q}_i + \tilde{Q}_i \tilde{A}_i^T + \tilde{B}_i \tilde{B}_i^T \right) \right], \tag{A.1}$$

where $\tilde{P}_i$ are the Lagrange multipliers, and the augmented system matrices are defined as follows:

$$\begin{aligned}
\tilde{A}_i &= \begin{bmatrix} A_i & -B_{u_i} C_c \\ B_c C_{y_i} & A_c - B_c D_{yu_i} C_c \end{bmatrix} = \begin{bmatrix} A_{11} & A_{12} \\ A_{21} & A_{22} \end{bmatrix}_i \\
\tilde{B}_i &= \begin{bmatrix} B_{w_i} \\ B_c D_{yw_i} \end{bmatrix} = \begin{bmatrix} B_1 \\ B_2 \end{bmatrix}_i \\
\tilde{C}_i &= \begin{bmatrix} C_{z_i} & -D_{zu_i} C_c \end{bmatrix} = \begin{bmatrix} C_1 & C_2 \end{bmatrix}_i .
\end{aligned}$$

Note that the submatrices of the augmented system matrices are a function of the compensator's matrices as follows:

$$\begin{aligned} A_{12} &= f(C_c) \\ A_{21} &= f(B_c) \\ A_{22} &= f(A_c, B_c, C_c) \\ B_2 &= f(B_c) \\ C_2 &= f(C_c) \end{aligned}$$

For the sake of convenience, $\tilde{Q}_i$ and $\tilde{P}_i$ are divided into four $n_x \times n_x$ submatrices,

$$\begin{aligned} \tilde{Q}_i &= \begin{bmatrix} Q_{11} & Q_{12} \\ Q_{21} & Q_{22} \end{bmatrix}_i \\ \tilde{P}_i &= \begin{bmatrix} P_{11} & P_{12} \\ P_{21} & P_{22} \end{bmatrix}_i . \end{aligned}$$

The following basic derivatives of a trace function of matrices with respect to a matrix are used in the derivations [40].

$$\begin{aligned} \frac{\partial}{\partial X} trace\{YX\} &= Y^T \\ \frac{\partial}{\partial X} trace\{YX^T\} &= Y \\ \frac{\partial}{\partial X} trace\{YXZ\} &= Y^T Z^T \\ \frac{\partial}{\partial X} trace\{YX^T Z\} &= ZY, \end{aligned}$$

where X, Y, and Z are square matrices.

The derivatives of the weighted sum of the LQG costs with respect of $\tilde{Q}_i$, A_c, B_c, and C_c are derived as follows:

$$\begin{aligned}
\frac{\partial J_a}{\partial \tilde{Q}_i} &= \sum_{i=1}^{n_{DP}} \beta_i \frac{\partial}{\partial \tilde{Q}_i}[trace\{\tilde{C}_i\tilde{Q}_i\tilde{C}_i^T + \tilde{P}_i\left(\tilde{A}_i\tilde{Q}_i + \tilde{Q}_i\tilde{A}_i^T + \tilde{B}_i\tilde{B}_i^T\right)\}] \\
&= \beta_i[\tilde{C}_i^T\tilde{C}_i + \tilde{P}_i\tilde{A}_i + \tilde{A}_i^T\tilde{P}_i], \qquad (A.2)
\end{aligned}$$

and

$$\begin{aligned}
\frac{\partial J_a}{\partial A_c} &= \sum_{i=1}^{n_{DP}} \beta_i \frac{\partial}{\partial A_c}[trace\{\tilde{P}_i(\tilde{A}_i\tilde{Q}_i + \tilde{Q}_i\tilde{A}_i^T)\}] \\
&= \sum_{i=1}^{n_{DP}} \beta_i \frac{\partial}{\partial A_c}[trace\{(P_{11}A_{11} + P_{12}A_{21})Q_{11} + (P_{11}A_{12} + P_{12}A_{22})Q_{21}\} \\
&\qquad + trace\{(P_{21}A_{11} + P_{22}A_{21})Q_{12} + (P_{21}A_{12} + P_{22}A_{22})Q_{22}\} \\
&\qquad + trace\{(P_{11}Q_{11} + P_{12}Q_{21})A_{11}^T + (P_{11}Q_{12} + P_{12}Q_{22})A_{12}^T\} \\
&\qquad + trace\{(P_{21}Q_{11} + P_{22}Q_{21})A_{21}^T + (P_{21}Q_{12} + P_{22}Q_{22})A_{22}^T\}]_i \\
&= \sum_{i=1}^{n_{DP}} \beta_i \frac{\partial}{\partial A_c}[trace\{P_{12}A_{22}Q_{21}\} \\
&\qquad + trace\{P_{22}A_{22}Q_{22}\} \\
&\qquad + trace\{(P_{21}Q_{12} + P_{22}Q_{22})A_{22}^T\}]_i \\
&= \sum_{i=1}^{n_{DP}} \beta_i \frac{\partial}{\partial A_c}[trace\{P_{12}(A_c - B_cD_{yu}C_c)Q_{21}\} \\
&\qquad + trace\{P_{22}(A_c - B_cD_{yu}C_c)Q_{22}\} \\
&\qquad + trace\{(P_{21}Q_{12} + P_{22}Q_{22})(A_c - B_cD_{yu}C_c)^T\}]_i \\
&= \sum_{i=1}^{n_{DP}} \beta_i[P_{12}^TQ_{21}^T + P_{22}^TQ_{22}^T + P_{21}Q_{12} + P_{22}Q_{22}]_i \\
&= \sum_{i=1}^{n_{DP}} \beta_i[(QP)_{22}^T + (PQ)_{22}]_i, \qquad (A.3)
\end{aligned}$$

$$
\begin{aligned}
\frac{\partial J_a}{\partial B_c} &= \sum_{i=1}^{n_{DP}} \beta_i \frac{\partial}{\partial B_c}[trace\{\tilde{P}_i(\tilde{A}_i\tilde{Q}_i + \tilde{Q}_i\tilde{A}_i^T + \tilde{B}_i\tilde{B}_i^T)\}] \\
&= \sum_{i=1}^{n_{DP}} \beta_i \frac{\partial}{\partial B_c}[trace\{(P_{11}A_{11} + P_{12}A_{21})Q_{11} + (P_{11}A_{12} + P_{12}A_{22})Q_{21}\} \\
&\qquad\qquad +trace\{(P_{21}A_{11} + P_{22}A_{21})Q_{12} + (P_{21}A_{12} + P_{22}A_{22})Q_{22}\} \\
&\qquad\qquad +trace\{(P_{11}Q_{11} + P_{12}Q_{21})A_{11}^T + (P_{11}Q_{12} + P_{12}Q_{22})A_{12}^T\} \\
&\qquad\qquad +trace\{(P_{21}Q_{11} + P_{22}Q_{21})A_{21}^T + (P_{21}Q_{12} + P_{22}Q_{22})A_{22}^T\} \\
&\qquad\qquad +trace\{P_{11}B_1B_1^T + P_{12}B_2B_1^T\} + trace\{P_{21}B_1B_2^T + P_{22}B_2B_2^T\}]_i \\
&= \sum_{i=1}^{n_{DP}} \beta_i \frac{\partial}{\partial B_c}[trace\{P_{12}A_{21}Q_{11} + P_{12}A_{22}Q_{21}\} \\
&\qquad\qquad +trace\{P_{22}A_{21}Q_{12} + P_{22}A_{22}Q_{22}\} \\
&\qquad\qquad +trace\{(P_{21}Q_{11} + P_{22}Q_{21})A_{21}^T + (P_{21}Q_{12} + P_{22}Q_{22})A_{22}^T\} \\
&\qquad\qquad +trace\{P_{12}B_2B_1^T\} + trace\{P_{21}B_1B_2^T + P_{22}B_2B_2^T\}]_i \\
&= \sum_{i=1}^{n_{DP}} \beta_i \frac{\partial}{\partial B_c}[trace\{P_{12}B_cC_yQ_{11} + P_{12}(A_c - B_cD_{yu}C_c)Q_{21}\} \\
&\qquad\qquad +trace\{P_{22}B_cC_yQ_{12} + P_{22}(A_c - B_cD_{yu}C_c)Q_{22}\} \\
&\qquad\qquad +trace\{(P_{21}Q_{11} + P_{22}Q_{21})(B_cC_y)^T\} \\
&\qquad\qquad +trace\{(P_{21}Q_{12} + P_{22}Q_{22})(A_c - B_cD_{yu}C_c)^T\} \\
&\qquad\qquad +trace\{P_{12}B_cD_{yw}B_w^T\} \\
&\qquad\qquad +trace\{P_{21}B_w(B_cD_{yw})^T + P_{22}(B_cD_{yw})(B_cD_{yw})^T\}]_i \\
&= \sum_{i=1}^{n_{DP}} \beta_i[P_{12}^TQ_{11}^TC_y^T - P_{12}^TQ_{21}^TC_c^TD_{yu}^T + P_{22}^TQ_{12}^TC_y^T - P_{22}^TQ_{22}^TC_c^TD_{yu}^T \\
&\qquad +(P_{21}Q_{11} + P_{22}Q_{21})C_y^T - (P_{21}Q_{12} + P_{22}Q_{22})C_c^TD_{yu}^T \\
&\qquad +P_{12}^TB_wD_{yw}^T + P_{21}B_wD_{yw}^T + P_{22}^TB_cD_{yw}D_{yw}^T + P_{22}B_cD_{yw}D_{yw}^T]_i \\
&= \sum_{i=1}^{n_{DP}} \beta_i[(P_{12}^TQ_{11}^T + P_{22}^TQ_{12}^T + P_{21}Q_{11} + P_{22}Q_{21})C_y^T \\
&\qquad -(P_{12}^TQ_{21}^T + P_{22}^TQ_{22}^T + P_{21}Q_{12} + P_{22}Q_{22})C_c^TD_{yu}^T \\
&\qquad +(P_{12}^T + P_{21})B_wD_{yw}^T + (P_{22}^T + P_{22})B_cD_{yw}D_{yw}^T]_i \\
&= \sum_{i=1}^{n_{DP}} \beta_i[\{(QP)_{12}^T + (PQ)_{21}\}C_y^T - \{(QP)_{22}^T + (PQ)_{22}\}C_c^TD_{yu}^T \\
&\qquad +(P_{12}^T + P_{21})B_wD_{yw}^T + (P_{22}^T + P_{22})B_cD_{yw}D_{yw}^T]_i,
\end{aligned}
\tag{A.4}
$$

$$
\begin{aligned}
\frac{\partial J_a}{\partial C_c} &= \sum_{i=1}^{n_{DP}} \beta_i \frac{\partial}{\partial C_c}[trace\{\tilde{C}_i\tilde{Q}_i\tilde{C}_i^T + \tilde{P}_i(\tilde{A}_i\tilde{Q}_i + \tilde{Q}_i\tilde{A}_i^T)\}] \\
&= \sum_{i=1}^{n_{DP}} \beta_i \frac{\partial}{\partial C_c}[trace\{C_1Q_{11}C_1^T + C_2Q_{21}C_1^T + C_1Q_{12}C_2^T + C_2Q_{22}C_2^T\} \\
&\qquad +trace\{(P_{11}A_{11} + P_{12}A_{21})Q_{11} + (P_{11}A_{12} + P_{12}A_{22})Q_{21}\} \\
&\qquad +trace\{(P_{21}A_{11} + P_{22}A_{21})Q_{12} + (P_{21}A_{12} + P_{22}A_{22})Q_{22}\} \\
&\qquad +trace\{(P_{11}Q_{11} + P_{12}Q_{21})A_{11}^T + (P_{11}Q_{12} + P_{12}Q_{22})A_{12}^T\} \\
&\qquad +trace\{(P_{21}Q_{11} + P_{22}Q_{21})A_{21}^T + (P_{21}Q_{12} + P_{22}Q_{22})A_{22}^T\}]_i \\
&= \sum_{i=1}^{n_{DP}} \beta_i \frac{\partial}{\partial C_c}[trace\{C_2Q_{21}C_1^T + C_1Q_{12}C_2^T + C_2Q_{22}C_2^T\} \\
&\qquad +trace\{(P_{11}A_{12} + P_{12}A_{22})Q_{21}\} \\
&\qquad +trace\{(P_{21}A_{12} + P_{22}A_{22})Q_{22}\} \\
&\qquad +trace\{(P_{11}Q_{12} + P_{12}Q_{22})A_{12}^T\} \\
&\qquad +trace\{(P_{21}Q_{12} + P_{22}Q_{22})A_{22}^T\}]_i \\
&= \sum_{i=1}^{n_{DP}} \beta_i \frac{\partial}{\partial C_c}[trace\{-D_{zu}C_cQ_{21}C_z^T - C_zQ_{12}(D_{zu}C_c)^T + D_{zu}C_cQ_{22}(D_{zu}C_c)^T\} \\
&\qquad +trace\{-P_{11}B_uC_cQ_{21} + P_{12}(A_c - B_cD_{yu}C_c)Q_{21}\} \\
&\qquad +trace\{-P_{21}B_uC_cQ_{22} + P_{22}(A_c - B_cD_{yu}C_c)Q_{22}\} \\
&\qquad +trace\{-(P_{11}Q_{12} + P_{12}Q_{22})(B_uC_c)^T\} \\
&\qquad +trace\{(P_{21}Q_{12} + P_{22}Q_{22})(A_c - B_cD_{yu}C_c)^T\}]_i \\
&= \sum_{i=1}^{n_{DP}} \beta_i[-D_{zu}^TC_zQ_{21}^T - D_{zu}^TC_zQ_{12} + D_{zu}^TD_{zu}C_cQ_{22}^T + D_{zu}^TD_{zu}C_cQ_{22} \\
&\qquad -B_u^TP_{11}^TQ_{21}^T - D_{yu}^TB_c^TP_{12}^TQ_{21}^T - B_u^TP_{21}^TQ_{22}^T - D_{yu}^TB_c^TP_{22}^TQ_{22}^T \\
&\qquad -B_u^T(P_{11}Q_{12} + P_{12}Q_{22}) - D_{yu}^TB_c^T(P_{21}Q_{12} + P_{22}Q_{22})]_i \\
&= \sum_{i=1}^{n_{DP}} \beta_i[D_{zu}^TD_{zu}C_c(Q_{22}^T + Q_{22}) - D_{zu}^TC_z(Q_{21}^T + Q_{12}) \\
&\qquad -B_u^T(P_{11}^TQ_{21}^T + P_{21}^TQ_{22}^T + P_{11}Q_{12} + P_{12}Q_{22}) \\
&\qquad -D_{yu}^TB_c^T(P_{12}^TQ_{21}^T + P_{22}^TQ_{22}^T + P_{21}Q_{12} + P_{22}Q_{22})]_i \\
&= \sum_{i=1}^{n_{DP}} \beta_i[D_{zu}^TD_{zu}C_c(Q_{22}^T + Q_{22}) - D_{zu}^TC_z(Q_{21}^T + Q_{12}) \\
&\qquad -B_u^T\{(QP)_{21}^T + (PQ)_{12})\} - D_{yu}^TB_c^T\{(QP)_{22}^T + (PQ)_{22}\}]_i.
\end{aligned}
\tag{A.5}
$$

Bibliography

[1] Kalman, R. E. , "Contributions to the Theory of Optimal Control," *BOLETIN DE LA SOCIEDAD MATEMATICA MEXICANA*, Vol. 5, 1960, pp. 102-119.

[2] Safonov, M. G. and M. Athans, "Gain and Phase Margin for Multiloop LQG Regulators," *IEEE trans. on Automatic Control*, Vol. AC-22, 1977, pp. 173-179.

[3] Athans, M., "The Role and Use of the Stochastic Linear-Quadratic-Gaussian Problem in Control System Design," *IEEE trans. on Automatic Control*, Vol. AC-16, 1971, pp. 529-551.

[4] Doyle, J. C., "Guaranteed margins for LQG regulators," *IEEE trans. on Automatic Control*, Vol. AC-23, 1978, pp.756-757.

[5] Doyle, J. C. and G. Stein, "Multivariable System Design: Concepts for a Classical/Modern Synthesis," *IEEE trans. on Automatic Control*, Vol. AC-26, 1981, pp. 4-16.

[6] Stein, G. and M. Athans, "The LQG/LTR Procedure for Multivariable Feedback Control Design," *IEEE trans. on Automatic Control*, Vol. AC-32, 1987, pp. 105-114.

[7] Okada, K. and R. E. Skelton, "Sensitivity Controller for Uncertain Systems," *AIAA Journal of Guidance, Control, and Dynamics*, Vol. 13, No. 2,1990, pp. 321-329.

[8] Sesak, J. R., "Sensitivity Constrained Linear Optimal Control Analysis and Synthesis," Ph.D. thesis, University of Wisconsin, 1974.

[9] Tahk, M. and J. L. Speyer, "Modeling of Parameter Variations and Asymptotic LQG Synthesis," *IEEE trans. on Automatic Control*, Vol. AC-32, 1987, pp. 793-801.

[10] Hyland, D. C., "Maximum Entropy Stochastic Approach to Controller Design for Uncertain Structural Systems," *Proceedings, American Control Conference*, Arlington, VA, June 1982, pp. 680-688.

[11] Ashkenazi, A. and A. E. Bryson Jr., "Control Logic for Parameter Insensitivity and Disturbance Attenuation," *AIAA Journal of Guidance, Control, and Dynamics*, Vol. 5, No. 4, July 1982, pp. 383-388.

[12] Glover, K. and J. C. Doyle, "State-space formulae for all stabilizing controllers that satisfy an H_∞-norm bound and relations to risk sensitivity," *Systems & Control Letters*, Vol. 11, 1988, pp. 167-172.

[13] Doyle, J. C., K. Glover, P. Khargonekar, and B. Francis, "State space solutions to standard H_2 and H_∞ control problems," *IEEE trans. on Automatic Control*, Vol. AC-34, 1989, pp. 832-847.

[14] Young, P. M., M. P. Newlin, and J. C. Doyle, "μ-analysis with real parametric uncertainty," *Proceeding of the 30th IEEE conference on Decision and Control*, 1991, pp. 1251-1256.

[15] How, J. P., *Robust Control Design with Real Parameter Uncertainty using Absolute Stability Theory*, Ph.D. thesis, Massachusetts Institute of Technology, Cambridge, MA, 1993, (M.I.T. SERC report#1-93).

[16] Grocott, S. C. O., *Comparison of Control Techniques for Robust Performance on Uncertain Structural Systems*, Master's thesis, Massachusetts Institute of Technology, Cambridge, MA, 1994, (M.I.T. SERC report#2-94).

[17] Grocott, S., J. How, D. Miller, D. MacMartin, and K. Liu, "Robust Control Design and Implementation on the Middeck Active Control Experiment," *AIAA Journal of Guidance, Control, and Dynamics*, Vol. 17, No. 6, 1994, pp. 1163-1170.

[18] Meirovitch, L., *Element of Vibration Analysis, Second Edition*, McGraw-Hill, Inc., New York, 1986.

[19] Isidori, A, *Nonlinear Control Systems: An Introduction*, Springer-Verlag, New York, 1989.

[20] Slotine, J. -J. E. and W. Li, *Applied Nonlinear Control*, Prentice Hall, New Jersey, 1991.

[21] Misawa, E. A., J. K. Hedrick, "Nonlinear Observers–A State-of-the-Art Survey," *ASME Journal of Dynamic Systems, Measurement, and Control*, Vol.111, 1989, pp.344-352.

[22] Rohrs, C. E., L. S. Valavani, M. Athans, and G. Stein, "Robustness of Continuous-Time Adaptive Control Algorithms in the Presence of Unmod-

eled Dynamics," *IEEE trans. on Automatic Control*, Vol. AC-30, 1985, pp. 881-889.

[23] Athans, M., *Final Report on Nonlinear and Adaptive Control*, MIT OSP No.95178, Massachusetts Institute of Technology, Cambridge, MA, 1989.

[24] Meressi, T. and B. Paden, "Gain Scheduled $\mathcal{H}_\infty$ Controllers for a Two Link Flexible Manipulator," *AIAA Journal of Guidance, Control, and Dynamics*, Vol. 17, No. 3, 1994, pp. 537-543.

[25] Zames, G., "Feedback and Optimal Sensitivity: Model Reference Transformations, Multiplicative Seminorms and Approximate Inverses," *IEEE trans. on Automatic Control*, Vol. AC-26, 1981, pp. 586-601.

[26] Brogan, W. L., *Modern Control Theory, Third Edition*, Prince-Hall, Inc., Englewood Cliffs, New Jersey, 1991.

[27] Stein, G., "Formal Control System Synthesis with H_2 and H_∞ Criteria," *Viewgraphs for Multivariable Control System, II*, Lecture material prepared by M. Athans in the course 6.234J in 1994 Spring term at Massachusetts Institute of Technology, Cambridge, MA, 1994.

[28] Kwakernaak, H. and R. Sivan, *Linear Optimal Control Systems*, Wiley & Sons, Inc., New York, 1972.

[29] Miyazawa, Y., "Robust Flight Control System Design with Multiple Model Approach," *AIAA Journal of Guidance, Control, and Dynamics*, Vol. 15, No. 3, July 1991, pp. 383-388.

[30] Scales, L. E., *Introduction to Non-Linear Optimization*, Springer-Verlag, New York, 1985.

[31] Grace, A., *Optimization TOOLBOX For Use with MATLAB*, The Math Works Inc., Natick, Massachusetts, 1992.

[32] Glaese, R. M., *Development of Zero-Gravity Structural Control Models from Analysis and Ground Experimentation*, Master's thesis, Massachusetts Institute of Technology, Cambridge, MA, 1994, (M.I.T. SERC report#3-94).

[33] Doyle, J. C., "Analysis of feedback systems with structured uncertainties," *IEE Proceedings*, Vol. 129, Part D, No. 6, 1982, pp. 242-250.

[34] Balas, G. J., J. C. Doyle, K. Glover, A. Packard, and R. Smith, *μ-Analysis and Synthesis TOOLBOX For Use with MATLAB*, The Math Works Inc., Natick, Massachusetts, 1994.

[35] Lehtomaki, N., *Practical Robustness Measures in Multivariable Control System Analysis*, Ph.D. thesis, Massachusetts Institute of Technology, Cambridge, MA, 1981.

[36] Lublin, L., *Multivariable Stability Robustness for Control of Flexible Beams and Trusses*, Master's thesis, Massachusetts Institute of Technology, Cambridge, MA, 1992, (M.I.T. SERC report#6-92).

[37] Campbell, M. E., *Neo-Classical control of Structures*, Master's thesis, Massachusetts Institute of Technology, Cambridge, MA, 1993, (M.I.T. SERC report#4-93).

[38] Padilla, C. E., *Middeck Active Control Experiment: Nonlinear Modeling, Simulation, and Preliminary Control of the Baseline Test Article*, Massachusetts Institute of Technology, Cambridge, MA, 1990 (M.I.T. SERC report#6-92).

[39] The Math Works Inc., *MATLAB Reference Guide*, Natick, Massachusetts, Cambridge, MA, 1993.

[40] Graham, A., *Kronecker Products and Matrix Calculus: with Applications*, Ellis Horwood Limited, Chichester, West Sussex, England, 1981.